Atomic processes in resistive switching devices: from fluctuations to reversible atomic rearrangements

Ph.D. Thesis

presented by

Anna Nyáry

Supervisor: Dr. András Halbritter

at the

Department of Physics

Institute of Physics

Budapest University of Technology and Economics

Budapest, 2024

Contents

Chapter 1

Motivation

Throughout history, the idea of artificial intelligence (AI), the mechanization of human thought, has always been intriguing. In the era of the first computers, the creation of thinking machines seemed to be more and more attainable. By the end of the last century, the IBM-built Deep Blue supercomputer defeated the chess world champion. Then, in 2015, AlphaGo defeated the world champion in Go, a game previously considered too challenging for AI to beat [1]. Although such results are promising, a day-to-day application of AI requires the processing of an immense amount of data that limits the computing speed and results in high power consumption. An alternative is to replace the conventional von Neumann architecture with neuromorphic computing, an approach inspired by the working principles of a human brain. This concept of brain-inspired computing, however, requires the development of fundamentally new technologies.

The novel approaches in neuromorphic computing include various resistive memories, such as memristors. Memristors are generally two-terminal resistive switching devices, named as the blend word from memory resistor. The devices can be switched between non-volatile conductance states by applying a voltage signal. Although there have been a few works reporting resistive switching in nanoscale devices earlier, the field of memristors was boosted in 2008 due to the publication of Strukov *et al.* [2] about a proposed physical model linking the reported resistive switching devices to the concept of memristors defined in electrical engineering in 1971 [3]. The physical mechanism behind and the materials involved in resistive switching, groups memristors into many categories. The widespread research on memristors showed that these devices have immense potential and could present a technology beyond conventional CMOS and Moore's law in applications [4]. Their high speed, stability, and excellent storage density suit them for non-volatile data storage. The low power consumption and analog conductance tuning possibility make them a great candidate in neuromorphic computing. Even the 2022 Edition of the International Roadmap for Devices and Systems lists memristors as promising candidates for analog in-memory computing and expects them to be integrated into neuromorphic applications by 2028 [5].

In a significant proportion of memristors, a nanoscale metallic bridge, a.k.a. filament is formed between the two electrodes. By applying a voltage to the device, the filament diameter, hence its conductivity, can be tuned. The diameter of the

narrowest part of the filament can be close to the atomic scale, so atomic processes can play an important role in the operation. The study of such atomic processes is the main motivation of my research, utilizing two approaches.

On the one hand, although, the switching of memristors can be driven by various processes in the active region, e.g., electrochemical metallization, and valence change mechanism, fundamentally different physical processes may also cause atomic rearrangements, such as current- or voltage-induced atomic switching, which is a well-known phenomenon in atomic-sized pure metal wires without the ion-hosting embedding matrix typical of memristors. The first part of my research focused on the comparative study of such switching characteristics in contrast with the typical memristive behavior. I thoroughly studied pure Ag atomic switches, including the detailed statistical analysis of pure atomic switches compared to Ag-based memristive devices. I also participated in the development and performed characterization measurements of nanofabricated Ag break-junction samples. These results make up the first part of my Ph.D. research, summarized in Chapter 3, as well as in Thesis Statements I-II.

On the other hand, fluctuations of single atoms in a memristive filament can cause significant conductance noise. In addition to the steady-state atomic fluctuations, the voltage-induced fluctuations are particularly relevant in the application of memristive devices. These two areas constitute the second part of my research. I conducted the research of the detailed noise characterization of Ta_2O_5-based crosspoint memristors. I performed an extensive steady-state noise characterization, then voltage-dependent noise spectroscopy aimed to investigate switching dynamics, and I designed and conducted sophisticated experiments of subthreshold cycling for noise tuning. The results are concluded in Chapter 4 and Thesis Statement III.

Fig. 1.1 summarizes these main topics covered by my research, all inspired by atomic processes in resistive switching devices.

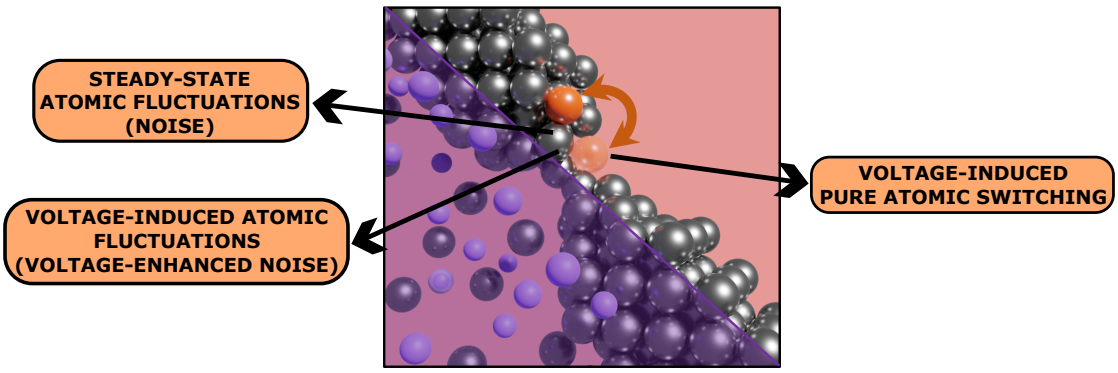

Figure 1.1: *Atomic processes play an important role in atomic scale memristive and metallic filaments, and give rise to different phenomena of interest. My research focuses on voltage-induced pure atomic switching caused by atomic rearrangements in pure metallic nanowires, as well as steady-state and voltage-enhanced noise induced by atomic fluctuations in memristive systems. The illustration is based on key image of Ref. P1.*

Chapter 2

Basic concepts

Resistive switching in this thesis stands for the voltage-induced reversible change of conductance in a two-terminal physical system. If the conductance is retained after removing the electric stimulus, such a device is a non-volatile memory. In this thesis, I will present measurements on different systems, all exhibiting resistive switching controlled by three different switching mechanisms: two types of redox-based resistive switching mechanisms: *electrochemical metallization cell memory (ECM)* and *valence change memory (VCM)*, and *pure atomic switching*. The term *pure atomic switching* will be used exclusively to label resistive switching governed by atomic rearrangements in pure metallic junctions of atomic size, while *memristor* (memory resistor) and *memristive* will be used in a general way to describe the redox-based resistive switching devices and their characteristics. This terminology mostly aligns with the literature, as memristors are usually defined as two-terminal devices with an intermediate insulating switching medium and are often categorized based on the switching materials [6–8]. Meanwhile, the term resistive switching is more general and could also include phase change memories [9], magnetoresistive switching [10], or molecular switching [11], which are not in the scope of this work. However, it is to be noted that there is another trend in the literature that takes the memristor definition even more generally, defining it simply by its current-voltage characteristics ($I(V)$) featuring the pinched-hysteresis loop [3, 12]. Such a broad definition could include pure atomic switching and other resistive switching devices into the category of memristors but is not advantageous for the current purpose of this research that has a special focus on differentiation and comparison.

2.1 Switching characteristics

The characterizing parameters of resistive switching are defined in Fig. 2.1, presenting illustrations of current-voltage characteristics of an example schematic resistive switching. The resistive switching $I(V)$ characteristic is shaped like a bow tie, exhibiting hysteretic behavior. Note that one should distinguish between drive and bias voltage. The former is the applied voltage on the whole circuit including any serial resistors, while the latter is the voltage that is applied on the device. The reproducible switching takes place between the *high-conductance state (HCS)* and the *low-conductance state (LCS)*, which in literature is often also denoted as low

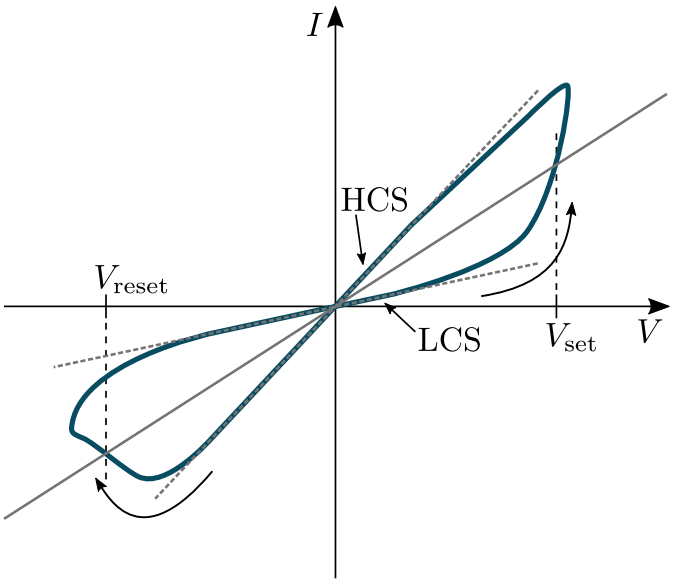

Figure 2.1: *Simplified current-voltage characteristics of an example schematic resistive switching, introducing the characterizing parameters. The switching takes place between the low-conductance state (LCS) and the high-conductance state (HCS). The average conductance is illustrated by the gray line.*

resistance state (LRS) and high resistance state (HRS), or as ON state and OFF state. The arrows indicate the direction of the switching. The transition from LCS to HCS is the *set* transition, while the reversed direction is the *reset* transition. The threshold voltage of the set and reset transition (V_{set}, V_{reset}) can be defined in different ways, for example at the voltage where the conductance starts to change, or where the conductance crosses the average of the HCS and LCS conductances. This latter definition, and the conductance average is illustrated in Fig. 2.1 by the solid gray line.

In an electrochemical metallization cell memory, a metallic filament is formed and dissolved between the contacting electrodes. The devices consist of one active electrode, typically Ag or Cu, and one electrochemically inert electrode, e.g., W, Pt, Ir, Au, as well as an insulating switching medium, traditionally sulfides, iodides, selenides, chalcogenides, or even oxides. Fig. 2.2(a) depicts an ECM device with active Ag and inert Pt electrodes. The set transition occurs with a positive voltage on the active electrode, oxidizing the metal (redox reaction) and releasing Ag^+ cations into the switching medium. The cations migrate to the inert Pt electrode and are electrochemically reduced to Ag atoms on the surface, building up the conducting filament. This process is reversed by the opposite voltage, which anodically dissolves the filament, leading to the reset transition. The filament can build up between the electrodes during the set and might dissolve entirely during the reset transition. The actual filament size, thus the HCS and LCS conductances, are determined by the applied bias voltage [15]. Fig. 2.2(b) presents an ECM-type switching in a device with an AgI insulating layer with both conductance states corresponding to a fully intact filament.

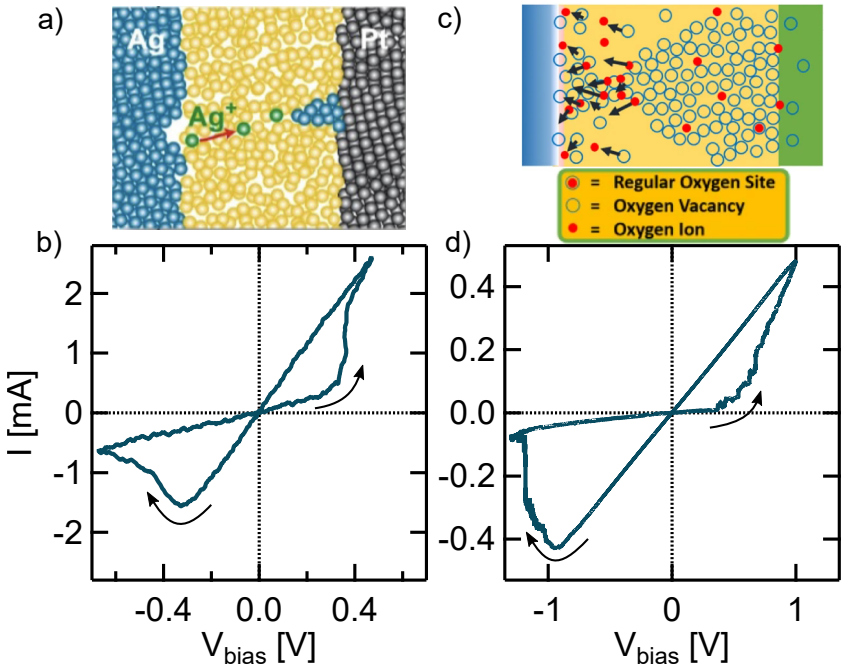

Figure 2.2: *Two different memristive mechanisms and corresponding typical current-voltage characteristics of resistive switching. (a-b) Schematic illustration of set transition in an electrochemical metallization cell (ECM) [13] and Ag/AgI/PtIr memristive switching [P1], (c-d) schematic illustration of set transition in a valence change memory [14] and Ta/Ta_2O_5/Pt memristive switching.*

The switching mechanism in valence change memory devices resembles the ECM-type switching. However, in VCM systems, the active electrode material is either not easily oxidized or the oxidized form is not easily reduced, e.g., Pt, Au or Al, Nb, Ti, Ta. Instead, the active electrode is often a transition metal with high oxygen affinity, and the insulating switching medium is usually a transition metal oxide. During electroforming, the initial, mainly metallic conductance channel is built up by applying a higher voltage than the ensuing switching threshold. This channel is unlike ECM filaments, as it mostly stays intact and does not dissolve at opposite voltage polarity, instead mainly the filament composition changes as described in the following. Fig. 2.2(c) shows the illustration of the set process in a VCM device with the active electrode on the left and the initial electroformed filament. The applied positive voltage on the active electrode creates oxygen anions that can equivalently be described by positively charged oxygen vacancies. The movement of the oxygen vacancies results in the valence changes of the metal oxide material, increasing conductance as an oxygen-depleted transition metal oxide filament is formed. At negative voltage, the filament is saturated with oxygen, decreasing the conductance and leading to the reset transition. To obtain a reversible and stable switching, the set and reset transitions' voltages may not be symmetrical. As I often observed in Ta/Ta_2O_5/Pt memristors, the reset process usually requires higher voltage, like in the example shown in Fig. 2.2(d).

Memristive switching can exhibit gradual transitions between the conductance

states and therefore, serve as an ideal system in the realization of analog multilevel programming. In such a system, the driving voltage analogously tunes the HCS and LCS conductances, as seen in Fig. 2.3(b) where the increasing driving voltage increases the $R_{\mathrm{OFF}}/R_{\mathrm{ON}}$ ratio. The results presented are measured on an Ag/AgI/PtIr ECM device. In memristive systems, the time-dependence of the switching is also a

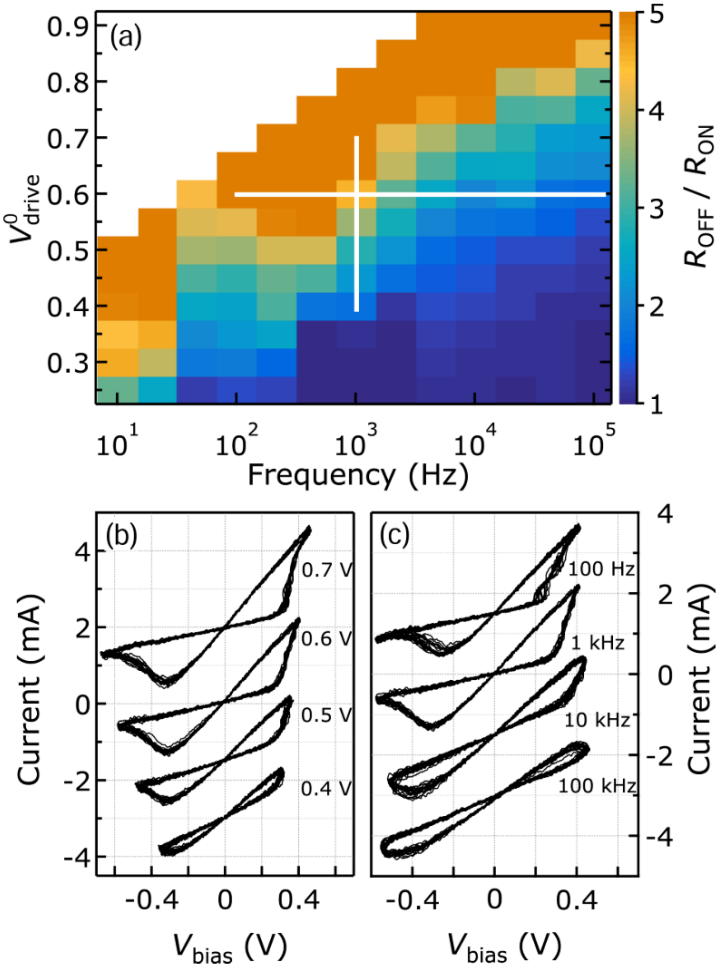

Figure 2.3: *(a) $R_{\mathrm{OFF}}/R_{\mathrm{ON}}$ ratio (indicated by the color scale) tuned linearly by the driving voltage and exponentially by the driving frequency. (b-c) Current-voltage characteristics were obtained with increased driving voltage with fixed 1 kHz driving frequency (b) and increased driving frequency at fixed 0.6 V driving voltage (c). Each consists of 10 consecutive switching cycles, and they are vertically shifted for visibility. Results from Ref. 16.*

well-researched topic, also here Fig. 2.3(c) demontrates such frequency dependence: the increase of the $R_{\mathrm{OFF}}/R_{\mathrm{ON}}$ ratio as the driving frequency is decreased. The meticulous analysis of this ECM-type system's voltage and frequency dependence is concluded in Fig. 2.3(a). The demonstrated voltage-time dilemma shows that a switching with unchanged $R_{\mathrm{OFF}}/R_{\mathrm{ON}}$ ($G_{\mathrm{OFF}}/G_{\mathrm{ON}}$) ratio exhibits the exponential increase of the switching speed with linearly increased driving voltage.

A fundamentally different resistive switching can be observed in pure metallic

nanowires. This so-called pure atomic switching is the sudden geometrical arrangement of individual atoms causing an abrupt jump in the conductance. The illustration of such atomic rearrangement is depicted in Fig. 2.4(a), and a representative $I(V)$ characteristic of a reproducible pure atomic switching is shown in Fig. 2.4(b). In this thesis, only reproducible switchings are investigated, where

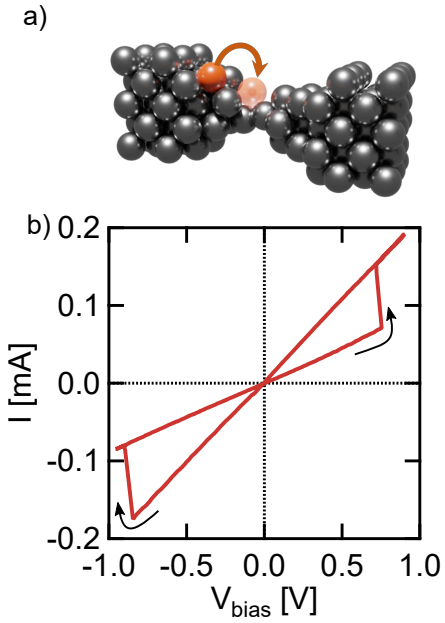

Figure 2.4: *(a) An atomic rearrangement that increases the conductance, (b) pure atomic switching current-voltage characteristics in Ag [P1].*

the initial geometrical arrangement and the corresponding conductance can be attained. Pure atomic switching occurs in the atomic scale and exhibits highly linear conductance states with a jump-like transition. After the transition, the new state is stable even with increasing voltage, and the initial state is attained again at opposite polarity. Therefore, the conductance can only be tuned between discrete conductance states according to discrete geometrical arrangements.

2.2 Applications of memristive switching devices

One of the main motivations behind emerging alternative random access memory (RAM) devices is the challenge posed by scaling down conventional charge storage-based memories to follow Moore's law. The development and fine-tuning of CMOS devices can be sustained for a while but are ultimately bound to reach a physical limit, creating demand for novel memory and computational technologies. Memristors as RAM are referred to as resistive random access memory (RRAM). They are considered a high-potential candidate, as research showed that these devices exhibit fast switching [17–20], high endurance [21], low energy consumption [22] and reasonable fabrication costs. Multiple memristors can be embedded on a chip with high device density while the scalability remains excellent. There are

potential applications in various fields; I will give insights into the application as a multilevel memory and the potential of the memristor-based neuromorphic computing.

The non-volatile memory of a memristor is an excellent base for data storage. In some applications, memristors are considered as a binary memory, as the example switching presented in Fig. 2.1, with an ON state (HCS) and OFF state (LCS). Memristors exhibit high endurance, some of them even exceeding the typical 10^6 cycles of flash memory devices [4], which is complemented by significantly reduced programming and reading energies compared to the flash technology. These properties make memristive technologies promising candidates for future's mass data storage devices.

Additionally, the memory storage density can easily be increased by defining more than one bit and precisely controlling multiple states. To achieve extremely high storage density, the device has to exhibit a wide range of adjustable conductance, and the conductance levels should not exceed the necessary low read noise margin. The method of multilevel programming has been demonstrated many times; one study presented the distinction of 141 states (~ 7 bits) in $Pt/Al_2O_3/Ta/Pt$ memristors [23]. More recently, Rao *et al.* [24] demonstrated 2048 states (11 bits) between ~ 0.65 and $\sim 53.5\ G_0$ in a $Pt/HfO_2/Al_2O_3/Ti/Ta$ device, where $G_0 = 2e^2/h$ denotes the conductance quantum. Fig. 2.5 shows the linear current-voltage curves depicting each of the 2048 conductance states programmed in one memristor device. This high-resolution multilevel programming also demonstrates that the atomic processes are relevant in memristor applications. On the one hand, the conductance is tuned below the conductance quantum, highlighted by the red curve. Later, the description of the Landauer formula (Eq. (3.3)) will explain in more detail, that this conductance range can correspond to atomic-scale conductors, meaning that atomic rearrangements can greatly influence the conductance. On the other hand, the high resolution is achieved by $0.026\ G_0$ distance between neighboring conductance levels and a maximal of $0.013\ G_0$ deviation from the target levels. These small values can only be reached by low-noise memristor states, motivating the study of $1/f$-type noise in memristor devices with a special focus on controlled noise tuning.

The emerging importance of artificial intelligence and machine learning drives another application of memristors which fundamentally relies on their above multilevel programmability. Neuromorphic computing is inspired by the biological functions of the human brain. Software neural networks relying on conventional CMOS-based hardware architectures face problematic scalability limitations due to the growing energy consumption of von Neumann-based computing. A promising alternative to the von Neumann architecture is the memristor-based in-memory computing where the biological neural network is imitated with memristors as artificial synapses. The basic idea of an artificial neural network is presented in Fig. 2.6(a). Let's take the example of the handwritten character recognition process. First, the image has to be divided into pixels, each serving as an input to the network at the input layer. The signal passing through neurons is weighted through synaptic weights connecting the subsequent neuron layers. This means, that the input of a certain neural layer is the product of the output vector of the previous

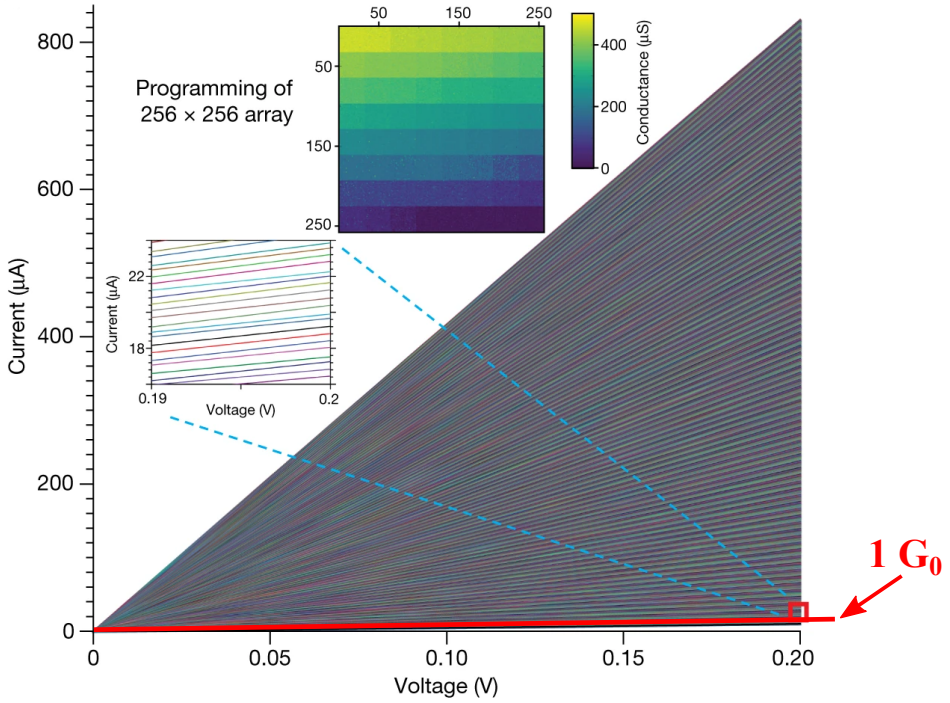

Figure 2.5: *The linear current-voltage characteristics of 2048 conductance states programmed in a $Pt/HfO_2/Al_2O_3/Ti/Ta$ memristor device. The top inset presents 256×256 memristors grouped into 8×8 blocks programmed to 64 distinct conductance levels. The figure from Ref. 24 is modified by highlighting the 1 G_0 curve.*

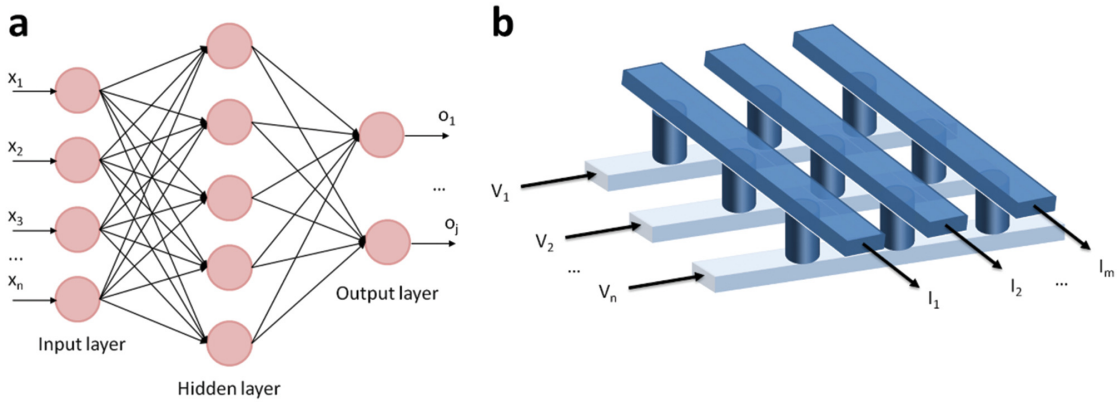

Figure 2.6: *(a) Illustration of an artificial neural network flow chart. (b) Schematic realization of a neural network in a crossbar structure. The applied input voltage and the conductance of the devices are multiplied in a single step to obtain the output current values. From Ref. 25.*

neural layer and the weight matrix represented by the connections between the two layers. The output of a certain neuron is calculated by a proper nonlinear function applied to its input. The output of the final neural layer represents the result of the envisioned computational task, like the recognition of the handwritten digits fed

to the input layer. For a neural network to recognize the digits, first, it is trained with labeled data, and the synaptic weights are adjusted such, that the network provides the best recognition accuracy for the training dataset. After the weights are optimized, they stay fixed, and unlabeled input patterns are recognized by simply passing the input data through this so-called feed-forward neural network according to the above-illustrated rules.

Note, that this network inference has a large computation cost both in power and time consumption, as many vector-matrix multiplications are necessary. The advantage of a memristor-based network lies in its ability to accelerate computation. Fig. 2.6(b) depicts the memristor-based hardware implementation of the data flow between two neural layers with n and m neurons, i.e., a weight matrix with $n \times m$ dimension. In this so-called crossbar setup, the input values are the applied V_i voltages, the G_{ij} memristor conductance determines the weight, and the output results from only a single step of vector-matrix multiplication realized by Ohm's law and Kirchoff's circuit law, leading to the set of I_j current values as follows:

$$I_j = \sum_{i}^{n} G_{ij} \cdot V_i. \tag{2.1}$$

An informative example of written digit recognition was demonstrated in the work of Li *et al.* [26]. Fig. 2.7(a)-(b) illustrate the schematic and implementation of the two-layer neural network. Panel (c) shows the downsampled image of the handwritten digit, fitting the available memristor array dimension. Here, the image resolution is adjusted to 8×8, corresponding to the 64 input pairs of the network. The pixels are described by $\mathbf{v_1}(n)$ voltages which are applied to the inputs. The network utilizes differential memristor pairs, leading to the conductance difference between two memristors acting as a weight. An activation function, here, the softmax function is applied to the $\mathbf{i_1}(n)$ current output of the first layer to obtain the $\mathbf{v_2}(n)$ input voltages for the second layer. The final layer contains 10 neurons, representing the 10 possible outcomes. Based on the current signal on each output (panel (d)), a probability is calculated by applying the activation function. Finally, panel (e) shows that the digit with the highest probability is recognized.

Other similar experiments have already shown a rising number of neural network implementations. Recognition of handwritten character images was achieved with 96% accuracy with a multi-layer neural network containing 2048 memristors [27]. In another experiment, imitation of short and long-term memory was demonstrated by image memorization in 10×10 memristor crossbar arrays [28]. Most such results are still in the experimental phase, and the widespread application demands even more research on memristors to achieve excellent stability, low noise, and high durability.

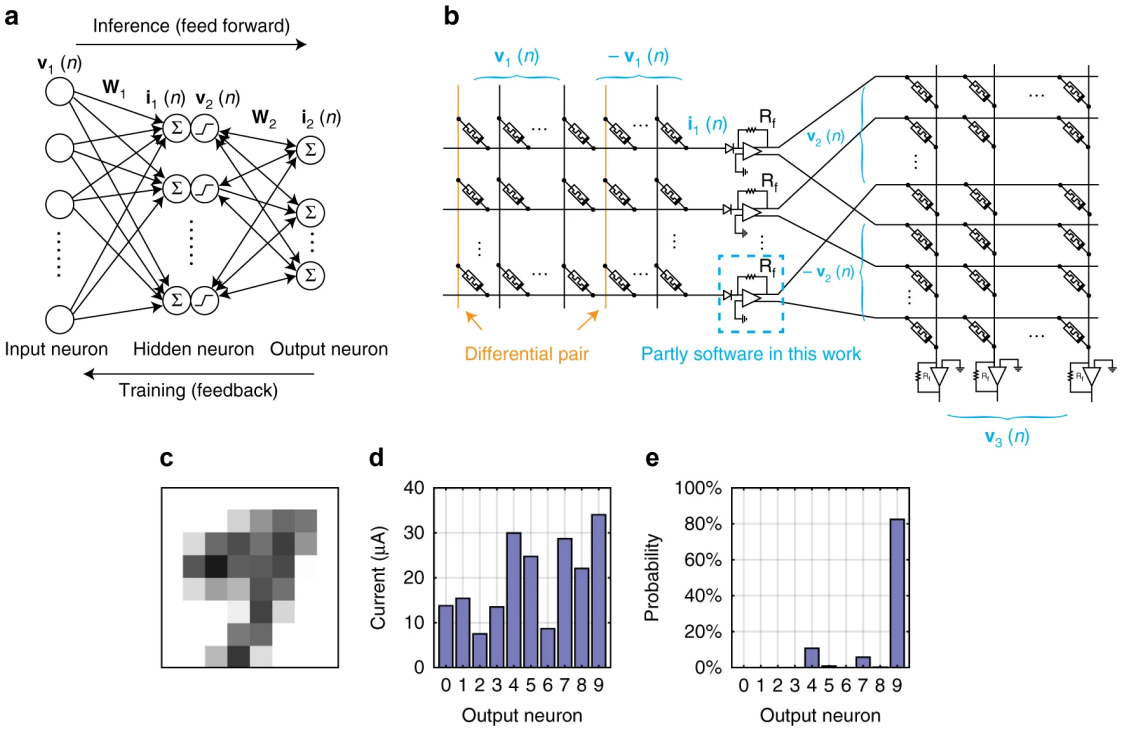

Figure 2.7: *The network inference of handwritten digit recognition. (a-b) The schematic and implementation of the two-layer neural network. (c) The written digit image that is applied to the input of the neural network. (d) The raw output current on the final 10 output neurons. (e) Probability obtained by the activation function applied to the output currents, indicating the highest possibility for the digit 9. Results from Ref. 26.*

Chapter 3

Investigation of pure silver atomic switches

Pure atomic switching is the sudden geometric rearrangement in a pure metallic nanowire that is observed as an abrupt jump in the measured conductance at a specific threshold voltage. In some cases, this jump is reversible, and the original geometry is attainable at reversed voltage. My research on pure atomic switching mainly focuses on reproducible and bistable switchings (see a representative $I(V)$ curve in Fig. 2.4), the necessary experimental techniques for its investigation, and the extensive statistical analysis of the switching characteristics. Pure Ag atomic switches have not been previously investigated, but due to the relevance of Ag-based ECM devices in memristive systems, it is valuable to compare Ag-based memristors with pure Ag atomic switching. These considerations motivated the material choice of Ag in my study of pure atomic switching. I have performed a detailed experimental analysis of pure atomic switching and proposed a vibrational pumping model describing its characteristics. The results are presented in Section 3.3 and outlined in Thesis Statement I. In addition, I also participated in the development of nanofabricated Ag break-junction devices. Conventional nanofabrication techniques are not compatible with oxygen-sensitive metals - such as Ag. Due to this obstacle, Ag break-junctions have not been investigated in a nanofabricated design before. As presented in Section 3.4, a special non-oxidizing process has been used to solve this problem. These results are concluded in Thesis Statement II about the optimalization and characterization of nanofabricated Ag break-junction samples.

Pure atomic switching can be observed in high-stability atomic-sized junctions between stable atomic configurations. A widely used technique for creating high-stability atomic-sized nanowires is the mechanically controllable break-junction (MCBJ) setup, which not only yields high stability but the *in situ* breaking of the nanowire grants a fresh and clean surface ideal for high purity conditions. There are two types of MCBJ samples based on the sample preparation technique, both presented in this work: the more robust notched-wire [29, 30] and the more elaborate nanofabricated [31, 32] MCBJ samples. These techniques rely on a free-standing bridge of high-purity metallic wire or nanofabricated constriction mounted on a

flexible sample substrate, bent mechanically in a three-point bending setup. The stretching of the nanowire, thus the x direction displacement, is controlled by the z direction movement of the pushing rod, as illustrated schematically in Fig. 3.1. The u length of the suspended bridge, the h height of the junction, and the L

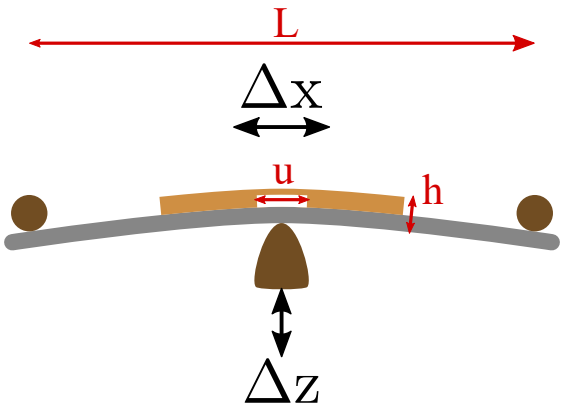

Figure 3.1: *Schematic illustration of the MCBJ sample with labeled dimension: u is the length of the suspended bridge, h is the height of the junction, and L is the distance of the counter-supports. Δz denotes the displacement in the z direction measured from the neutral line in the bending beam, realized by the pushing rod, while Δx is the elongation of the suspended nanowire.*

distance of the counter-supports will specify the actual displacement ratio. For a homogeneous strain, this ratio can be estimated by the following relation [32]

$$r = \frac{\Delta x}{\Delta z} = \frac{6uh}{L^2}. \tag{3.1}$$

As a consequence, the smaller dimensions of the nanofabricated MCBJ free-standing bridge offer a much higher mechanical stability. The typical displacement ratio values are around $10^{-3} - 10^{-2}$ for notched-wire and around $10^{-6} - 10^{-4}$ for nanofabricated samples [33]. However, nanofabricated MCBJ samples are not only more elaborate, but most metals, such as Ag, are not compatible with the traditional nanofabrication procedure. Furthermore, the robustness of notched-wire MCBJ samples has other advantages, such as being more withstanding against electrostatic discharges and having a typically longer lifetime.

The measured conductance of an atomic wire does not follow the rules of macroscopic transport. As the dimensions of the investigated system reach atomic limits, quantum mechanical considerations are necessary for the description of transport. By Ohm's law in a wire, one would expect the conductance to decrease continuously as the cross-section decreases ($G = \sigma A/L$) where σ is the conductivity, A is the cross-section and L is the length of the investigated sample. The conductivity is derived from the Drude model of conduction which takes the scattering of electrons on impurities and defects of the crystal lattice into account. Fig. 3.2(a) illustrates such a system in the diffusive transport regime. The path of an electron is indicated by the line, as it is scattered from one to another scattering center. The l_{m} momentum relaxation length is characteristic of the distance of the scattering events.

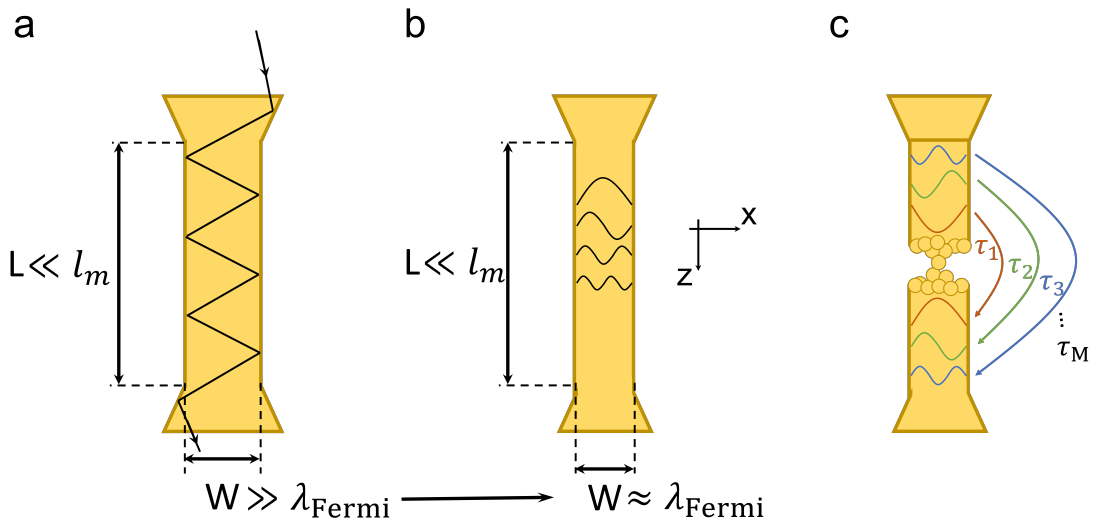

Figure 3.2: *Illustration of a diffusive (a) and ballistic (b) transport regime, and (c) point-contact system with. L denotes the characteristic length, W the width of the conductor, l_m is the momentum relaxation length, and λ_{Fermi} is the Fermi wavelength. The τ_i transmission coefficients denote the probabilities in all open channels for an electron to pass through. Based on Ref. 34.*

At the quantum limit of the length scale, as soon as the W size of the conductor gets commensurate with the λ_{Fermi} Fermi wavelength, the electrical transport is described as ballistic. In a simple picture of considering a quantum wire, just like in Fig. 3.2(b), propagation in the z direction is unbound, and a hardwall potential encloses the x direction. The electron wave function will take the form

$$\psi_{n,k}(x,z) = \mathrm{e}^{ikz} \cdot \sin\left(\frac{n\pi x}{W}\right), \tag{3.2}$$

which describes a longitudinal plane wave propagation and transversal standing wave with n quantum number, see Fig. 3.2(b). The energy eigenstates are given by parabolic dispersion relations, and all modes with available energy states below the Fermi energy are considered open channels. The conductance of such an ideal quantum wire system with M open conduction channels can be described in the form of

$$G = \frac{2e^2}{h} \cdot M, \tag{3.3}$$

where $G_0 = 2e^2/h \approx 1/12.9$ kΩ is the conductance quantum, the conductance of a single-channel ideal quantum wire.
A point-contact system, however, cannot be considered an ideal quantum wire, as there may be a finite probability for an electron to pass through the wire due to scattering at the junction bottleneck, see panel (c) for the illustration of this case. Rolf Landauer [35] showed that the description above can be extended by taking the transmission probabilities for each n open channel into account. Consequently, the conductance of a point-contact system with M open conduction channels with

the set of τ_i transmission coefficients exhibits a conductance summed up from the individual channels:

$$G = \frac{2e^2}{h} \cdot \sum_{n=1}^{M} \tau_n. \tag{3.4}$$

Based on the Landauer expression for point-contacts, the conductance of each atomic configuration depends on the channel transmissions. In experiments, by bending and subsequent return to the non-bent state of the sample, the constriction of the MCBJ sample is stretched and contracted. That way, the atomic wire can be broken and formed repeatedly in a mechanically controlled fashion while the conductance of the wire is monitored. Although the bending of the sample is continuous, the breaking yields step-like changes in the conductance which correspond to abrupt atomic rearrangements between stable junction configurations. By repeated breaking, some steps reproduce more frequently in accordance with the more favorable geometrical configurations [36]. The statistical tool used for the sample characterization is a histogram created from the repeated breaking of the junction, which clearly highlights the most reoccurring conductance step values. The conductance of the single-atom junction for some monovalent metals is around 1 G_0 due to a single nearly perfectly transmitting channel in this configuration, the most popular example is Au single-atom contact [37, 38]. Similar behavior is observed in the material of interest in my research, in Ag. Fig. 3.3 presents the conductance histogram of an Ag atomic wire, presented by Rodrigues *et al.* [39]. Two typical breaking traces are shown in the inset, clearly demonstrating conductance plateaus. The 1 G_0 sharp peak and 2.4 G_0 broadened peak in the

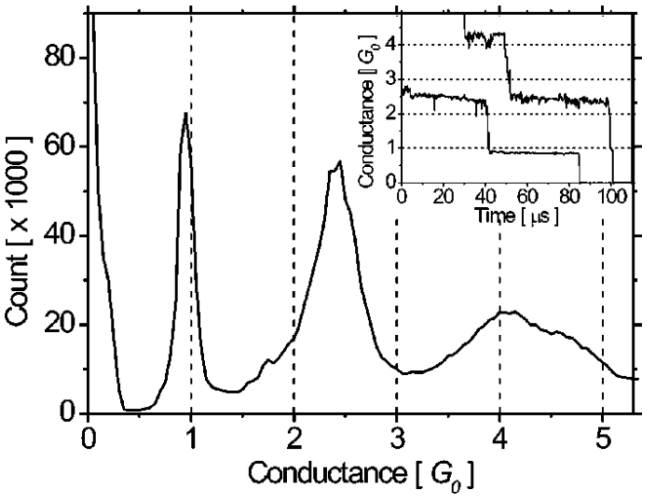

Figure 3.3: *Conductance histogram of repeated breaking of an Ag atomic junction showing two clear peaks at favorable geometrical configurations, presumably a one-atom and two-atom junction. The inset shows typical breaking traces with conductance plateaus around the observed histogram peaks. Results from Ref. 39.*

histogram indicate frequently occurring geometrical configurations, presumably a one-atom and two-atom junction. Although the single-atom conductance is usually in the order of magnitude of G_0, most metals have multiple partially transmitting

channels in this configuration accounting e.g., a conductance of 0.8 G_0 in Al [40, 41], or 2.6 G_0 in Nb [42, 43].

It is a reasonable assumption that in atomic-sized filaments, pure atomic rearrangements can play a crucial role in ECM-based filamentary switches. There are indeed studies in the ultimate atomic limit [24, 44, 45], and also results highlighting atomic behavior in memristors. An evident example is given by Wagenaar *et al.* [46] who reported about measurements on Ag_2S-based memristors, presenting both step-like and continuous breaking traces in the atomic-scale, depicted in Fig 3.4, attributing these to abrupt rearrangements in pure metallic filaments and to gradual decay of locally modified structure of Ag_2S filaments, respectively. Although results

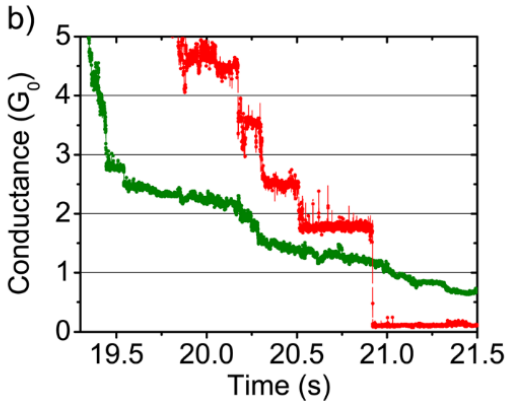

Figure 3.4: *Both, step-like (red) and continuous (green) breaking traces in the atomic-scale of Ag_2S-based ECM-type memristor. Results from Ref. 46.*

nicely demonstrate atomic behavior expected in pure metallic systems, but also do not exclude any influencing effect of the embedding Ag_2S matrix. In the next section, I will review atomic-scale rearrangements and even switching in pure metallic systems. Then in Section 3.3, I will give two other examples of atomic phenomena observed in memristive systems.

3.1 Literature overview of pure metallic atomic rearrangements and switching

3.1.1 Experimental realization of pure atomic switching

Several studies reported about voltage-driven bistable atomic switches observed in pure metal atomic junction, exhibiting either switching between the broken junction and contact regime [47, 48] or switching between various contact conductances [49–53]. These experiments were carried out on a wide variety of materials, including Au, Cu, Al, and Pb. The work of Schirm *et al.* [50] presented the significant result that the switching is attributed to the geometrical rearrangement of the atomic wire. The research group investigated the pure atomic switching measured in a low-temperature Al nanofabricated MCBJ setup. The switching was driven by

ramping the drive current until an abrupt change of conductance was detected, then reversing the ramp for the transition back to the initial state at the reversed polarity. The group investigated bistable switchings and used the so-called superconducting subharmonic gap structure in the current-voltage characteristics to resolve the transmission channels. An example switching is presented in Fig. 3.5(a), revealing the set of τ_i transmission coefficients (red and blue circles) in the two $G = G_0 \cdot \sum_i \tau_i$ conductance states (red and blue triangles for the HCS and LCS, respectively), as described by the Landauer formula from Eq. 3.3. Panel (b) depicts the corresponding superconducting current-voltage characteristics of the two states with consistent coloring. The basic idea behind this technique is that multiple Andreev reflections

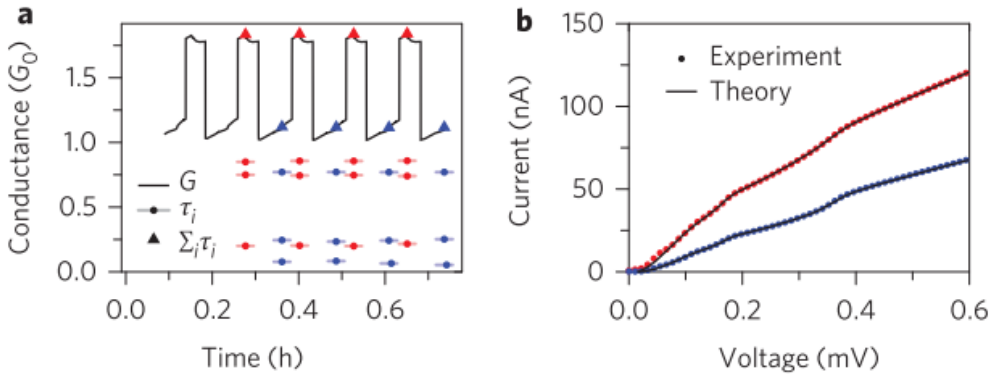

Figure 3.5: *(a) Conductance and the corresponding transmission coefficients for a bistable pure atomic switching in low-temperature Al junction. (b) Superconducting subharmonic gap structure in the current-voltage characteristics of the two conductance states. Results from Ref. 50.*

between superconducting leads cause nonlinearities in the $I(V)$ characteristics [41, 54]. This phenomenon is sensitive to the ensemble of transmission coefficients, therefore, fitting the obtained superconducting $I(V)$ characteristics reveals the individual coefficients of the atomic contact. By analyzing the states of stable pure atomic switching presented here, the subharmonic gap structure revealed the 3-3 conducting channels with unchanged transmission coefficients during the subsequent switching, proving the true reversibility of the switching, indicating well-defined atomic arrangements in both states. The analysis was supported by molecular dynamics simulation that showed a corresponding atomic configuration for a chosen switching, depicted in Fig. 3.6(b)-(c). The simulation consisted of multiple stretching events while monitoring the evolution of transmission coefficients. Panel (a) presents such an event, the evolution of the overall conductance and the individual coefficients with increasing displacement. The number of channels with nonzero transmission is plotted on the right axis (blue circles). The single-atom switching configurations of panels (b) and (c) are extracted at the displacement values indicated by vertical dashed lines. The simulated conductance corresponds to the measured set of transmission coefficients extracted in Fig. 3.5(a), demonstrating the quite probable configuration for the exemplified switching.

Another research group, Yoshida *et al.* [48], published results about pure atomic

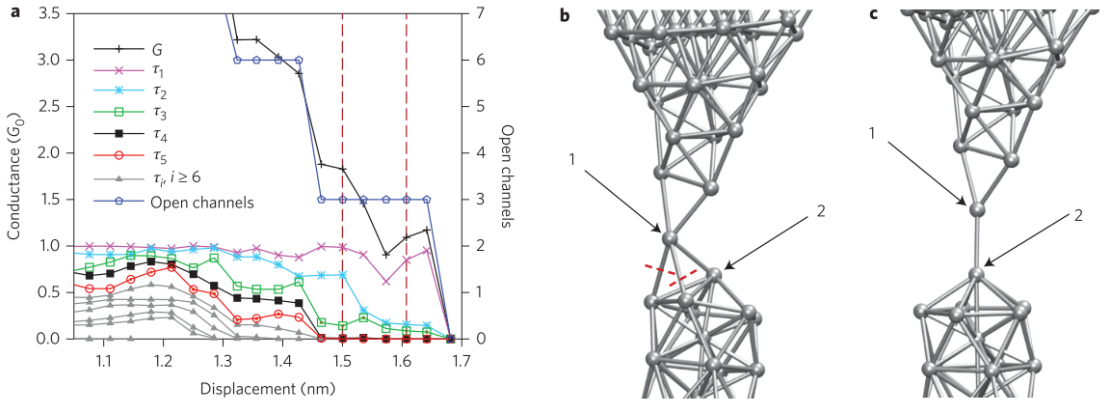

Figure 3.6: *(a) Molecular dynamics simulation of transmission coefficients during a stretching event. The evolution of the overall conductance, the individual coefficients and the number of open channels with the displacement. (b-c) The single-atom switching configurations extracted at displacement values 1.5 and 1.6 nm. Results from Ref. 50.*

switching on gold atomic contacts, switching between tunneling and contact regime. A triangle signal is applied to the sample, resulting in the current-voltage characteristics presented in Fig. 3.7(a). The characteristics exhibit a linear trend for both

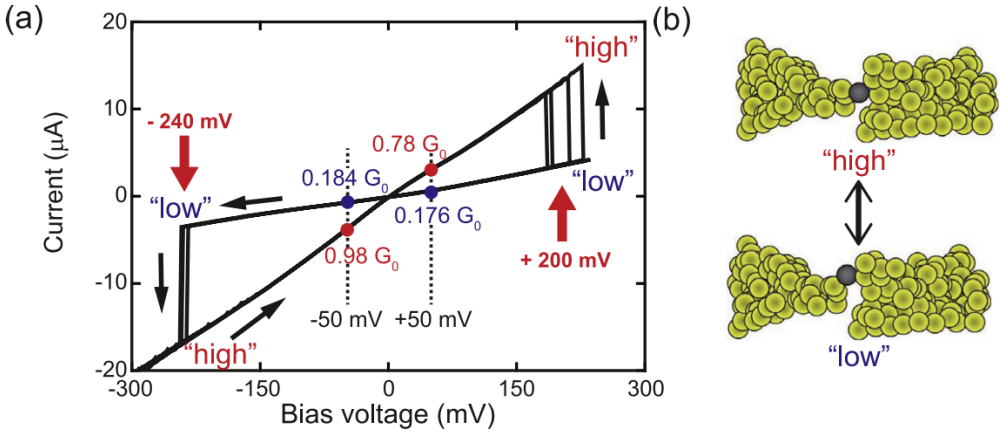

Figure 3.7: *Pure atomic switching between tunneling and contact regime. (a) Cycle-to-cycle variation of current-voltage characteristics. (b) Supposed geometric rearrangement corresponds to the switching. Results from Ref. 48.*

states and the typical abrupt jump in conductance, which are distinctive features for pure atomic switches. The supposed geometric rearrangement corresponding to the conductance states both below 1 G_0 are depicted in panel (b). The measurements are obtained at low temperatures on a nanofabricated planar break-junction. In such a sample, the atomic point-contacts are fabricated by narrowing the constriction of the sample by an electromigration routine that controls the applied voltage based on the evolution of the conductance. The authors did not conduct a statistical analysis on pure atomic switching, they instead investigated the so-called

stochastic resonance. This phenomenon is realized by adding noise of an appropriate amplitude to a subthreshold voltage which enables the switching.

The only room-temperature pure atomic switching published in the literature is the work of Wang *et al.* [51] on Au. The results are obtained on a nanofabricated mechanically controllable break-junction sample. The sample design exhibits extraordinary stability, crucial for observing the rearrangements in the atomic-scale nanowire at room temperature. The measurement scheme used a feedback-controlled voltage signal, i.e., the applied voltage ramp was reversed as soon as an abrupt jump was detected in the conductance. Fig. 3.8(a) and (c) present the time-dependent conductance and the resulting current-voltage characteristics, respectively, of a reversible pure atomic switching. The applied voltage signal is depicted in panel (b). The group then demonstrated the utilization of atomic manipulation by repeated

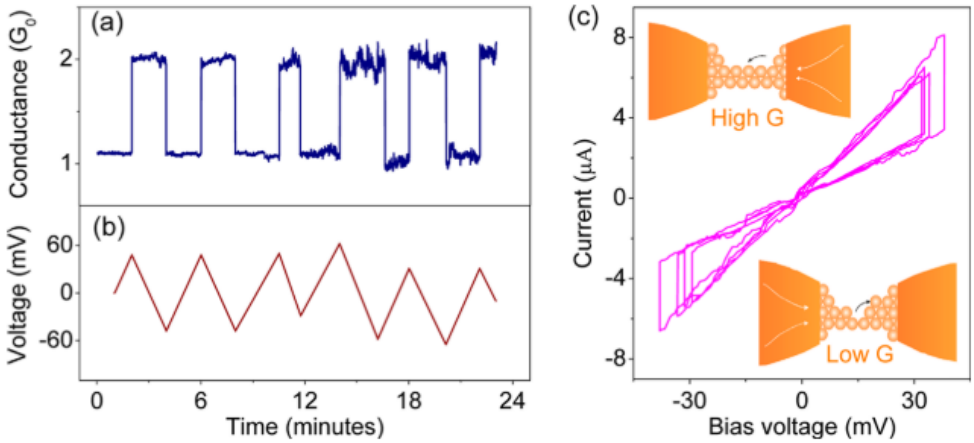

Figure 3.8: *Room-temperature pure atomic switching observed in Au junctions. The measured conductance of a bistable switch (a) and the corresponding feedback-controlled voltage (b). (c) Current-voltage characteristics of pure atomic switching. Insets show assumed atomic arrangements attributed to the conductance states. Results from Ref. 51.*

voltage-driven breaking of the atomic wire. The conductance evolution suggests that the breaking can be controlled in a highly precise way, with atoms removed even one by one. This protocol of accurately controlled breaking is proposed to serve as a useful technique for the fabrication of extremely small gaps, ideal for single-molecule measurements.

3.1.2 Theoretical description of pure atomic switching

There are a few different approaches to describe pure atomic switches theoretically. First, current-induced forces were used to describe atomic rearrangement. The basis for that was given by the theoretical and experimental study on the failure of single-atom junctions. Brandbyge *et al.* [55] presented first-principles calculations revealing that an applied bias from 100 mV to 2 V induces forces in the range of $0.05 - 1$ nN in Au atomic wires. Experimental results on the rupture force of a

single-atom Au contact were found to be around 1.5 nN [56, 57], reinforcing the role of current-induced forces in the breaking of the wire. The rupture forces are in a similar range of magnitude for Ag atomic wires at $1-2$ nN [58, 59].
Based on these results, the paper of Schirm *et al.* [50] considered the atomic rearrangements as an atomic-scale electromigration phenomenon, and presented simulations of the stretching process of nanowires. The authors calculated the evolution of the total energy and force in Al nanowires by molecular dynamics simulations with a tight-binding description of the electronic structure. A stretching event between 2.5 to 1.5 G_0, is plotted in Fig. 3.9. The jumps in the energy and

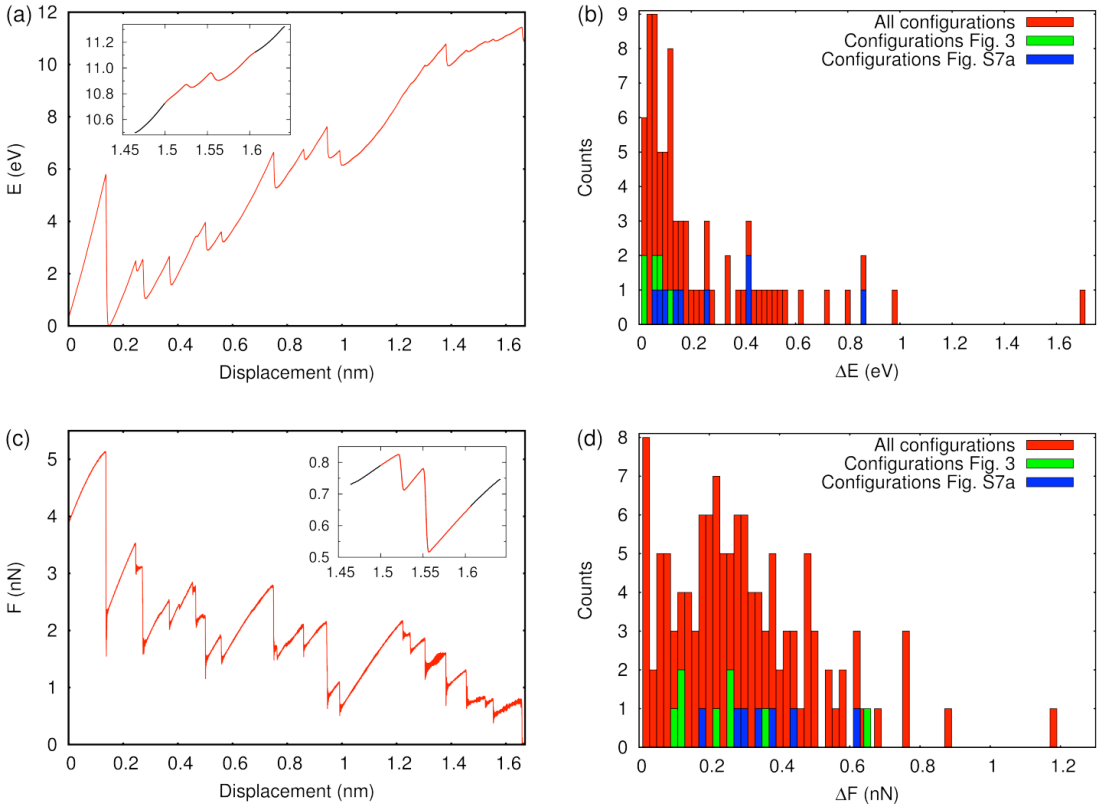

Figure 3.9: *Results of molecular dynamics simulation on the total energy and force in Al nanowires during stretching events. (a-b) Evolution of the total energy during stretching, and corresponding histogram of the energy jump height (energy barrier) in 100 stretching events. (c-d) The same evaluation as (a-b) for the force and force jump heights. The insets of panels (a) and (c) present smoothed curves used in the evaluation. The green and blue colors in the histogram consider results for selected configurations not shown here. Results from Ref. 50.*

force curve of one stretching event in panels (a) and (c) correspond to dislocation of single atoms, and these jump heights are analyzed further in the histograms of panels (b) and (d) which includes the ΔE and ΔF jump heights obtained from 100 stretching events. The analysis shows typical energy barriers of $50-300$ meV and force barriers of $0.05-0.5$ nN. Although this simulation does not describe the electromigration process itself but the mechanical stretching, the obtained values

are in good correspondence with the experimental findings. They conclude that the forces caused by electromigration suffice to cause atomic rearrangements similar to mechanical deformations.

The same research group continued the investigation of atomic rearrangements with the focus on the material- and conductance-dependent threshold voltages. In the publication of Ring *et al.* [60], they presented the analysis of many atomic rearrangements in four materials: Pb, Au, Al, and Cu. In the measurements, they ramp the applied current while monitoring the junction conductance. As soon as an abrupt jump is detected, the ramp direction is inversed. In this paper, the goal was to obtain independent atomic rearrangement for a large statistical analysis, therefore, they only investigated independent rearrangements instead of reproducible switching. The distribution of switching current and the mean value grouped by conductance is depicted in Fig. 3.10, showing large variation and apparent material differences but a consistent increase in the threshold current for increasing conductance. However, these results somewhat deviate from classical

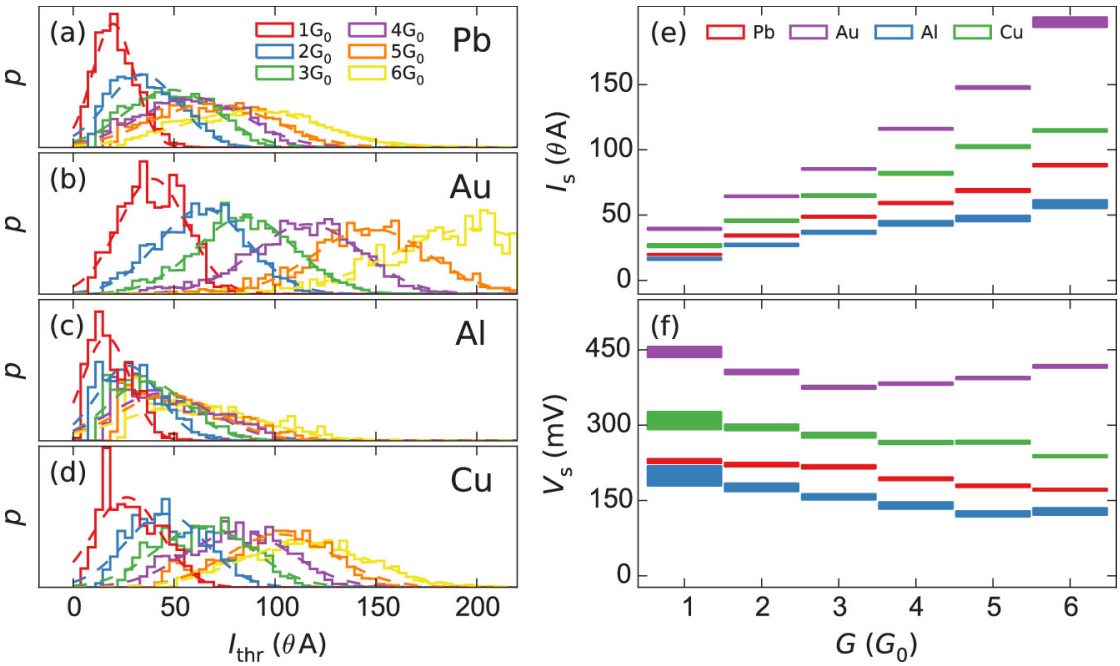

Figure 3.10: *Material dependence of the threshold voltages. (a-d) Distribution of switching currents grouped by initial conductance. (e) The mean value of switching currents grouped by initial conductance consistently increases for all materials. (f) The mean value of switching voltages grouped by the initial conductance is rather weakly depending on the initial conductance. Results from Ref. 60.*

theory of current-induced electromigration. In macroscopic wires, the current density drives the electromigration ($j = I/A$), which entails the linear dependence between the threshold current and the A cross-section. The presented threshold current shows a weaker dependence on the conductance. This is in line with the fact that atomic-size conductance and the number of atoms in the junction does not scale linearly with the cross-section [38]. The authors used a theoretical

description of voltage-induced pumping of particular phonon modes, so-called runaway modes. As soon as the runaway voltage is reached, the phonon mode is much more effectively pumped which leads to the destabilization of the atomic arrangement. The experimental threshold voltages are identified as these runaway voltages, where vibration modes become unstable and launch the switching event. The simulated runaway voltages and variance are compared to the experimental

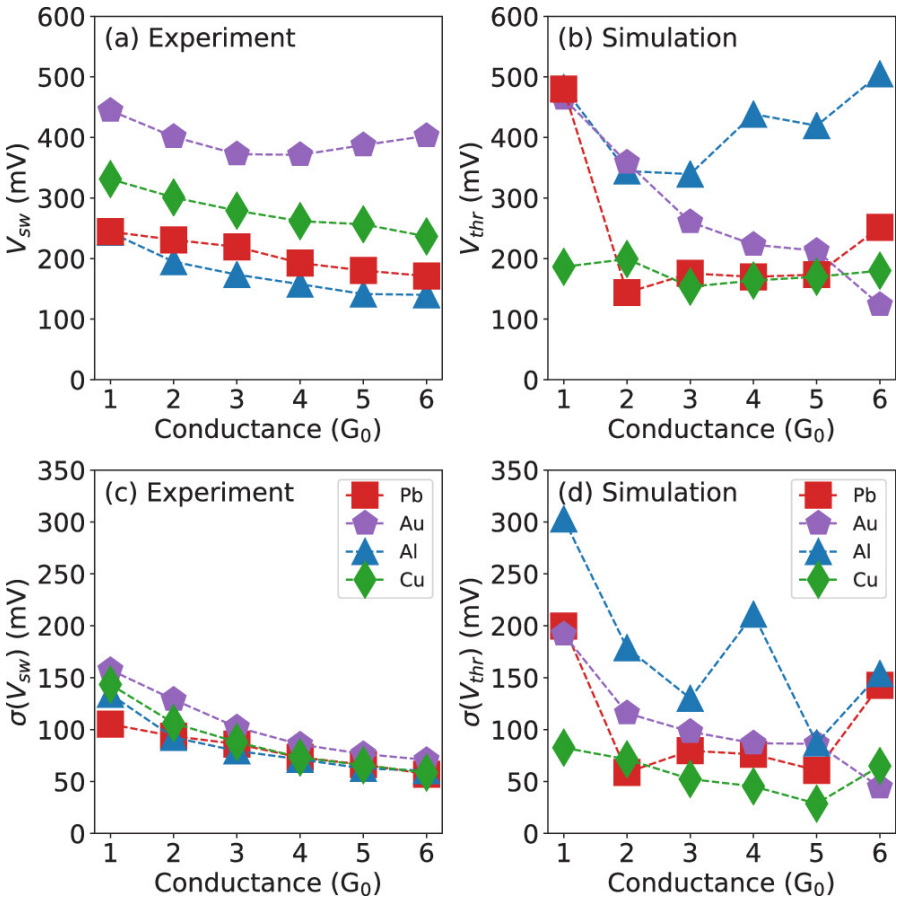

Figure 3.11: *Mean values and standard deviations of switching voltages, experimental results (a,c) compared with simulation results (b,d). The investigated materials are indicated by different colors corresponding to the legend. Results from Ref. 60.*

data in Fig. 3.11. The authors conclude that the results are in the same order of magnitude as the experimentally obtained threshold voltages and variances and are mostly in qualitative agreement.

Papior *et al.* [61] proposed a different approach to describe the material dependence of the critical voltage of breaking a 1D metal chain. The authors presented first-principles calculations of the current-induced ultimate tensile strength, i.e., the force at which the chain becomes unstable. They proposed a simple comparison to the threshold voltages observed by Ring *et al.* [60] (see Fig. 3.11(a)) by defining a critical voltage based on the tensile strength, taking its strain and voltage dependence into account. The comparison is plotted in Fig. 3.12 with values normalized to the critical voltage of Au. The experimental

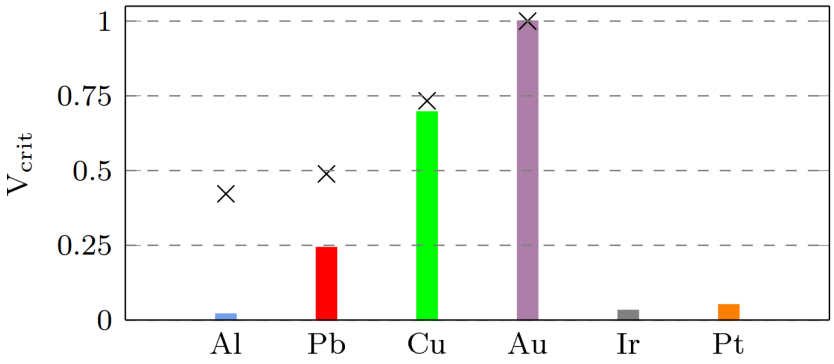

Figure 3.12: *Simple comparison of material-dependent critical voltages obtained based on calculations of the current-induced ultimate tensile strength in 1D metal chains (colored bars) to experimental threshold voltages (black crosses) from Ref. [60] (see Fig. 3.11(a)). Experimental values are chosen at the conductance corresponding to infinite chains at zero voltage:* 1 G_0 *in Au and Cu,* 3 G_0 *in Pb, and* 2 G_0 *in Al. Voltages are normed to the critical (threshold) voltage in Au. Results from Ref. 61.*

values are at the conductances corresponding to infinite chains at zero voltage and are indicated by the black crosses. The analysis shows that the critical voltage reproduced the sequence of the measured threshold voltages. The authors noted that multiple effects, such as electron-phonon coupling, phonon heat conduction, non-conservative forces, etc., may play an additional role in the atomic rearrangement process, influencing the junction's stability.

3.2 Experimental techniques

3.2.1 The principle of the experimental setup

Resistive switching is observed in conductance measurements; the simplified and general schematic diagram of the required electrical system is outlined in Fig. 3.13. The circuit consists of the data acquisition card, the investigated sample, the serial

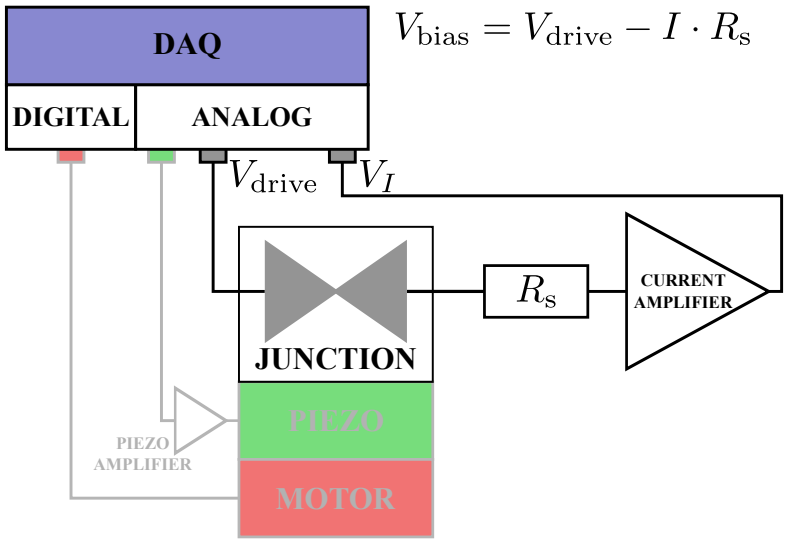

Figure 3.13: *General schematic diagram of the conductance measurements used for observing resistive switching. The data acquisition (DAQ) card is the central piece of the setup, outputting voltage, measuring current, and controlling the piezo and motor positioner. Depending on the sample design, the piezo and motor positioner, colored in green and red, are omitted from the setup.*

resistance, and the current amplifier. In all measurements presented in this chapter, the data acquisition card is a National Instruments USB-6363, which is outputting the drive voltage V_{drive} and measuring the voltage $V_I = R_{\text{gain}} \cdot I$ translated from the current I flowing in the circuit and R_{gain} transimpedance (gain) of the current amplifier Femto DLPCA-200. Finally, the actual V_{bias} bias voltage on the sample is calculated based on the known value of the R_{s} serial resistance:

$$V_{\text{bias}} = V_{\text{drive}} - I \cdot R_{\text{s}}. \tag{3.5}$$

The tuning of the conductance of the junction is different for the different sample fabrication techniques and will be discussed in detail in Sections 3.2.2, 3.2.3 and 3.2.4. In some cases, the tuning may involve the control of the stepper motor and piezo positioner for coarse-tuning and fine-tuning, respectively, see red and green boxes in Fig. 3.13.

In this chapter, I will present altogether four different sample fabrication techniques relevant to my research. Section 3.2.2 presents the Ag notched-wire mechanically controllable break-junction technique I used to observe pure atomic switching in pure nanowires. Section 3.2.3 gives an overview of the AgI-based

scanning tunneling microscopy break-junction technique measurements realized by Botond Sánta and Dániel Molnár [16, 62]. I used the results of these ECM-type resistive switching experiments as a comparative reference to the pure atomic switchings. Section 3.2.4 summarizes the preparation of the ECM-type Ag_2S-based nanofabricated planar sample created and measured by László Pósa [63, 64] that exhibited both atomic-scale and ECM-type switching. Finally, at the end of the chapter, in Section 3.4, I will separately introduce the newly developed fabrication steps and measurements of nanofabricated mechanically controllable break-junction samples for oxygen-sensitive metals in detail.

3.2.2 Pure Ag notched-wire mechanically controllable break-junction (MCBJ)

The pure atomic switching measurements presented in detail in Section 3.3.1 were conducted in the notched-wire MCBJ setup. The sample fabrication requires some practical experience but is easy to learn, and samples can be prepared within a day. Two typical samples are shown in Fig. 3.14 together with a close-up photo of the freestanding junction. The first step of the sample preparation is cutting the flexible

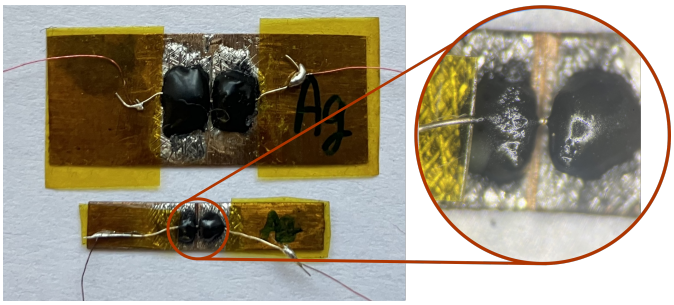

Figure 3.14: *Photo of two typical notched-wire MCBJ samples with close-up to the junction area. The two sizes are in accordance with the two different sample holders.*

phosphor bronze substrate to the dimensions fitting the sample holder. Next, after the surface is cleaned, some soldering tin is applied and corrugated to provide a rough surface for the epoxy glue to adhere to. Two drops of LOCTITE® STYCAST glue are placed on the substrate as near to each other as possible, and while still wet, the Ag wire of 125 µm in diameter is pushed into them. After the glue solidifies, the wire has to be notched by hand with a sharp razor blade, leaving only a small part (typically 20-40% of the original diameter) of the wire still connected that designates the point of breaking. To eliminate the risk of shortcuts between the Ag wire and the substrate, an insulating Kapton® tape is applied. Finally, the junction is connected by carefully soldering thin copper wire to the Ag wire.

The completed sample is mounted in one of two custom-built low-temperature MCBJ sample holders pictured in Fig. 3.15. The difference between these setups is the mechanical technique to bend the sample; however, whether this is executed by a differential or by a cone-shaped screw, both are equivalently suitable for investigating atomic switches. The head of the sample holder can be sealed and serves as a

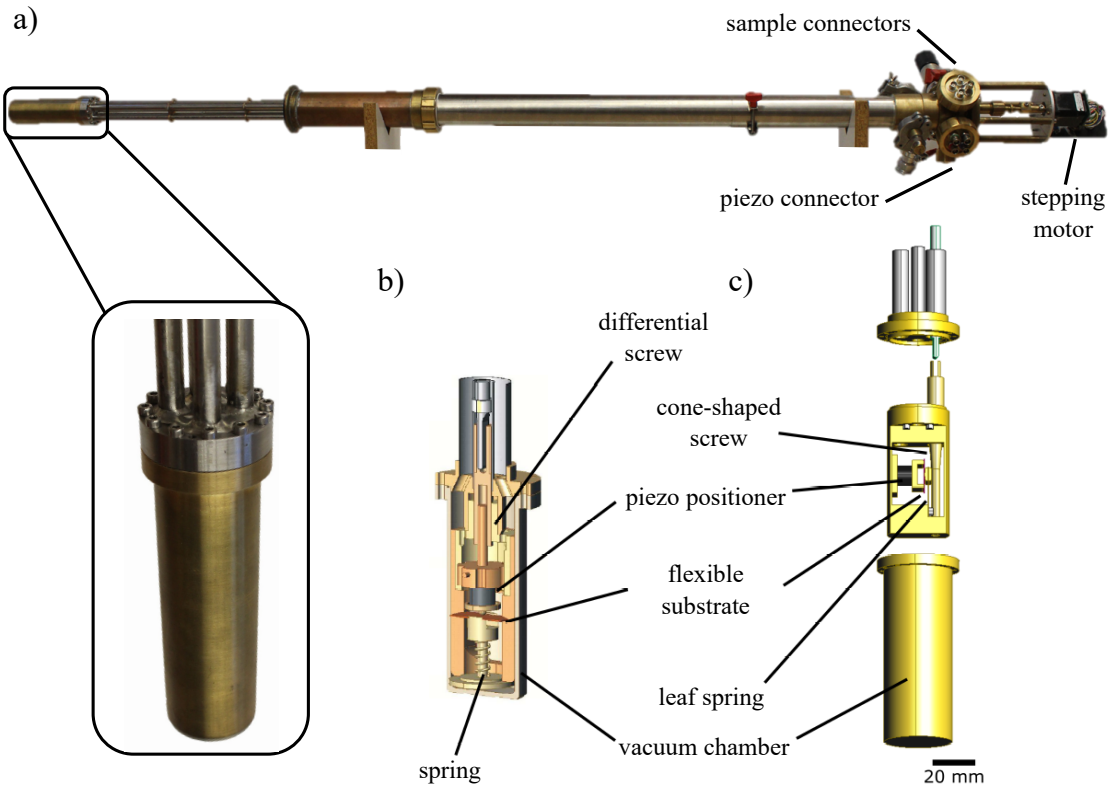

Figure 3.15: *(a) The custom-built low-temperature MCBJ sample holder with zoom-in of the head. Photo from Ref. 65. (b,c) Two different builds of the sample holder head, containing the differential screw (b) or the cone-shaped screw (c). Schematics taken from Ref. 34.*

vacuum chamber. In the end, the sample is cooled down to cryogenic temperature by immersing the setup rod in a liquid helium dewar. Measurements in cryogenic temperatures provide a way to improve the stability of the atomic wire by freezing the thermal motion of the atoms. Furthermore, low-temperature measurements are crucial for high-purity measurements since the risk of contamination of the junction is decreased, as any contaminating residual molecules that could remain after evacuation condense on the cold surfaces of the setup walls. To ensure the high purity of the junction area, the sample is first broken after cooldown. The stepper motor rotates either the differential screw or the cone-shaped screw to bend the flexible substrate to the point where the notched wire fully breaks. The fine-tuning of the junction size, thus tuning the conductance, is executed by a piezo positioner. The LabVIEW measurement program for controlling the motor and piezo positioners, as well as obtaining the $I(V)$ characteristics of the notched-wire samples was developed by András Magyarkuti [65]. The measurement circuit follows the schematic presented in Fig. 3.13, with typical serial resistance values $R_s < 1$ kΩ.

3.2.3 AgI-based scanning tunneling microscopy break-junction (STM-BJ)

In my analysis, I will use the measurements of Botond Sánta and Dániel Molnár on AgI-based scanning tunneling microscopy point-contact (STM-PC), created with STM break-junction (STM-BJ) technique, to compare the characteristics and statistics of my pure atomic switchings to the ECM-type switchings. Such samples demonstrated high-speed memristive switching within nanosecond time scale [16, 62] with a measurement setup specifically developed for high-frequency operations.

The samples were made by Botond Sánta. The preparation starts with the SiO_2 substrate, a 12 nm Ti sticking layer, and > 80 nm Ag evaporated on top of that. The AgI thin layer is created by exposing the Ag layer to iodine vapor at 40°C and ambient pressure for 30 s [16, 66].

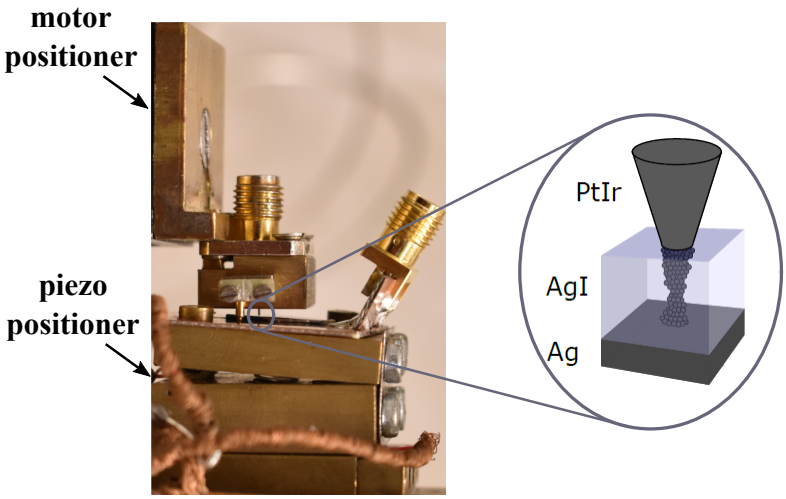

Figure 3.16: *The photo of the STM-BJ setup, and an illustration of the AgI-based STM-PC created. AgI is formed after exposing the Ag layer to iodine vapor; the filament is built between the PtIr STM tip and the Ag layer in the first voltage sweep. Images are from Ref. 62.*

The resulting photosensitive sample is built into a room-temperature STM-BJ setup with particular attention to avoid exposing it to light. Then the setup is pumped down to 10^{-2} mbar pressure. The PtIr STM tip is approached and even slightly pushed into the sample. The first voltage sweep creates the Ag filament; therefore, an extra electroforming step is unnecessary. Fig. 3.16 depicts the photo of the used STM sample holder on the left, and the illustration of the memristive filament formed during the measurements. The current-voltage curves are measured in the same arrangement of Fig. 3.13, the piezo and motor positioners are used for fine and coarse tuning, and the measurement is controlled by the same program as in the case of the notched-wire MCBJ samples with typical serial resistance values $R_s < 1$ kΩ.

3.2.4 Nanofabricated, electromigrated Ag_2S samples

In this chapter, I will also introduce an ECM-type sample exhibiting fundamentally different switching characteristics in the atomic scale and nanoscale, observed with a high-stability on-chip sample fabricated and measured by László Pósa [63, 64]. The sample fabrication starts on a Si_3N_4 layer with a thickness of 140 nm on top of a Si/SiO_2 chip. The nanofabrication involves electron beam lithography and electron beam physical vapor deposition of 40 nm thick Ag on the substrate. The resulting pattern has a 100 nm wide and 45 nm thick constriction, depicted in Fig. 3.17(a), which is further narrowed by controlled electromigration [63, 67]. The electromigration is performed by applying 100 µs long consecutive voltage

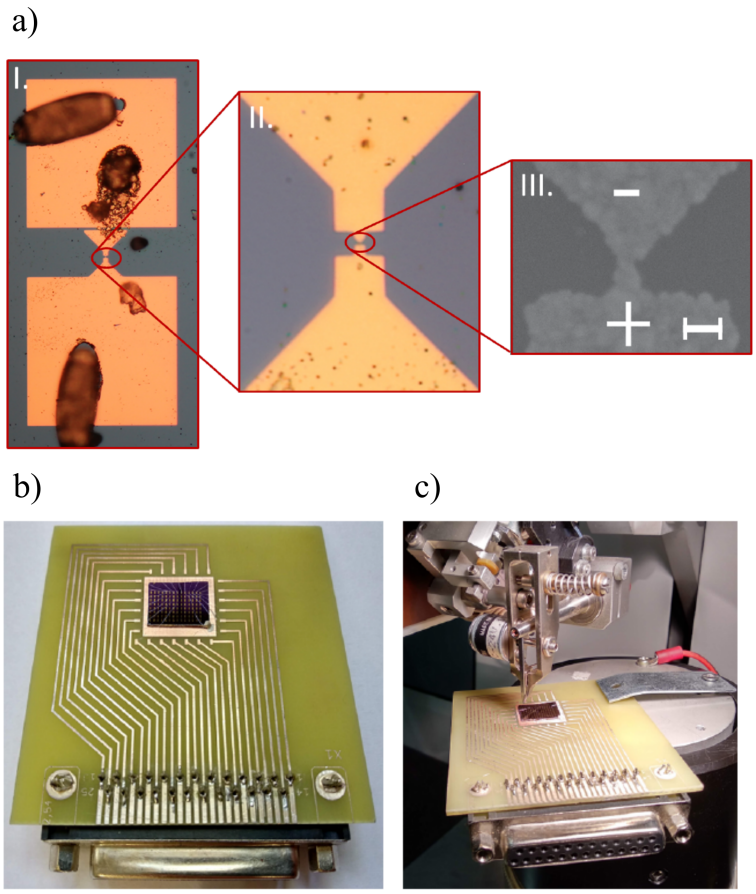

Figure 3.17: *(a) Optical (I-II.) and scanning electron microscope (III.) picture of the nanofabricated planar sample. Polarity and a scale bar of 200 nm are indicated on the scanning electron microscope image. (b) Printed circuit board with fixed sample on top. (c) Electrical connections from the sample pads to the copper leads are created by wedge bonding. All photos taken from Ref. 64.*

pulses with gradually increasing amplitude while the resistance is monitored closely. As the electromigration process evolves, the diameter of the constriction becomes narrower until a small nanogap is formed, and the resistance increases abruptly. The feedback-controlled electromigration procedure is similar to the sample fabrication

of Ref. 48 (see pure atomic switching measurements in Fig. 3.7) with the significant difference that the samples of László Pósa are fabricated and measured at room temperature, and undergo the next step: sulfurization. This step involves the exposure of sulfur vaporized at 60°C and ambient pressure. Herewith, Ag_2S is formed in the nanogap, establishing the switching medium for an electrochemical metallization cell. A number of the described sample designs are arranged in a matrix structure on the substrate chip, which is then fixed on a printed circuit board (panel (b)). The individual samples are connected to the Cu leads by wedge bonding (panel (c)). The printed circuit board is mounted in a sample holder and vacuum-pumped, as the samples are air-sensitive. The sample holder is connected to a switch box equipped with electrostatic discharge (ESD) protection, where the sample connections can be switched to the ground with a serial 1 MΩ resistance. Conductance is measured with the C# control program written by László Pósa [64]. The circuit schematic is the same as presented in Fig. 3.13; however, since the atomic-size junction is created by the electromigration steps and the stability is exceedingly high in the planar sample, there is no need for piezo and motor positioners. The typical serial resistance is $R_s = 50\ \Omega$. Although the described sample fabrication method results in high mechanical stability, the yield of working samples is not outstanding. This fact contributed strongly to the motivation to develop an alternative room-temperature nanofabricated break-junction sample design described at length in Section. 3.4.

3.3 Characterization of pure atomic switching

When a memristive device is operated at the atomic scale, atomic processes may govern the transport, see for example the breaking traces in Fig. 3.4 exhibiting two distinct behaviors in the same ECM-type memristor. My research was motivated by similar observations in memristive systems made in our research group. The first such measurements were reported by Geresdi *et al.* [15] who presented experiments in Ag_2S-based memristors with two distinct switching behaviors. The investigated system was a STM-PC sample of sulfurized thin Ag which showed a clear transition from the well-known ECM-type switching characteristics in the nanoscale, i.e., higher conductance regime, to fundamentally different characteristics at an atomic-sized regime. The two panels of Fig. 3.18 demonstrate typical current-voltage characteristics with clear distinguishing features.

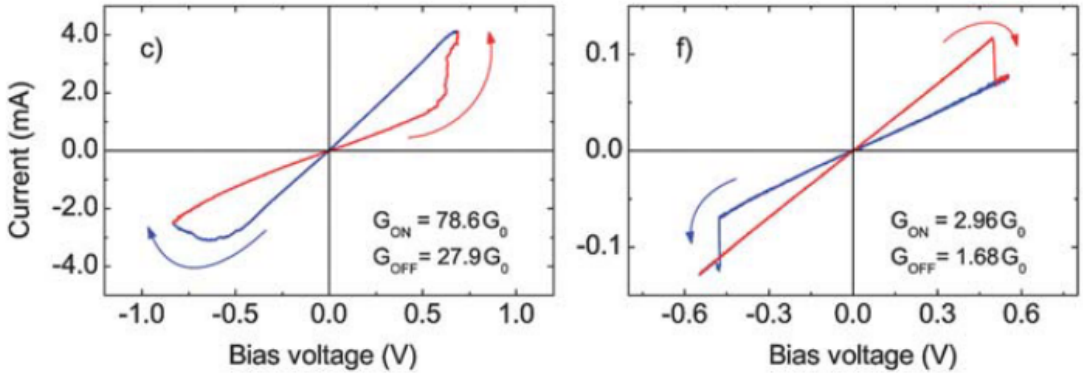

Figure 3.18: *ECM-type nanoscale (a) and fundamentally different atomic-scale (b) current-voltage characteristics observed in the same Ag_2S-based memristor sample at different conductance ranges. Results from Ref. 15.*

Similarly, László Pósa also observed two different resistive switching characteristics in Ag_2S-based devices. His sample was a nanofabricated device (fabrication technique presented in Section 3.2.4) that provides adequate stability for room-temperature measurements. Reproducing current-voltage characteristics of 20 switchings distinctive for ECM-type switching in the nanoscale, and a distinct switching behavior in the atomic-sized regime are depicted in Fig. 3.19(a) and Fig. 3.19(b), respectively.

In both of these results, the nanoscale switching behaves as a conventional ECM-type device, while the atomic scale resembles the pure atomic switching characteristics of e.g., Yoshida *et al.* in Fig. 3.7 [48]. Both measurements investigated Ag_2S-based memristors, meaning that the important requirement of pure atomic switching, namely a switching observed in a pure metallic system, was not fulfilled, and the role of the embedding Ag_2S matrix in the switching is unclear.

Based on these presented results, it is clear that atomic switching is not restricted to pure metallic nanowires and that it may also become important in conventional ECM cells, once atomic size scales are reached. For this reason, it is of fundamental importance to explore the differences between pure atomic and ECM-type switching

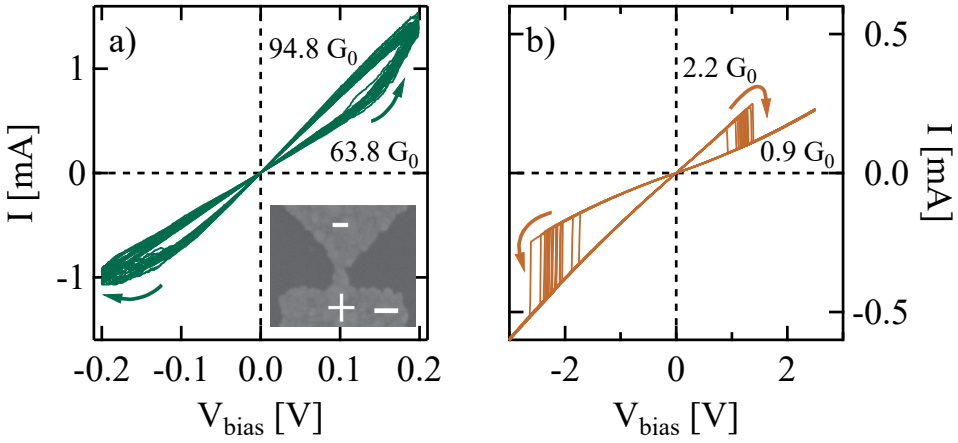

Figure 3.19: *Reproducing room-temperature current-voltage characteristics in the nanoscale (a) and the atomic scale (b) of the Ag_2S-based ECM-type device. The labels indicate the corresponding HCS and LCS conductances. Measurements by László Pósa. Published in Ref. P1.*

and to understand the physical mechanisms governing the former phenomenon. Although a broad range of material systems exhibit ECM-type switching, Ag plays a prominent role as an active material in such devices which has not been investigated in terms of pure atomic switching. To this end, in this Section, I compare the pure atomic and ECM-type switching characteristics, and to achieve an unquestionable distinction between the two types of phenomena, the pure atomic switching is explored in ultrapure-silver nanowires, where ECM processes can be excluded. During my research, I conducted a large number of measurements on notched-wire Ag MCBJ samples at low temperatures with the sample fabrication and measurement technique introduced in Section 3.2.2. I investigated the extensive statistics of reversible pure atomic switching, focusing on the threshold voltage variation and the voltage-time dilemma. I chose to compare the pure atomic switching properties and characteristics to an AgI-based memristive STM-BJ system (fabrication technique presented in Section 3.2.3), to which I received the raw data of a large statistical set of current-voltage characteristics from Botond Sánta and Dániel Molnár. I also received from them the raw data of the voltage-time dilemma concluded in Fig. 2.3 from Ref. 16. Additionally, I processed the measurement data by László Pósa on the Ag_2S-based sample already presented in Fig. 3.19. Finally, working together with Zoltán Balogh and Máté Vigh, we proposed a vibrational-pumping model of the pure atomic switching process, which consistently describes the observed phenomena. The results of this Section are summarized in Ref. P1 and in Thesis Statement I.

3.3.1 Statistical analysis of pure atomic switching versus electrochemical metallization cell type switching

In order to clearly distinguish its characteristic switching features of pure atomic switching, I compare its properties to the AgI-based memristive system. The first step of this comparison regards individual curves and cycle-to-cycle variation of

current- and conductance-voltage characteristics summarized in Fig. 3.20. The analysis will use consistent red (blue) color coding for pure atomic (ECM-type) switching. The illustrations for the two systems, notched-wire Ag MCBJ and AgI-based memristive STM-BJ, are shown in panels (d)-(e). The $I(V)$ curves in panels (a)-(c) exhibit typical pure atomic switching behavior with linear characteristics of atomic-sized conductances, and jump-like switching at stochastic voltages, and common asymmetry in the set and reset voltages. This behavior is consistent with switching between discrete atomic configurations. In contrast, the ECM-type switching in panel (f) exhibits a gradual transition between the conductance states during switching, the well-defined threshold of the switching, and the analog multilevel programming characteristic for memristive memories.

Another important aspect to compare is the direction of the switching which is understood by considering the asymmetric conditions in the system. For a typical ECM device, the switching direction is well-defined by the compositional difference of the active and inert electrodes. The set transition occurs with a positive voltage on the active electrode which starts the redox reaction of the active material. In the case of an ECM cell with compositional symmetry, the switching direction is determined by the geometrical asymmetry present at the apex of the junction which induces an inhomogeneity of the local electric field [63]. Therefore, it is essential to define a bias polarity convention for the STM-BJ setup, which says that the positive bias corresponds to a positive voltage applied to the sample with respect to the STM tip. This definition coincides with the compositional asymmetry of the Ag/AgI/PtIr setup where the active electrode is the sample, and thus, the set transition always occurs at positive polarity. For pure atomic switching, there is no compositional asymmetry, and therefore, the direction of the switching is given by geometrical asymmetry, and since the system has no macroscopic asymmetry, the atomic-sized geometry of the active region is relevant. Therefore, pure atomic switchings show stochastic direction from junction to junction defined by the local geometry.

The switchings depicted in this panel (f) originate from the voltage-time dilemma analysis presented in Fig. 2.3(b) [16], demonstrating the analog increase of the $G_{\mathrm{HCS}}/G_{\mathrm{LCS}}$ conductance ratio tuned by the increase of the driving voltage (indicated in the legend). This analog behavior is not characteristic of pure atomic switching, where the rise in voltage does not change the stable conductance until a threshold for another atomic jump is reached, and occasionally, this yields reproducible switching between multiple conductance states as demonstrated in the example of panel (c).

The study of the cycle-to-cycle variation, shown in panel (g), provides another difference between the two types of switchings. In this figure, 20 consecutive $G = I/V$ conductance versus voltage curves demonstrate switchings with similar threshold voltages in both systems. It is a remarkable difference that the pure atomic switching exhibits fundamentally stochastic threshold voltage with a broad distribution. At the same time, the memristive system shows a better defined threshold voltage with smaller deviations of the seemingly reproducible curves. The numerical values of the relative deviations $|\Delta V_{\mathrm{thr}}/\overline{V}_{\mathrm{thr}}|$ show more than twofold greater deviations for pure atomic switching, 6.2% (7.8%) for the set (reset) and

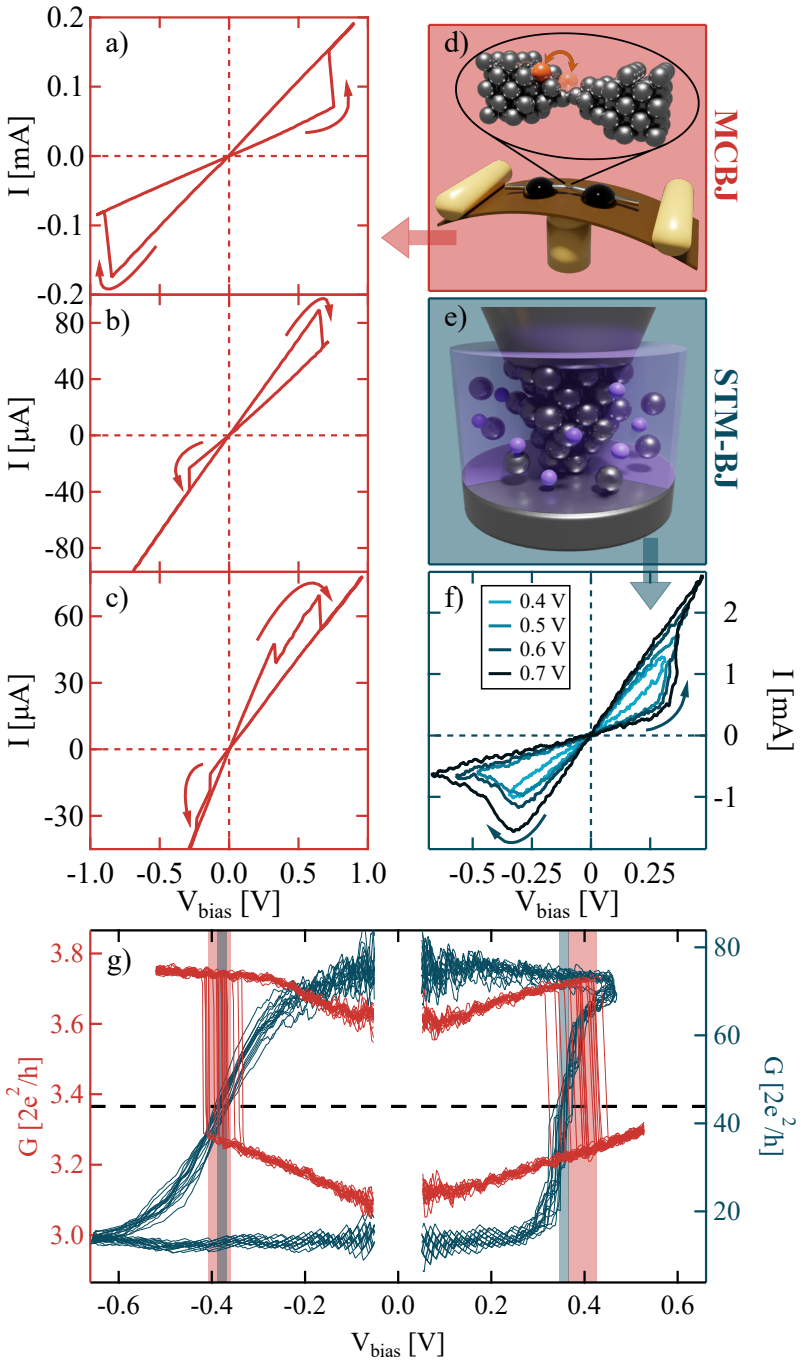

Figure 3.20: *Characteristics of pure atomic and ECM-type memristive switching. (a-c) Representative pure atomic switching current-voltage characteristics. (d-e) Illustration of the MCBJ and STM-BJ samples used in the comparison. (f) Analog multilevel programming characteristics for memristive switching where the legend shows the applied driving voltage. (g) Conductance-voltage characteristics of reproducible pure atomic switching (red) and memristive switching (blue) to compare the cycle-to-cycle variation. The shaded areas indicate the standard deviations of the threshold voltages. Published in Ref. P1.*

symmetric values of 2.7% for the well-defined memristive switching.

As a next step in the comparison, the device-to-device variation is discussed based on the mean values of 35 (38) independent switchings, each consisting of a median number of 100 (200) reproducible cycles for pure atomic (memristive) switching. Fig. 3.21 illustrates the mean threshold voltages of set transitions (circles) and reset transitions (squares) of the pure atomic (red) and ECM-type (blue) switchings as a function of the mean initial conductance (LCS (HCS) for set (reset) transitions). The right panel of Fig. 3.21 shows the corresponding histogram of the threshold voltages. For the cycle-to-cycle variation, it was previously observed

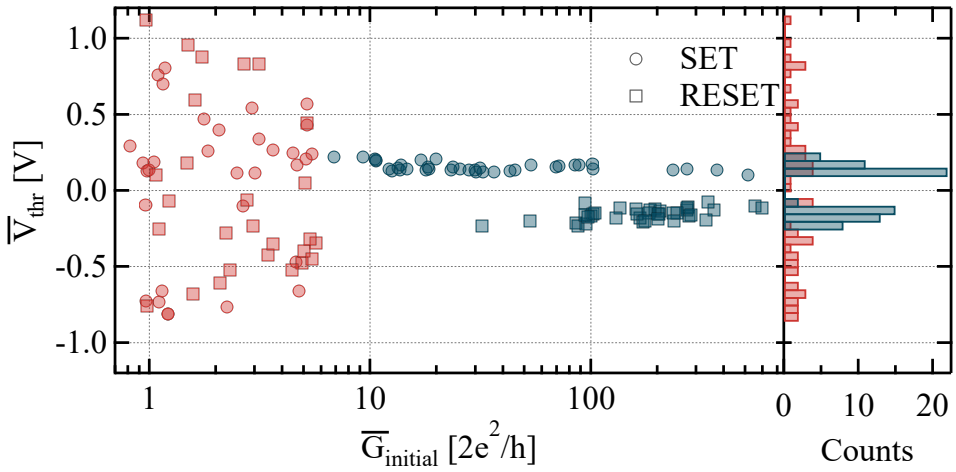

Figure 3.21: *Device-to-device variation of the threshold voltage as a function of the initial conductance of independent pure atomic switchings (red) and AgI-based memristive switchings (blue). The histogram on the right emphasizes the clear difference in the distributions of threshold voltages. Published in Ref. P1.*

that there is a huge difference in the distribution of the threshold voltage, which holds for device-to-device variation as well. The ECM-type switching exhibits well-defined and relatively low threshold voltages around ±155 mV, whereas the pure atomic switching values show a wide distribution exhibiting order-of-magnitude device-to-device differences up to ±1 V. In comparison, the atomic-scale switching in Fig. 4.11(b) on the more stable nanofabricated sample exhibits even higher thresholds, which implies that the limited stability of the break-junction arrangement could play a role in limiting the achievable threshold voltage. Additionally, this comparison reinforces the observation about the switching direction being well-defined for ECM-type (the set transition occurs at positive voltage) and stochastic for pure atomic switching.

Further analysis of the difference and ratio of the conductance states of pure atomic switching can be compared to literature and the memristive system. Fig. 3.22(a) presents the correlation plot of the G_{HCS} and G_{LCS} conductances, revealing an average of $\Delta G = 0.4\ G_0$ jump height which is in line with the average values found in literature: all in the range of $0.3 - 0.4\ G_0$ for Al [50], Pb [52], Au [52] and Cu [53]. Jumps between the preferred conductance states of Ag (at peak positions in the conductance histogram, see Fig. 3.3) were not observed. Still,

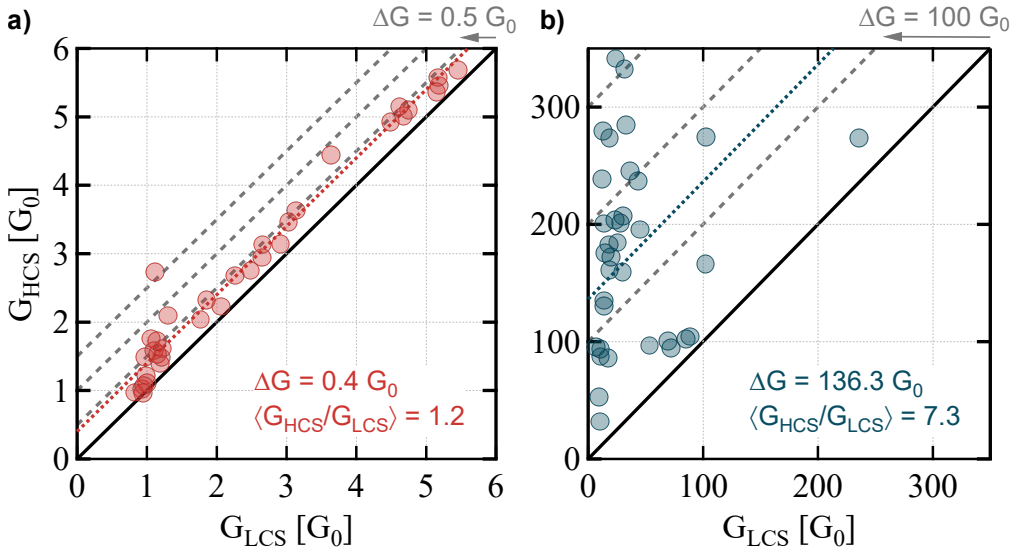

Figure 3.22: *Correlation plots of the G_{HCS} and G_{LCS} conductances for the pure atomic (a) and memristive (b) switchings. The dashed lines guide the eye for offsets of 0.5, 1, 1.5 G_0 (a) and 100, 200, 300 G_0 (b). The colored dashed lines indicate the average offset of 0.4 G_0 (a) and 136.3 G_0 (b).*

there is a pronounced clustering of data around 1 G_0, which the increased stability of the single-atom junction can explain. Such clustering at the preferred conductance states was also reported for Au [52]. Further comparison to the AgI-based system plotted in Fig. 3.22(b) shows that the conductances of the investigated memristive switchings vary over a larger range with the average jump height being $\Delta G = 136.3\ G_0$. The memristive system shows an average conductance ratio of $G_{\mathrm{HCS}}/G_{\mathrm{LCS}} = 7.3$, a 6-fold difference to pure atomic switching.

Another intriguing question is how the conductance dependence of the current and voltage threshold compares to the various other materials investigated by Ring *et al.* [60] (see summary of their work in Section 3.1). For the proper comparison, I use Fig. 3.10(e)-(f) for the background, and scale my measurements on top of that, the resulting plot is presented in Fig. 3.23. The data is grouped and averaged based on the corresponding initial conductance in bins of $G_{\mathrm{initial}} \pm 0.5\ G_0$ to show the trends more evidently. The mean current (voltage) thresholds of independent Ag pure atomic switching are plotted with brown color, which closely coincides with the Au data, expect for the last bin. The significantly lower number of switching data for Ag at the 6 G_0 bin could explain the deviation from the otherwise increasing trend. The threshold current shows a monotonous increase for all materials, with Au and Ag having the strongest dependence on the conductance. The threshold voltage slightly decreases, with the exception of Au. The authors explain that behavior with the switching threshold distribution showing multiple maxima due to different possible configurations and the stochastic nature of the switching.

The investigation of the device-to-device variation only included data obtained at 100 Hz driving frequency. Consequently, the next step is to expand the analysis to the time dependence of the switchings. For further comparison, the sweep rate

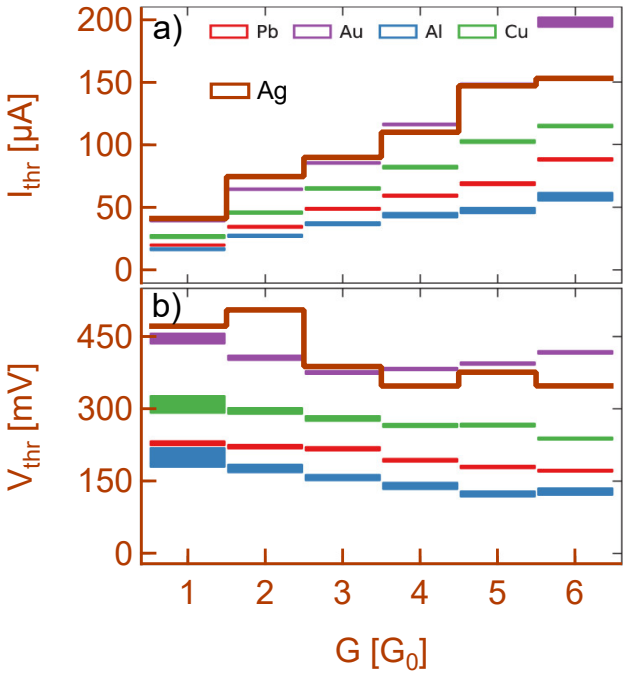

Figure 3.23: *Size-dependent statistical analysis of mean threshold current (a) and voltage (b) of independent measurements compared to the results of Ring et al. [60]. My results on Ag are indicated with brown color, which is drawn on top of the plot from Ref. 60. Initial conductance is grouped in bins of* $G_{\text{initial}} \pm 0.5\ G_0$.

seems to be the appropriate quantity to describe the traversed bias voltage on the sample, calculated as $4 \cdot V_{\text{ampl}} \cdot f$ where V_{ampl} is the maximum amplitude of the bias voltage on the sample. Note that the applied voltage might be asymmetrical (see Fig. 3.19(b)); thus, the sweep rate is calculated separately for the negative and positive sides. Furthermore, even with a symmetrical applied voltage, the V_{ampl} bias voltage depends on the sample resistance and can considerably differ in the two conductance states, especially if the serial resistance is not neglectably small with respect to the junction resistance.

The voltage-time dilemma, the connection between the switching speed and driving voltage, is a widely researched topic for memristive systems [6, 16, 68] (see Fig. 2.3). However, no results regarding pure atomic switching are available, therefore one of my goal was to investigate the voltage-time dilemma in the pure Ag break-junctions. Fig. 3.24 presents the mean threshold voltage as a function of the sweep rate of selected representative atomic switchings (red) and AgI-based memristive data (blue). In all measurements, the linearly increasing voltage threshold corresponds to exponentially increasing sweep rate which is highlighted by the linear fits on the linear-logarithmic scale. It is evident that the pure atomic switchings exhibit an increasing slope with increased threshold voltage. Compared to the identical voltage range, the AgI-based memristive switching clearly shows a

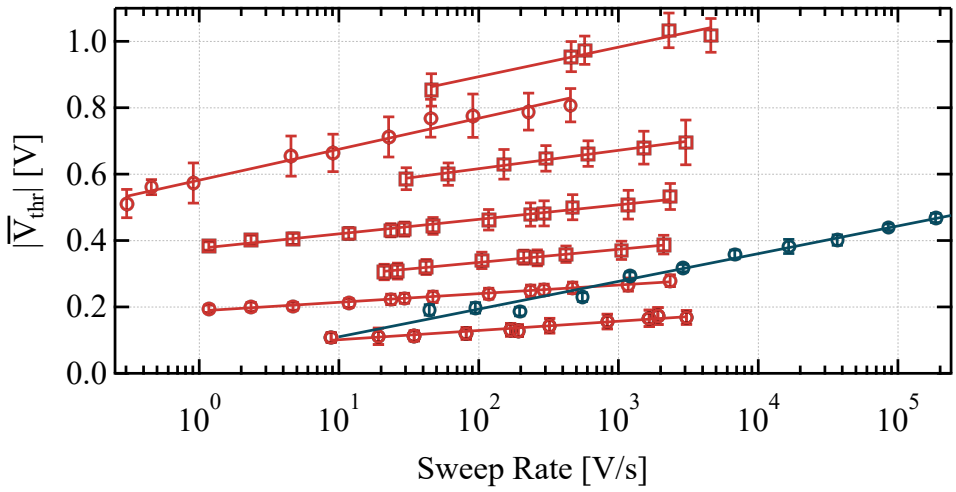

Figure 3.24: *Sweep rate dependence of the threshold voltage of representative atomic switchings (red) and AgI-based memristive switchings (blue). The memristive data is obtained from Fig. 2.3(a) [16]. The error bars denote the cycle-to-cycle standard deviation. The linear fits on the linear-logarithmic scale highlight the exponential dependence on the sweep rate. Published in Ref. P1.*

relative increase of threshold voltage over the sweep rate that is more than twice as large. Whereas, there are also examples, where an Ag-based ECMS exhibits $\approx$ 100% relative increase of the threshold voltage within one decade along the temporal axis [69–71].

Further quantitatively analysis of the sweep-rate-dependent slope and cycle-to-cycle variation of pure atomic switching in pure Ag nanowires will follow in the next section in Figs. 3.34 and 3.35 where the experimental data is compared with model calculations.

3.3.2 Theoretical model and numerical simulations of atomic switching

After the detailed statistical analysis of pure atomic switching in pure Ag nanowires, the next goal of my work was to find a theoretical approach to describe the observed features of pure atomic switching. The presented approaches described in Section 3.1 consider current-induced forces and runaway phonon modes. They simulate specific atomic arrangements and have high computational costs to achieve a reasonable description of the variability of the contacts. My goal was to describe the statistical observation characteristic for pure atomic switching: a significant stochastic cycle-to-cycle variation and a comparatively weak sweep rate dependence of the threshold voltage which could mean a extremely high computational cost if simulated by the models present in literature. Instead, I will present the theoretical approach based on the single-level vibrational pumping model of Ref. 72, which is similar to the runaway phonon pumping of Ref. 60 (Fig. 3.11) but significantly simpler. I will show that the results of this simple vibrational pumping model can generally describe the cycle-to-cycle variation and the sweep rate dependence observed in

the measurements which support the validity of the model in these two aspects of the switching characteristics.

To begin with, I review the contributions made towards developing the theory and simulations. The presented model is based on the conventional vibrational pumping model [72–74]. The principles of the single vibrational level model are presented in the work of Paulsson *et al.* [72] that provides the basics to derive the voltage-dependent probabilities of phonon excitation and absorption. I wrote the first simulation code, which evolved the phonon occupation by considering the probabilities in every time step while increasing the applied voltage. Similarly to stochastic simulations, the computational costs were relatively high as a reliable result is given by constant repetition of samples. Máté Vigh suggested using the Markov chain approach to describe the evolution of vibrational energy as a random walk along a one-dimensional energy ladder, which dramatically decreased the simulation time by implementing the analytical formula of the first passage time, yielding mean value and variation. However, at this point, the model was not entirely consistent with the measurements, as this conventional Markov chain model did not account for sweeping the voltage, basically describing a fixed voltage measurement. In the following, Zoltán Balogh revised the formulas from the Markov chain model, implemented a solution for sweeping the voltage, and made changes to speed up the calculation. From this point forward, he wrote and executed the simulation codes. In the following, the details of the theoretical background and the thorough description of this final simulation will be described.

Vibrational pumping model

The basic idea of the model is presented in Fig. 3.25: two meta-stable junction configurations are considered, which are described by a double-well potential.

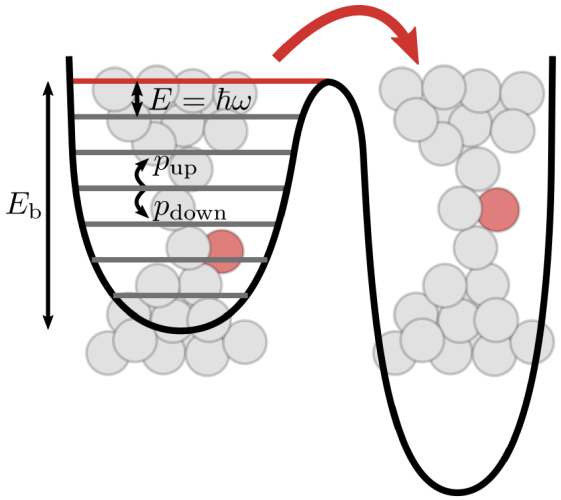

Figure 3.25: *Pure atomic switching is attributed to the atomic rearrangement (a), which is energetically described as a double-well potential where the phonon occupation ladder has to be climbed to trigger the switching (b). Published in Ref. P1.*

At a certain voltage, the final state is considered as the more stable (lower

energy) configuration. However, an energy barrier of E_b must be reached for the switching. For this, the electrons cannot transfer enough energy to the switching atom within a single scattering process, however, multiple scattering events may pump the proper vibrational mode, described by energy quanta $E = \hbar\omega$. The model describes the voltage-induced evolution of the vibrational energy states as a random walk along the energy ladder, described by $p_\mathrm{up}(\Delta\mathrm{t})$ and $p_\mathrm{down}(\Delta\mathrm{t})$ upward and downward jump probabilities within a time-step Δt.

As a first approach to obtain the transition probabilities, one can take the possible electron-phonon scattering processes into account. Let's consider the electron transport of a single-channel perfectly transmitting junction between two electrodes at an applied V voltage. Fig. 3.26 illustrates the zero temperature Fermi functions of the electron reservoir on the left and right side of the junction, also considering the direction of the electrons (see arrows and colors). In the zero temperature case of a perfectly transmitting channel, only four scattering processes are possible, which are resolved in Fig. 3.26: a phonon excitation process in panel (a), and three different phonon absorption processes in panel (b)-(d). To estimate the probabilities for these processes, the Fermi functions of the initial and final state have to be considered. The Fermi function $f(\varepsilon)$ is a probability that an electron occupies the state with ε energy, whereas $1-f(\varepsilon)$ is the probability of the state being vacant. Therefore the probability of any process is given by $p \sim \int f(\varepsilon_\mathrm{initial})\,(1 - f(\varepsilon_\mathrm{final})\,\mathrm{d}\varepsilon$. Additionally, the occupation number of the vibrational mode n has to be considered to obtain the results indicated on the right. Summarizing these expressions, the probability of transferring energy to the phonon system is expressed as

$$p_\mathrm{up} \sim (n+1)\,(eV - E)\,, \tag{3.6}$$

while the probability of absorbing energy from the phonon system is

$$p_\mathrm{down} \sim n\,(eV + 3E)\,. \tag{3.7}$$

It will be shown, that these probabilities already give a good description of the vibrational pumping probabilities with a single missing term, which describes the relaxation of the vibrational mode towards the phonon bath. A more general and complete description is given by the single vibrational level model of Ref. 72 which I use to derive the p_up and p_down probabilities including the latter phonon relaxation and the detailed prefactors. The one-level model offers analytical formulas derived from the lowest-order expansion of the self-consistent Born approximation for the conduction, including the phonon scattering. Here, the results for a single fully open transmission channel are presented. The calculations give the power dissipated by the electrons into a single vibrational mode as:

$$P = \gamma_\mathrm{eh} E\,[n_B(E) - n] + \frac{\gamma_\mathrm{eh}}{4}\frac{\left[\cosh\left(\frac{eV}{kT}\right) - 1\right]\coth\left(\frac{E}{2kT}\right)E - eV\sinh\left(\frac{eV}{kT}\right)}{\cosh\left(\frac{E}{kT}\right) - \cosh\left(\frac{eV}{kT}\right)}, \tag{3.8}$$

where n_B is the Bose-Einstein distribution, n is the occupation number of the vibrational mode, γ_eh is the electron-hole damping rate (the electron-phonon

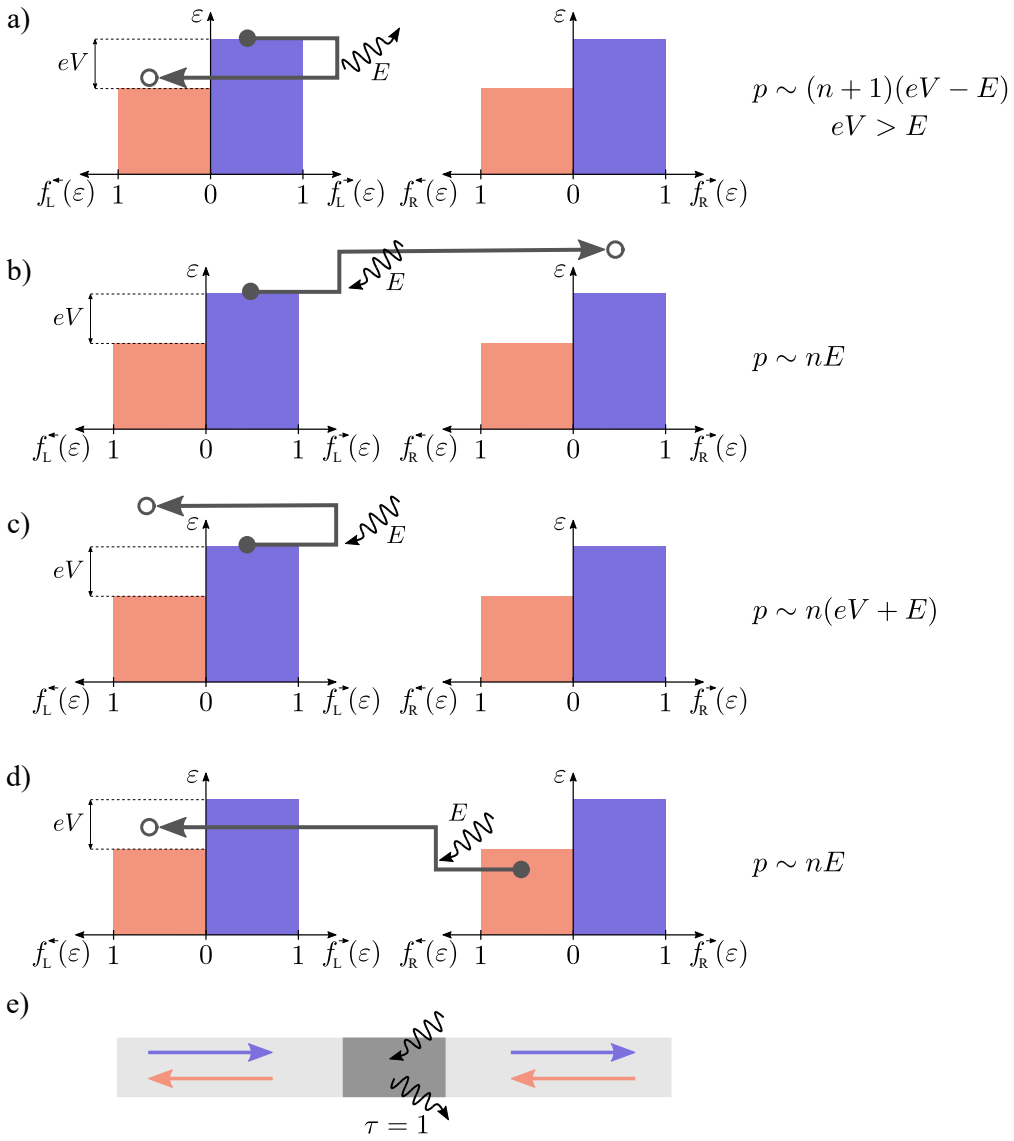

Figure 3.26: *Illustration of the scattering processes at $T = 0$ K (a-e) between the left and right leads of a single-channel perfectly transmitting junction schematically presented in panel (e). The Fermi-Dirac distributions on the left (right) side indicate the left (right) electrode. The direction of the electrons, i.e., $+k$ (rightmoving) and $-k$ (leftmoving) is differentiated by blue and red colors, respectively. The phonon excitation and absorption processes cause small perturbations, so their effect on the distribution function is not considered. Circles denote the electrons, and wavy arrows illustrate phonons with the energy E. (a) Phonon excitation that is only possible at $eV > E$. (b-d) Three different phonon absorption processes. The probabilities for each process are indicated on the right. (e) Schematic illustration of the junction between the two electrodes. The dark gray colored area represents the single-channel perfectly transmitting junction where electron-phonon interactions can take place.*

coupling strength), and $E = \hbar\omega$ is the energy quantum of the vibrational mode. From this, the rate, at which the occupation number changes is obtained as:

$$\nu = \frac{P}{E} + \gamma_{\mathrm{d}} \left[n_B(E) - n \right], \tag{3.9}$$

where the γ_{d} external damping rate describes the relaxation of the vibrational mode towards the phonon bath (phonon-phonon relaxation strength). In the calculation, the case of $eV > E$ in the zero temperature limit of this model is considered, yielding

$$\nu = \underbrace{\left[\frac{\gamma_{\mathrm{eh}}}{4E} (n+1) (eV - E) \right]}_{\nu_{\mathrm{up}}} - \underbrace{\left[\frac{\gamma_{\mathrm{eh}}}{4E} n \left(eV + \left(3 + 4\frac{\gamma_{\mathrm{d}}}{\gamma_{\mathrm{eh}}} \right) E \right) \right]}_{\nu_{\mathrm{down}}}, \tag{3.10}$$

where the formula is already decomposed for the excitation processes, where the occupation number increases (ν_{up}) or the relaxation processes, where it decreases (ν_{down}). Note that these terms contain the probabilities Eq. (3.6)-(3.7) estimated based on the scattering processes in Fig. 3.26 but additionally include the phonon-phonon relaxation term and the exact prefactors. My notation uses a dimensionless electron-phonon interaction rate, $r = \gamma_{\mathrm{eh}} h / 8E$, and the $\gamma = \gamma_{\mathrm{d}} / \gamma_{\mathrm{eh}}$ normalized external damping rate, yielding the

$$p_{\mathrm{up}}(\Delta \mathrm{t}) = \frac{2Mr\Delta t}{h} (n+1) (eV - E), \tag{3.11}$$

and

$$p_{\mathrm{down}}(\Delta \mathrm{t}) = \frac{2Mr\Delta t}{h} n \left(eV + (3 + 4\gamma) E \right), \tag{3.12}$$

formulae for the upward and downward jump probabilities along the energy ladder (see Fig. 3.25). Note, that these probabilities already include a multiplication factor of M generalizing the model for M open conductance channels instead of the original single-channel situation. Lastly, the possibility of no event occurring has to be considered while satisfying the relation

$$p_{\mathrm{up}}(\Delta \mathrm{t}) + p_{\mathrm{down}}(\Delta \mathrm{t}) + p_{\mathrm{rest}}(\Delta \mathrm{t}) = 1. \tag{3.13}$$

Note, that the results of the simulation are insensitive to the Δt timestep, however, Δt should be sufficiently small to satisfy the $p_{\mathrm{up}}(\Delta \mathrm{t}) + p_{\mathrm{down}}(\Delta \mathrm{t}) < 1$ condition. In the simulations, Δt was typically in the range of $10^{-14} - 10^{-17}$ s.

The phonon energy quantum in the simulation is $E = 13.1$ meV, which is determined in agreement with the criteria for the homology of forces [75]

$$\left\langle E_{\mathrm{Ag}} / E_{\mathrm{Cu}} \right\rangle = \left\langle \left(\sqrt{ma^2} \right)_{\mathrm{Cu}} / \left(\sqrt{ma^2} \right)_{\mathrm{Ag}} \right\rangle = 0.679, \tag{3.14}$$

where m is the molecular mass, a is the lattice constant and $E_{\mathrm{Cu}} = 19.3$ meV is based on the simulated mean value of the phonon energy quantum of Cu atomic wires [60].

At any applied voltage, a steady-state phonon occupation $\overline{n}$ can be achieved at the condition when there is a balance between the excitation and relaxation ($p_{\mathrm{up}} = p_{\mathrm{down}}$). From the single-level model [72], the current of the perfectly transmitting single-channel junction can be expressed with the average phonon occupation number $\overline{n}$:

$$I = \frac{2e^2}{h}V - \frac{e\gamma_{\mathrm{eh}}}{4E}\left(2e\overline{n}V + \frac{E-eV}{\mathrm{e}^{\frac{E-eV}{kT}}-1} + \frac{E+eV}{\mathrm{e}^{\frac{E+eV}{kT}}-1}\right). \tag{3.15}$$

The expression consists of the Landauer formula with the conductance quantum $G_0 = 2e^2/h$ and a correction term due to electron-phonon interaction. Let's start by considering the regions $eV < E$ and $eV > E$ separately. For voltages when eV is below the vibrational quantum energy, the voltage does not suffice to excite phonons, the correction terms disappear, and the conductance is voltage-independently 1 G_0. For voltages when eV is higher than the vibrational quantum energy, the electrons can start to excite the vibrational mode (see panel Fig. 3.26(a) demonstrating the relevant scattering process).
In the zero temperature limit, the current expression takes the following form:

$$I = \frac{2e^2}{h}V - \frac{e\gamma_{\mathrm{eh}}}{4E}\left(2e\overline{n}V - E + eV\right). \tag{3.16}$$

Consequently, the differential conductance is expressed with the voltage-dependent average phonon occupation $\overline{n}(V)$ and the electron-phonon interaction rate r as

$$\frac{\mathrm{d}I}{\mathrm{d}V} = \frac{2e^2}{h}\left(1 + \frac{r}{2(\gamma+1)} - r\right) - \frac{2e^3 r}{hE(\gamma+1)}V. \tag{3.17}$$

The differential conductance exhibits linear dependence on the voltage with a slope of $-2e^3r/(hE(\gamma+1))$. The resulting shape of the differential conductance is illustrated for a perfectly transmitting single channel in Fig. 3.27 in this simplified picture of considering both regions separately. Experimentally, the transition at $eV = E$ is smeared due to the finite temperature [72, 76, 77]. The jump-like decrease at the voltage corresponding to $eV = E$ is explained by the sharp onset of phonon excitations, as soon as eV exceeds the vibrational quantum energy. The height of this jump can be calculated by substituting $V = E/e$ into the equation. In the limit of no local phonon heating $\gamma \to \infty$, the jump height is directly described by the r dimensionless electron-phonon interaction rate, representing the rate of the scattering of electrons on the vibrational mode. The calculations for $\gamma = 10^5$ in Fig. 3.27 present this accurately, see blue and cyan lines for $r = 0.01$ and $r = 0.02$, respectively. In any other case, the finite γ value influences this jump height. For example, the depicted black line represents the $\gamma = 3$ case with an increased but commensurate jump. With increasing voltage, the phonon mode is pumped, and the average occupation number increases. Both, the voltage and the occupation number increase the phonon pumping probability (see Eq. (3.11)). Therefore, one can observe a slope of decrease in the conductance. Quantitatively, the calculations depicted in Fig. 3.27 show that the slope is determined by r and the γ_{d} external damping rate. Based on the results, the role of phonon-phonon relaxation is easily understandable. In the limit of $\gamma \to \infty$, the excited phonons relax instantaneously, the slope is zero, and the vibrational mode cannot be pumped up to a desired E_{b}

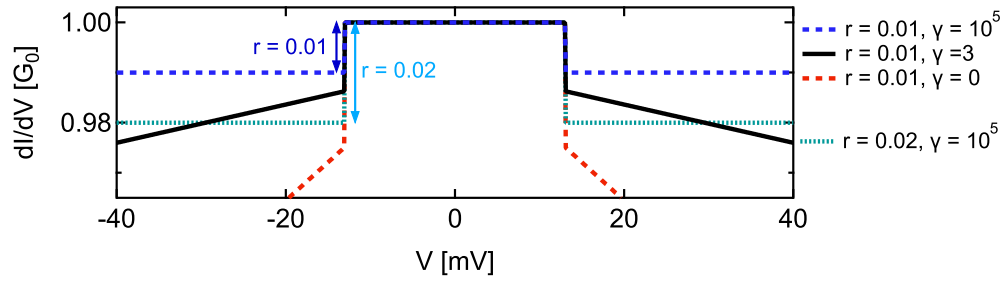

Figure 3.27: *Illustration of the simplified shape of the differential conductance as predicted by the single-level model. The jump-like decrease at $E = 13.1$ meV is due to the onset of phonon excitation. In the limit of no local phonon heating $\gamma \to \infty$, demonstrated by $\gamma = 10^5$ in the calculation (blue and cyan lines), the jump height is directly described by r. In contrast, at finite γ values, the jump height and slope of conductance decrease changes. The $\gamma = 3$ and $r = 0.01$ values (black line) are motivated by the model fitting on Au wire point-contact spectroscopy measurements [72, 76], depicted in Fig. 3.28.*

barrier energy. Finally, the single-level model can describe the voltage-dependent differential conductance, and in Ref. 72, it was demonstrated to be adequately fitting the experimentally obtained $\mathrm{d}I/\mathrm{d}V$ characteristics of single-atom [76] and single-molecule [77] junctions. Fig. 3.28 depicts the fit of the differential conductance in an atomic Au nanowire.

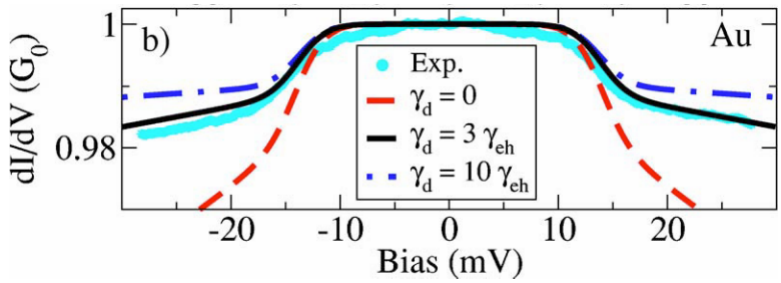

Figure 3.28: *Experimental result (light blue) of voltage-dependent differential conductance in single-atom Au nanowire fitted utilizing the single-level model with parameters $\gamma = 3$ (black line), $E = 13.8$ meV and $r = 0.009$. Measurement is from Ref. 76, while the theoretical fit and figure itself are presented in Ref. 72.*

Based on the above considerations, the γ external damping rate and the r electron-phonon interaction rate can be obtained from point-contact spectroscopy measurements. Such measurement was not performed on Ag, but the experimental results and the bias-dependent model fitting on Au nanowire presented in Fig. 3.28 provide a good estimate for the description in Ag point-contact, which yields the $\gamma = 3$ ratio and $r \sim 0.01$ rate used in the simulations.

Markov chain model and details about the simulation

The previous section summarized the basics of the vibrational pumping model, with a focus on expressing the phonon excitation and absorption probabilities based on the one-level model [72] (Eqs. (3.11)-(3.13)). In the following, I will detail the voltage-induced evolution of the vibrational energy states described as a random walk along the energy ladder. Fig. 3.29 illustrates a detailed picture of the phonon occupation ladder with the voltage- and occupation-dependent probabilities. Such

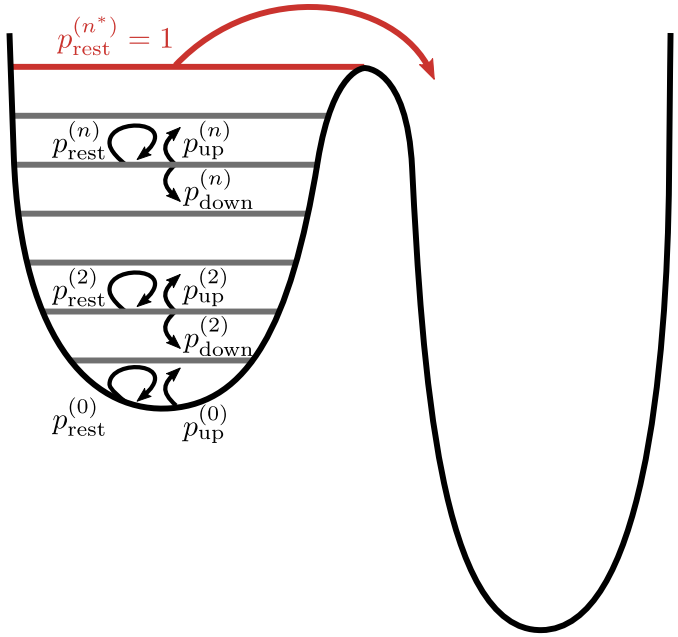

Figure 3.29: *The double-well potential illustrated together with the phonon occupation ladder which has to be climbed to trigger the switching. The voltage-dependent transition probabilities are considered at each n phonon occupation number. Published in Ref. P1.*

random walk of the consecutive transition events can be represented by a Markov chain model [78]. Fig. 3.30 depicts the mathematical diagram describing the problem with highlighted notation for a general n occupation number. In this notation, the final state at occupation number $n^* = E_b/E$ is the so-called absorbing state of the system where no transition out of this state is allowed, as in $p_{\text{rest}}^{(n^*)} = 1$. The

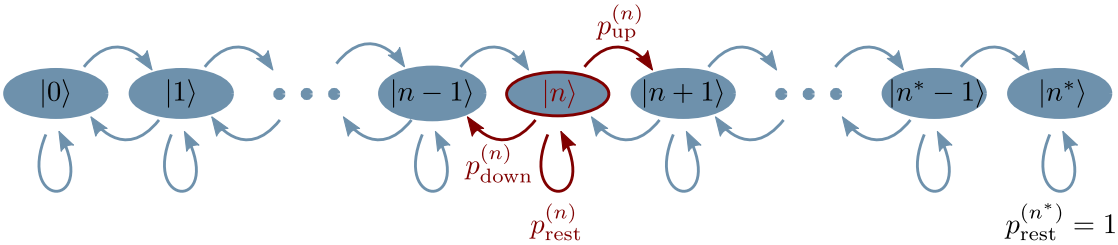

Figure 3.30: *Representation of the Markov chain of the phonon state occupancy with probabilities of moving up, down, and no event, respectively $p_{\text{up}}^{(n)}$, $p_{\text{down}}^{(n)}$ and $p_{\text{rest}}^{(n)}$ for a general n occupation number.*

bias-dependent stochastic matrix for this Markov chain is defined as

$$\mathbf{P} = \begin{bmatrix} p_{\text{rest}}^{(0)} & p_{\text{down}}^{(1)} & 0 & & & & & & \\ p_{\text{up}}^{(0)} & p_{\text{rest}}^{(1)} & p_{\text{down}}^{(2)} & & & & & & \\ & \ddots & & & & & & & \\ & & & p_{\text{rest}}^{(n-1)} & p_{\text{down}}^{(n)} & 0 & & & \\ & & & p_{\text{up}}^{(n-1)} & p_{\text{rest}}^{(n)} & p_{\text{down}}^{(n+1)} & & & \\ & & & 0 & p_{\text{up}}^{(n)} & p_{\text{rest}}^{(n+1)} & & & \\ & & & & & & \ddots & & \\ & & & & & & p_{\text{up}}^{(n^*-2)} & p_{\text{rest}}^{(n^*-1)} & 0 \\ & & & & & & 0 & p_{\text{up}}^{(n^*-1)} & 1 \end{bmatrix}$$

with $P_{j,i}$ transition probabilities from state $n = i$ to $n = j$. Note that the matrix is tridiagonal, as the occupation number can only change by 0 or 1. The elements are accordingly given by $P_{n,n} = p_{\text{rest}}^{(n)}$, $P_{n+1,n} = p_{\text{up}}^{(n)}$ and $P_{n-1,n} = p_{\text{down}}^{(n)}$.

A state vector $v_i(k)$ is defined containing the probability of the system being in the state $n = i$ at time $t = k\Delta t$ with the condition that the simulation always starts from the ground state $v_0(k = 0) = 1$ with no other states filled ($v_{i\neq 0}(k = 0) = 0$). Subsequently, the probability of state $n = j$ after k time steps is given by

$$v_j(k) = \sum_{i=1}^{n^*} P_{j,i} v_i(k-1). \tag{3.18}$$

The probability that in t time a switching occurs is translated to reaching n^* in exactly k time steps, which is given by

$$p_{\text{switch}}(k) = v_{n^*}(k) - v_{n^*}(k-1). \tag{3.19}$$

Although for a simulation at fixed bias, the mean first passage time is easily calculated from this point, the goal is to simulate the measurements obtained with a triangular voltage signal with characteristic sweep rates. In the simulations, a discretized voltage sweep $V = M\Delta V$ is defined where M is the number of voltage steps and $\Delta V = 0.1\,\text{mV}$ is the voltage resolution. For a signal with $\Delta V/\Delta T$ sweep rate, $\Delta T = N\Delta t$ is the length of each voltage step consisting of N time steps. Fig. 3.31 shows the simulated triangular signal at a sweep rate of 1 V/s. To speed up the simulation, instead of calculating the probability of reaching the barrier each $\Delta t = \Delta T/N$ time step, the cumulative effect of each time step in the voltage plateau can be obtained by

$$v_j^{(M)} = \sum_{i=1}^{n^*} \left(P^N\right)_{j,i} v_i^{(M-1)}. \tag{3.20}$$

The difference from the evolution of states described in Eq. (3.18) is that now the calculation is only evaluated at the end of the voltage steps based on the state

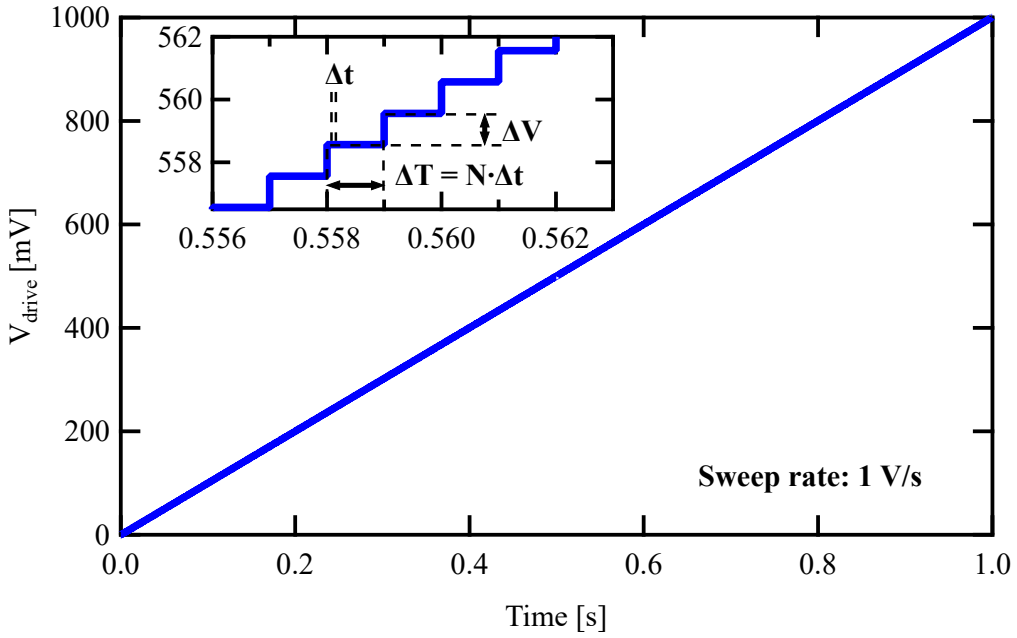

Figure 3.31: *The simulated triangular signal with a sweep rate of 1 V/s. The $V = M\Delta V$ voltage is defined in M steps with a $\Delta V = 0.1$ mV resolution. The length of each voltage plateau is $\Delta T = N\Delta t$, consisting of N subsequent Δt time steps. Published in Ref. P1.*

vector at the end of the voltage step $M-1$ and the N-th power of the probability matrix P. The simulation then yields the probability density of reaching the barrier at bias voltage $V = M\Delta V$

$$p_{\text{switch}}(V) = v_{n^*}^{(M)} - v_{n^*}^{(M-1)}. \tag{3.21}$$

The $p_{\text{switch}}(V)$ is calculated in a large range of V values, which results in a probability density function. Fig. 3.32 plots examples of the obtained probability density function for a few sweep rates and barrier heights. The simulation is run for several sweep rates and barrier heights, and the probability density function provides both, the threshold voltage's mean and standard deviation to compare with measurements. It is a general trend, that the probability density functions exhibit increasingly broadened distributions of the threshold voltages with increasing mean value.

Note that this vibrational pumping model applies fixed, physically motivated model parameters, and the E_{b} barrier energy is the only free parameter, which is rather directly related to the V_{thr} switching voltage. On the other hand, the energy landscape (Fig. 3.29) of the system is considered to be modified by the applied voltage, presumably yielding a decrease of E_{b} with increasing voltage. Furthermore, the energetically more stable atomic configurations should be interchanged at reversed voltage polarity. These processes are not modeled in the simulation. However, at low enough voltages, where the probability of reaching the barrier energy is negligible, the actual value of E_{b} is insignificant. Therefore, E_{b} can be considered as the characteristic barrier height in the voltage interval, where the switching has a reasonable probability, i.e., in the voltage region, where the

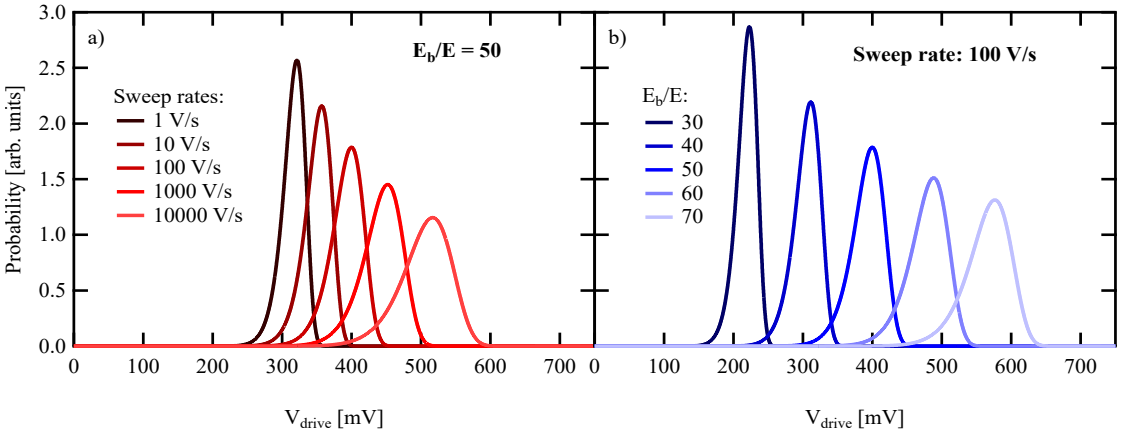

Figure 3.32: *The resulting probability density function of the simulated threshold voltage for different sweep rates (a) and for different barrier heights (b). Published in Ref. P1.*

experimentally measured V_{thr} values scatter.

Comparison with measurement

The simulation results based on the vibrational pumping model are compared to the experimental data in order to describe the sweep rate dependence of the threshold voltage and the cycle-to-cycle variation of the threshold voltage. Additionally, this analysis motivates and discusses the simulation parameters as physically relevant measures.

First, I compare the current-voltage characteristics of 20 measured (red) and simulated (black) curves in Fig. 3.33. The simulation is performed with E_{b} barrier

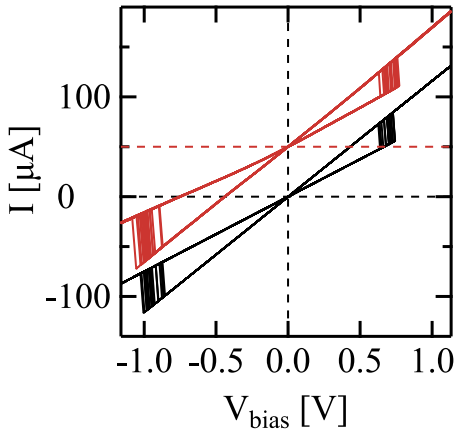

Figure 3.33: *The simulated (black) and the vertically shifted measured (red) current-voltage characteristics of 20 consecutive switchings. Published in Ref. P1.*

heights adjusted to reproduce the average experimental switching voltages. More on the connection between barrier height and switching threshold will be discussed in the next paragraph. The simulated HCS and LCS conductances and the sweep

rate are chosen to be identical to the measurements. This comparison gives a qualitatively agreeing cycle-to-cycle variation, and in the following, a further comparison is presented to investigate the quantitative agreement.

In Fig. 3.34(a), the sweep rate dependence of the threshold voltage of all pure atomic switching measurements are plotted that feature an initial conductance of $G = 1 \pm 0.15\ G_0$ (red dots). These experiments are fitted along the linear V_{thr} and logarithmic sweep rate. In the simulations, parameter M is the number of open channels that can be roughly estimated from the conductance by $M = \mathrm{round}(G/G_0)$; therefore, the simulations with parameter $M = 1$ corresponds to the single conductance channel case $G \sim 1\ G_0$. Note that based on the probabilities expressed in Eqs. (3.11)-(3.12), the parameters M and r both tune the outcome in the same way, therefore the $M \cdot r$ product is considered. The simulations executed for $M \cdot r = 0.01$ for various E_{b} energy barriers are depicted with colored dashed lines. The simulated threshold voltage trends over the sweep rate very well resemble the slopes of the experimental fits. In addition, by increasing the energy barrier height, the threshold voltage and the slope also increase. Accordingly, the measured typical threshold voltage and the slope yield an estimated phonon energy barrier when compared with the simulation.

An additional comparison to the simulation results is presented in panels (b) and (c), plotting the threshold dependence of the slope and the relative cycle-to-cycle standard deviation for measured and simulated data. The threshold voltage on the x-axis is at 100 V/s (solid gray line in panel (a)), and the exact value is interpolated from the voltage threshold versus sweep rate fits. The slopes are calculated from the linear-logarithmic fits between the whole range measured for the experimental data. Meanwhile, the slope of the simulated sweep rate dependence is defined between $50 - 500$ V/s, dashed gray lines in panel (a) indicate these limits, enclosing one order of magnitude change in the sweep rate. The relative cycle-to-cycle standard deviation in panel (c) is linearly interpolated at 100 V/s from the neighboring data points for both measured and simulated data.
The measured data is marked with circles colored based on the conductance range, although there is no apparent conductance dependence based on the color coding in either plot. The results of the simulation executed with the default parameters of $M = 1$, $r = 0.01$, and $E = 13.1$ meV are plotted with a solid black line, and dashed colored lines indicate the sensitivity of the model to these parameters, yellow for a three-fold increase of phonon energy quantum E and green for a hundred-fold increase of $M \cdot r$.

The sensitivity of the simulation to all model parameters within physically relevant limits is investigated in a complementary analysis in Fig. 3.35, consisting of the slope values, and the absolute and relative stochastic threshold value variations as a function of the average threshold values at 100 V/s sweep rate, in panel (a), (b), and (c), respectively. Before going into details about the comparison between the measured and simulated results, first, I will describe the limits for the $M \cdot r$, E, and γ parameters. Each of these parameters was detuned while all the others were left at their default values (indicated in the legend for the black curve panel (c)). Meanwhile, in this plot, all measured data is plotted with gray circles.
All the investigated pure atomic switching states were investigated in the range

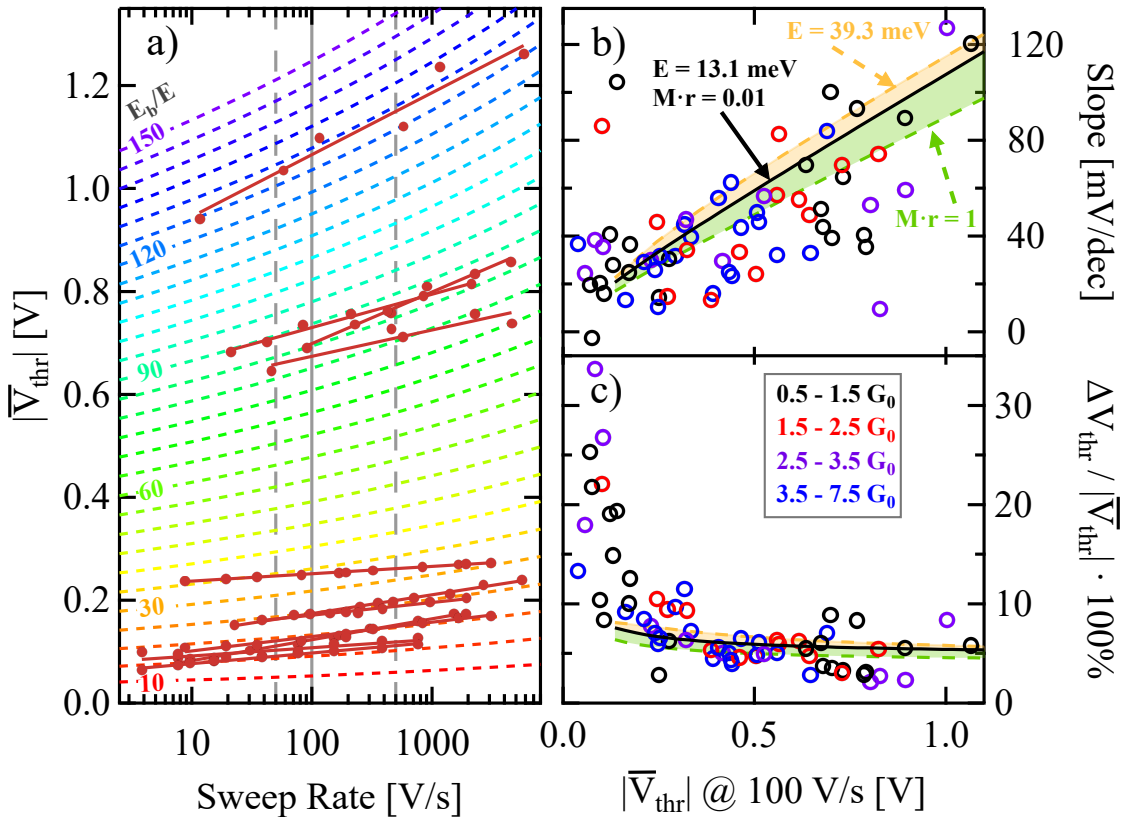

Figure 3.34: *(a) The simulated (colored dashed lines) and measured (red dots) sweep rate dependence of the threshold voltage with $M = 1$ corresponding to a conductance of $G \sim 1\ G_0$. (b-c) Quantitative comparison of the slope (from fit on the linear-logarithmic scale) and relative cycle-to-cycle standard deviation. The threshold voltage is evaluated at 100 V/s (solid gray lines in panel (a)). Measured data (circles) is color-coded based on the initial conductance indicated in the legend. The simulated slope is evaluated between $50 - 500$ V/s (dashed gray lines in panel (a)). Color of the simulated data illustrates the parameters used to run the simulation, black lines present the default set of $M \cdot r = 0.01$ and $E = 13.1$ meV, while yellow and green lines indicate results either with a three-fold increase of phonon energy quantum E or for a hundred-fold increase of $M \cdot r$, respectively. Published in Ref. P1.*

of $1 - 10\ G_0$, therefore, the number of open channels is considered in the range $1 \leq M < 10$. The $r \approx 0.01$ interaction rate was obtained from point-contact spectroscopy measurements, see Eq. (3.17) and Fig. 3.28. Based on the step heights in the typical point-contact spectra of atomic junctions, $0.001 < r < 0.1$ range is expected to be a broad estimate for r. Based on these considerations with the additional possibility for even larger diameter junctions, the simulations were performed at detuned $M \cdot r = 0.001$ and $M \cdot r = 10$ limits, as demonstrated by the dark and light green dashed lines in Fig. 3.35.
The phonon energy quantum is a rather well-defined quantity in atomic junctions

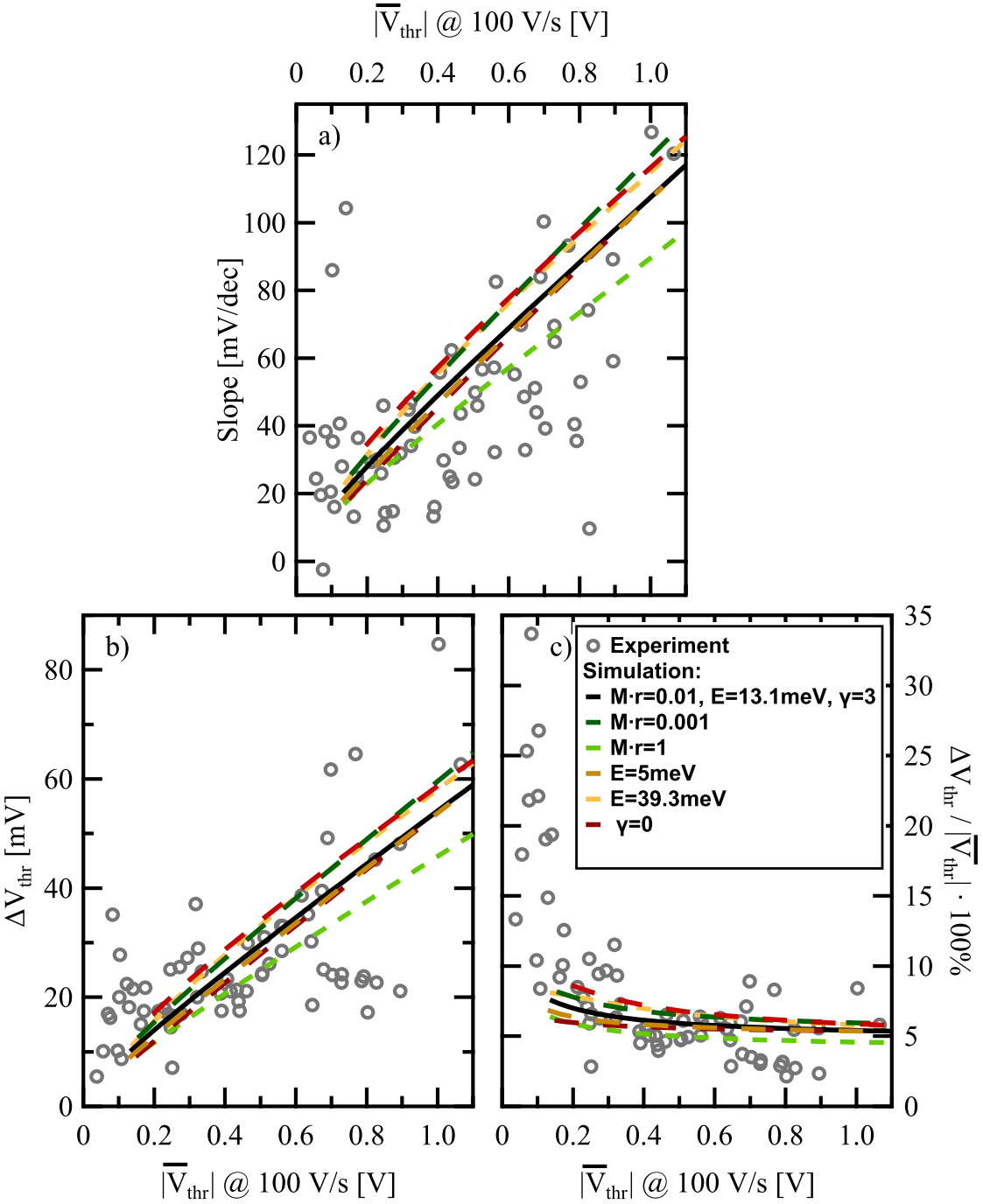

Figure 3.35: *Analysis of the sensitivity of the simulation to all model parameters (colored curves) compared to measured data (gray circles). Slope values (a), and the absolute (b) and relative (c) stochastic threshold value variations as a function of the average threshold values at 100 V/s sweep rate. Each parameter - $M \cdot r$ (dark and light green), E (brown and yellow), and γ (dark and light red) - were detuned between physically reasonable limits while others were left at the default values ($M \cdot r = 0.01$, $E = 13.1$ meV, and $\gamma = 3$). Published in Ref. P1.*

[60], i.e., threefold-detuned values of $E = 5$ and $E = 39.3\,\mathrm{meV}$ (brown and yellow dashed lines) are already considered as broad limiting cases.
Finally, the $\gamma = 3$ normalized external damping rate was also based on the point-contact spectroscopy measurements. $\gamma = 0$ and $\gamma = 10$ (dark and light red dashed lines) are considered as reasonable limits. The lower value corresponds to negligible external damping of the vibration mode, characteristic for a molecular junction [72, 77]. On the other hand, $\gamma = 10$ represents a significantly stronger damping which seems to be a practical upper limit according to the experiments and theoretical calculations [72].

The slope plotted in Fig. 3.34(b) and Fig. 3.35(a) shows that the measured and simulated values cover the same slope range exhibiting a very similar threshold voltage dependence. The range of the simulated slope and the increasing trend, indicating roughly 10% relative variation of the threshold voltage over a decade in sweep rate, are in good agreement with the measured data.
The measured relative cycle-to-cycle standard deviation in Fig. 3.34(c) and Fig. 3.35(c) at around a constant value of ∼5% are well described by the simulation. For decreased threshold voltages, the measured data exhibits a rapidly increasing relative deviation, and although the simulation also anticipates an increase, this does not track the measured trend. The simulation is expected to be less reliable for small voltages since this voltage range would correspond to a small energy barrier. Based on the results, an energy barrier of $E_\mathrm{b}/E \geq 10 - 20$ already works; therefore, the simulation is only plotted for threshold voltages above this level. Note, that panels Fig. 3.35(b) and (c) compare the absolute and relative threshold voltage variations, implying that the divergence of the experimental points at low threshold voltages in panel (c) is related to the fact that the normalization to the low V_thr magnifies a small excess value of ΔV_thr. Furthermore, the repeated cycling may also introduce slight variations in the two atomic arrangements, even if the conductances of the two states seem to be similar in the subsequent cycles. The latter issue may introduce an additional cycle-to-cycle variance of the threshold voltage, which may also explain the deviation from the model curves especially in the low threshold region, where the normalization to the low V_thr magnifies a small excess value of ΔV_thr.

Concluding the comparison, it is clear, that the scattering of the experimental data is considerably larger than the variation of the simulation results within the above broadly estimated limiting cases. This implies that the experimental points significantly deviating from the default-valued simulations are not related to fundamentally different model parameters, rather to the fact that the model does not grab many details of the actual switching process, in particular the obvious voltage-dependent deformation of the potential landscape as the switching is approached, as well as current-induced or non-conservative forces acting on the switching atom [55, 79]. Furthermore, the role of these aspects is expected to be different for each individual junction arrangement, which might explain the broad variance of the experimental data points around the general tendency predicted by the simplified model. In consequence, the presented model can only describe the most typical trends, but not the broad device-to-device variations.
Still, the comparison confirms the successful application of the vibrational pumping

model, as it provides a quantitative description describing the weak frequency dependence of the switching threshold voltage, as well as its stochastic cycle-to-cycle variation.

3.3.3 Conclusions

The earlier works in the research group reported on atomic-scale switching in Ag_2S-based memristive systems with fundamentally different features from ECM-type switching. These results motivated the deeper study of pure atomic switching in Ag, and the comparison to the fundamentally different characteristics of ECM-type switching. My analysis suggests the possible appearance of the atomic switching phenomenon in a wider range of atomic-sized ECM-type resistive switching systems, highlighting the need for the proper characterization and understanding of the atomic processes.

I performed pure atomic switching measurements on high-purity Ag MCBJ samples at low temperatures and gave an extensive quantitative comparison to ECM-type memristive switching in AgI-based STM-BJ samples (measurements of Botond Sánta and Dániel Molnár). This quantitative analysis showed the fundamentally different characteristics of pure atomic switching compared to ECM-type switching. Pure atomic switching exhibits an abrupt jump-like switching at stochastic threshold voltages between discrete geometric arrangements, with large cycle-to-cycle and device-to-device variation and comparatively weak sweep rate dependence of the threshold voltage.

Based on the vibrational pumping model of Paulsson *et al.* [72], we proposed a theoretical approach to describe the sweep rate dependence of the average and the standard deviation of the threshold voltage. The model described the voltage-dependent evolution of the phonon occupational number by simulating the random walk along the energy ladder of the vibrational mode. In this picture, the switching event is triggered by reaching a phonon energy barrier. The quantitative comparison of the simulation to measurements was consistent with the experimental observations, i.e., the weak frequency dependence of the switching threshold voltage, as well as its stochastic cycle-to-cycle variation.

3.4 Development and characterization of Ag nanofabricated break-junction samples

As already foreshadowed in Section 3.2.2, nanofabricated MCBJ samples provide superior stability, which could not only enable room-temperature observation of pure atomic switching in Ag but also prolonged quantum transport measurements to stabilize single-atom [41, 50, 80, 81] and single-molecule [82–85] structures of other oxygen-sensitive metals. However, high reactive metal surfaces present a challenge regarding the usual lithographic procedure, as the suspension step executed by oxygen plasma etching also destroys the sensitive metallic thin film. During my work, I participated in the development of an alternative non-oxidizing sample preparation method to overcome this obstacle, and I characterized the resulting nanofabricated Ag MCBJ samples. The results of this work are summarized in Ref. P2 and in Thesis Statement II.

The original non-oxidizing nanofabricated fabrication process was developed by Ágnes Gubicza, Jan Overbeck, and Péter Makk at the University of Basel. I learned and reconstructed the fabrication steps during a research trip in Switzerland at the laboratory of Prof. Michel Calame at Empa, Swiss Federal Laboratories for Materials Science and Technology and at ETH Zürich, in collaboration with Miklós Csontos, where we also implemented some improvements. The thermal evaporation was done by Martina Lingg at Empa. Miklós Csontos was in charge of the electron beam lithography, and I was responsible for the remaining step. Later, I produced additional samples for characterization measurements at the Institute of Technical Physics and Materials Science in Budapest. Here, György Molnár carried out the thermal evaporation, and László Pósa performed the electron beam lithography.

3.4.1 Development of Ag nanofabricated sample fabrication

First, I introduce the steps of sample fabrication that are summarized in Table 3.1 and illustrated in Fig. 3.36.

The first step of the fabrication process is cleaning the 0.3 mm thick stainless steel substrate before coating it with polyimide. This step consists of repeated spin-coating and baking until the thickness of 4 µm is reached, which serves as an insulator and helps to smooth the steel plate's otherwise rough surface. The next step is the spin-coating and baking of the sacrificial layer LOR^{TM} 3A in the thickness of 300 nm, which is essential to omit oxygen plasma etching for the suspension in later steps. On top of that, PMMA electron-beam resist is spin-coated and baked in the thickness of 430 nm. During electron beam lithography, both the sacrificial and resist layers are exposed to the electron beam to create the junction and electrode structure (panel (a)). This is followed by the development of the resist layer (panel (b)) to construct the mask for the metal evaporation. Note that only the resist layer is developed, the sacrificial layer is only removed below the constriction in a later step. Thermal evaporation is recommended for metal deposition (panel (c)) as scattered electrons during the commonly used method of electron beam evaporation could inadvertently expose the sacrificial layer resulting in the removal of additional regions, thus mechanically destabilizing

Step	Procedure/Parameters	Functionality
Cleaning of stainless steel plate	• Cleaning with acetone, isopropanol and distilled water	Clean substrate
Polyimide coating (HD Microsystems PI2611)	• Coating at 600 min^{-1} for 3 s, then 4000 min^{-1} for 30 s • Baking at 300 °C for 1 h • Repeating coating and baking 3-4 times	Smooth surface, final thickness around 4 µm
Spin-coating LOR^{TM} 3A	• Coating at 4000 min^{-1} for 45 s • Baking at 200 °C for 15 min	Sacrificial layer, final thickness around 300 nm
Spin-coating PMMA (950K AR-P 671.04)	• Coating at 2000 min^{-1} for 40 s • Baking at 180 °C for 5 min	Resist layer, final thickness around 430 nm
Electron beam lithography /Fig. 3.36(a)/	• Exposing structure to 20 kV • Line dose (junction): 1000 µC/cm^2 • Area dose: 190–240 µC/cm^2	Writing structure
PMMA development /Fig. 3.36(b)/	• Immersing in o-xylene for 1 min 50 s • Rinsing with hexane for 30 s, drying with N_2 flow • Dehydration on hotplate at 100 °C for 1 min	Removal of exposed resist
Thermal evaporation of Ag /Fig. 3.36(c)/	• Evaporation rate around 20 Å s^{-1} • Desired thickness at 70 nm	Thin-film deposition
PMMA lift-off /Fig. 3.36(d)/	• Immersing in 70 °C warm o-xylene for $>$ 1 h • Rinsing with hexane for 30 s, drying with N_2 flow	Removal of non-exposed resist
Spin-coating PMMA (950K AR-P 671.02)	• Coating at 6000 min^{-1} for 40 s • Baking at 180 °C for 5 min	Protection mask, final thickness around 70 nm
Electron beam lithography /Fig. 3.36(e)/	• Exposing structure to 20 kV • Area dose: 1200 µC/cm^2	Creating free-standing bridge
PMMA development /Fig. 3.36(f)/	• Immersing in o-xylene for 1 min 50 s • Rinsing with hexane for 30 s	Removal of exposed resist
LOR development /Fig. 3.36(g)/	• Immersing in 1-methoxy-2-propanol for 2 min • Rinsing with hexane, drying with N_2 flow	Removal of exposed sacrificial layer
PMMA removal /Fig. 3.36(h)/	• Immersing in 70 °C warm o-xylene for 5 min • Rinsing with hexane, drying with N_2 flow	Removal of remaining resist

Table 3.1: *Overlook of the non-oxidizing nanofabricated MCBJ sample preparation steps with parameters.*

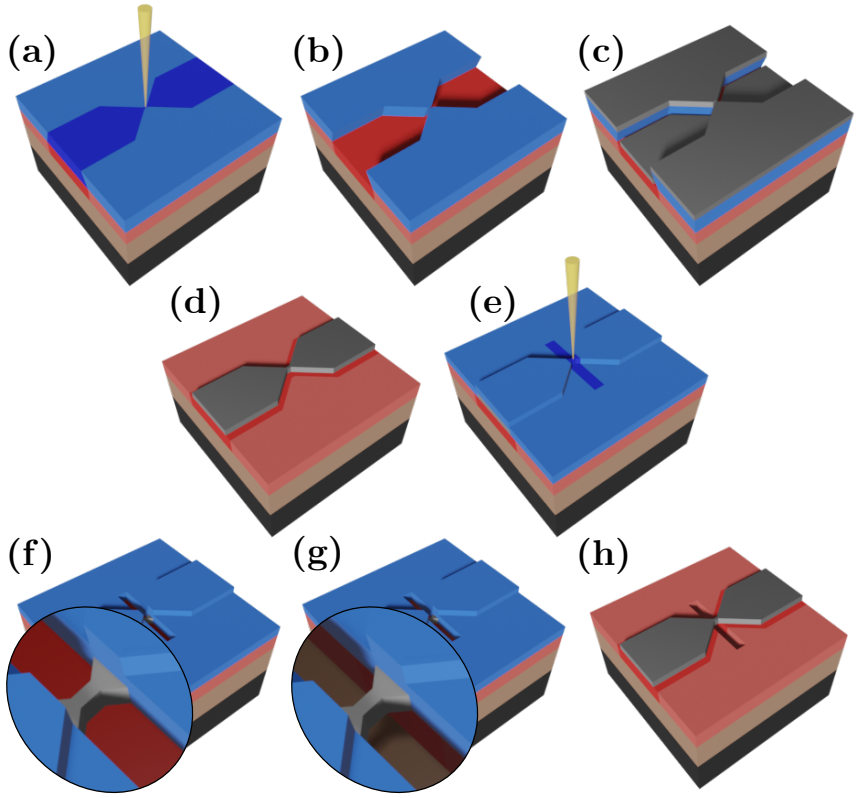

Figure 3.36: *Schematic depiction of the sample fabrication process. The initial structure of the sample consists of the steel substrate (black), the polyimide insulating layer (light brown), the LOR™ sacrificial layer (red), and the PMMA resist layer (blue). The saturated shades indicate the regions exposed to electron beam lithography. (a) Electron beam lithography of the structure. (b) Development of the exposed resist. (c) Thin-film deposition of Ag. (d) Lift-off of the non-exposed resist. (e) Electron beam lithography preparing the free-standing bridge. (f) Development of the exposed resist. (g) Development of the exposed sacrificial layer. (h) Lift-off of the remaining resist. The fabrication steps are detailed in the text. Published in Ref. P2.*

the junction suspension. After lift-off (panel (d)), a thin protective PMMA resist layer is spin-coated and baked with the thickness of 70 nm, and the second electron beam lithography step (panel (e)) is executed for creating the suspension. The protective resist layer ensures that even when additional regions in the sacrificial layer are exposed to electrons (either during evaporation or lithography), only the necessary region below the constriction will be removed. The suspension is formed by the subsequent development of the resist (panel (f)) and sacrificial (panel (g)) layers. Finally, the protection layer is removed (panel (h)), and the sample is ready for measurements. Based on the statistics of the test samples created in Zürich, the constriction is typically 100 ± 20 nm wide and 140 ± 50 nm long, while the suspended region is 880 ± 200 nm long.

Fig. 3.37(a) depicts the optical microscope image of one of the first test samples,

where the evaporated material was Au due to technical reasons. Each sample has two parallel junctions with one shared lead (left side in panel (a)). The scanning electron microscope picture of a typical Ag sample is shown in panel (b) with the visible trench under the junction area. The usual contacting of nanofabricated MCBJ samples is done with silver conductive paste; however, the sacrificial LOR layer is incompatible with this method. Therefore, the leads are contacted with a clamp setup as schematically depicted in panel (c). Small and soft pieces of indium are between the sample electrodes and the copper pins to avoid damage. The clamps are fixed in their position by small screws at the ends, and finally, thin copper wires are soldered to the pins.

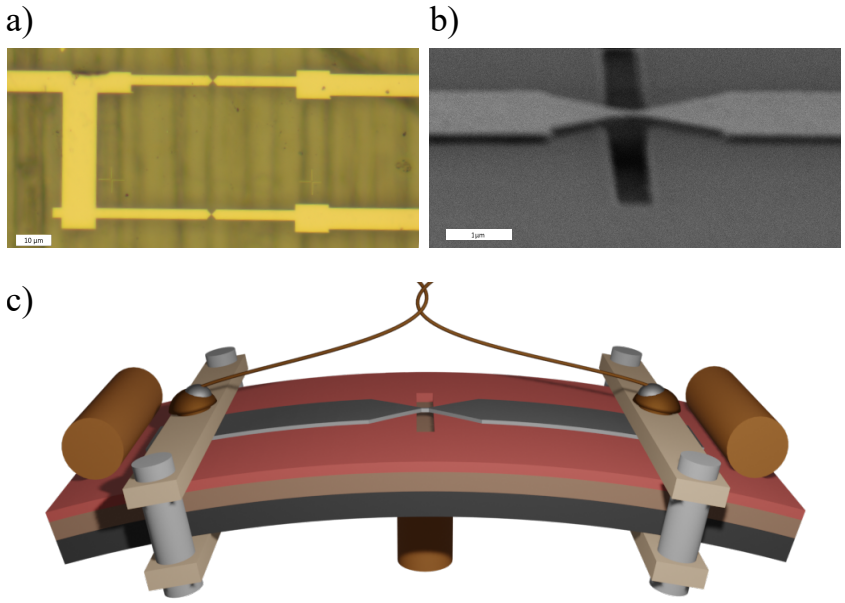

Figure 3.37: *(a) Optical microscope image of Au test sample. (b) Scanning electron microscope image of the suspended junction area. (c) Schematic MCBJ setup and sample contacting with clamp setup. Published in Ref. P2.*

The nanofabricated MCBJ samples are expected to exhibit higher mechanical stability and a lower displacement ratio. On the other hand, the nanofabricated structure is more vulnerable to ESD. I conducted the measurements in the room-temperature sample holder depicted in Fig. 3.38(a). To ensure the purity of the sample, the sample holder is vacuum-pumped to under 10^{-3} mbar pressure. I also used a switch box serving as an extra ESD protection, designed with the option to ground the sample connectors with a serial 1 MΩ resistance. The sample is mounted carefully between the pushing rod and the counter-supports shown in Fig. 3.38(b). One significant difference in the fabrication and tuning of the atomic-sized junction is the irrelevance of the piezo positioner. Since the displacement ratio decreases to a degree where the range of motion of the piezo positioner is no longer effective, the conductance tuning of the junction is executed only with the coarse displacement induced by the motor. While it was an important goal to characterize the new samples with conductance histograms constructed from breaking traces, the breaking of nanofabricated MCBJ samples cannot be executed by fine-tuning

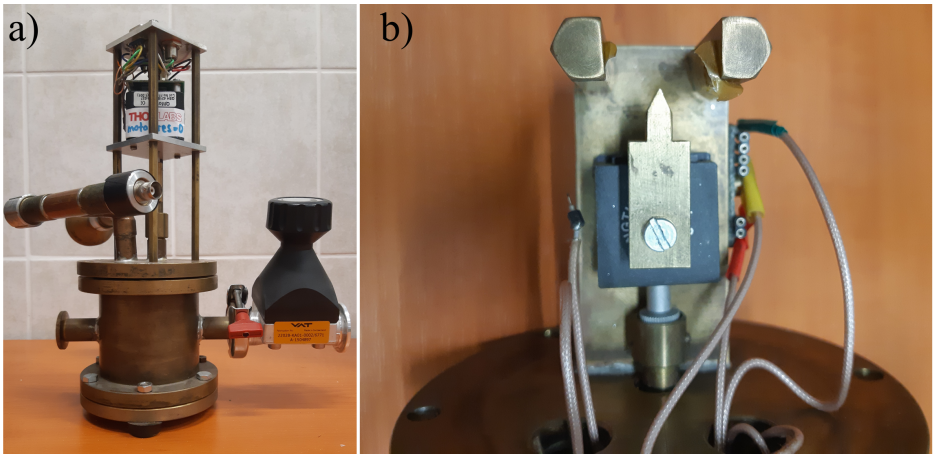

Figure 3.38: *(a) Photo of the vacuum chamber setup. (b) The close-up of the MCBJ sample holder with the pushing rod mounted on the translation stage which is driven by the motor. Note that there is no need for piezo positioning due to the decreased displacement ratio.*

with the piezo positioner. Therefore, I wrote a new LabVIEW program recording conductance histograms with feedback-controlled motor positioning. On the other hand, the stability and $I(V)$ curves were still measured in the original program by András Magyarkuti [65]. The measurement setup is modified from the one in Fig. 3.13 by leaving out the piezo system and including a voltage divider on the output of the data acquisition card. Since the analog output of the data acquisition card has a finite resolution and is also subject to noise, it is advisable to use a voltage divider to generate the low voltage level to ensure a longer lifetime of the nanofabricated samples. The typical serial resistance value is $R_s = 1$ kΩ.

3.4.2 Characterization measurements on Ag nanofabricated break-junctions

The main goal of the characterization experiments was to deliver proof-of-principle measurements of the samples fabricated with the new design. Some representative breaking traces are depicted in Fig. 3.39, the conductance as a function of the electrode displacement measured with a low drive voltage of 10 mV. The traces exhibit the expected staircase structure with plateaus indicative of the Ag nanowire, most prominently the plateau at 1 G_0 corresponds to the conductance of the Ag single-atom junction [59, 86, 87].

It is important to correctly interpret the scaling of the displacement, as this question needs a detailed discussion. The first step is the calibration of the Δz motor displacement based on the parameters of the stepper motor. Then, there are multiple approaches to estimate the Δx displacement from the measured breaking or closing traces [88] and conclude the displacement ratio $r = \Delta x/\Delta z$. One method is the calibration based on the chain length of single atoms before breaking, that is, the examination of the 1 G_0 plateau length. The principal idea is to employ that an atomic chain can be formed when stretching the monoatomic contact,

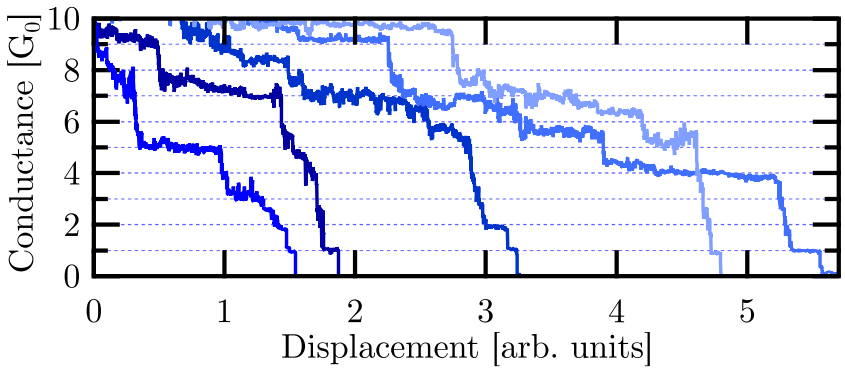

Figure 3.39: *Representative breaking traces, conductance measured as a function of electrode separation featuring conductance quantization with the distinct* 1 G_0 *conductance characteristic for Ag single-atom junction. Published in Ref. P2.*

yielding multiple equidistant peaks in the plateau length histogram consisting of the lengths of the measured 1 G_0 plateaus. However, the atomic chain formation is not characteristic for Ag, and accordingly, I did not observe the expected structure in the plateau length histogram. Instead, measurements on Au in low-temperature measurements could provide such information [39, 89].
Another way of calibration is exploiting the exponential dependence of the current in the tunneling regime. The tunneling conductance formula derived for small voltages $e \cdot V < \phi$ from the exponential dependence of the current in a vacuum gap [88] looks like the following:

$$G \propto \exp\left(-\sqrt{8 \cdot m \cdot \phi} \cdot x/\hbar\right), \tag{3.22}$$

where m is the mass of the electron, ϕ is the height of the tunnel barrier estimated by the electrode work function, and x is the electrode separation. The Δx variation of the electrode distance corresponding to a change of conductance between G_1 and G_2 values is then calculated as

$$|\Delta x| = \frac{|\ln(G_2) - \ln(G_1)|}{\sqrt{8 \cdot m \cdot \phi}/\hbar}. \tag{3.23}$$

The tunneling regime is more pronounced in the closing traces because, during the closing of the junction, smaller gaps can be created between the electrodes, and the tunneling regime is observed in a wider range. This is due to the fact that immediately after the rupture of the wire, the relaxation of atoms on the electrodes too quickly increase the gap to observe the tunneling regime. Fig. 3.40(a) shows a few examples of closing traces on a logarithmic scale, and panel Fig. 3.40(b) depicts the logarithmic two-dimensional histogram and average curve (black) of the included closing traces. The two-dimensional histogram is constructed by first aligning all traces at a certain conductance, which will serve as the zero displacement position, then defining bins along the logarithmic conductance and the displacement axis, where each bin is colored proportional to the included number of data points. Finally, although there is a large variation of traces, the calculated average trace exhibits

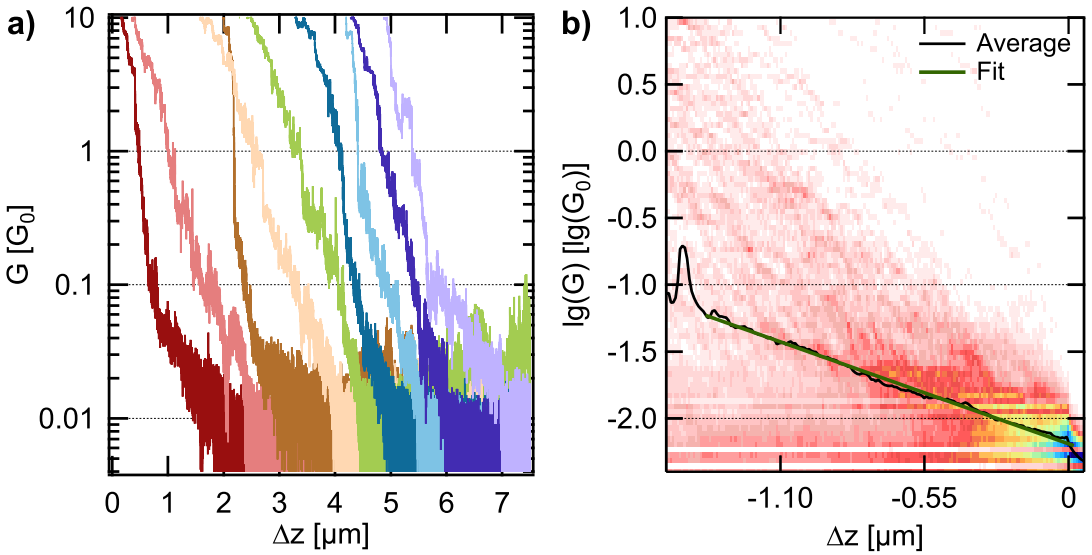

Figure 3.40: *Investigation of the tunneling regime of closing curves for calibration purposes. Typical individual traces (a) and two-dimensional histogram with average trace (b). In panel (b), the black curve is the average closing trace, which is fitted with a linear trend on the logarithmic-linear scale, see green curve.*

the expected linear relation between the logarithm of the conductance and the Δz displacement. The uncertainty of this calibration method comes from the difficulty of estimating the correct work function. Nonetheless, a rough range estimation of the displacement ratio can be calculated by considering both the vacuum work function of Ag $\phi = 4.26$ eV [90] and the estimated contaminated work function of $\phi = 1.1$ eV based on the reduced values reported for Au MCBJs due to the effect of water film formation and oxygen uptake [91, 92]. The resulting displacement ratio calculated from the tunneling fit (green), covering the uncertainty of the work function, is in the range of $\Delta x/\Delta z = (0.76 - 1.5) \cdot 10^{-4}$.

Nevertheless, some additional effects must be considered when interpreting the calibration. First, relevant research of Vrouwe *et al.* [92] raises attention to the changes in the displacement ratio of nanofabricated MCBJ samples because a soft layer, such as the polyimide and LOR layer, also sustains an elastic deformation during the bending of the sample. This also results in the significant difference between breaking and closing traces. Immediately after breaking the junction, the connection between the two sides snaps, and the soft layers endure the additional relaxation resulting in an increased junction separation. In addition, the nonlinear forces present in the atomic wire during the breaking induce a nonlinear strain in the soft layer, thus resulting in a possibly nonlinear scaling. In the end, the calculated displacement ratio is a rough estimate correctly describing the order of magnitude and is comparable with other values reported in the literature calibrated in the tunneling regime.

One can construct the conductance histogram based on many breaking traces

by counting the data points in each conductance bin for every breaking trace. The resulting conductance histogram exhibits peaks at conductances of stable junction geometries. The wider the peak, the greater the conductance variation of the given junction geometry. The conductance histogram of 266 independent breaking traces between the tunneling regime and 5 G_0 is depicted in Fig. 3.41(a) with the unmistakable appearance of the sharp single-atom peak at 1 G_0 and the broader double-atom peak around 2 G_0 [39] (see Fig. 3.3) confirming the absence of oxygen contamination [59]. As an interesting side note, the nanofabricated MCBJ

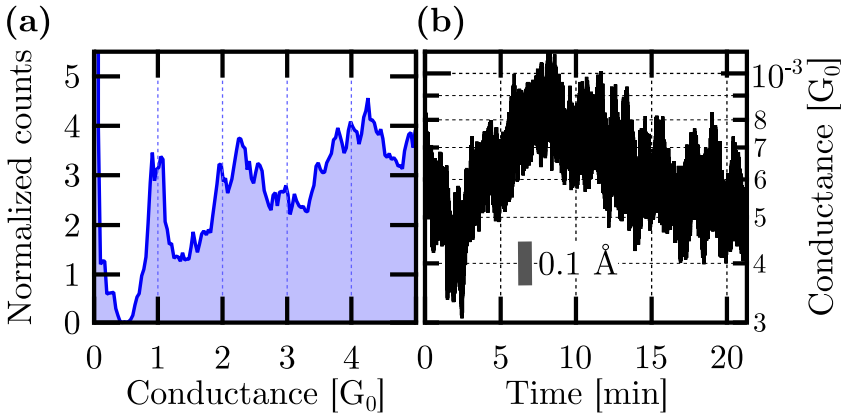

Figure 3.41: *(a) Conductance histogram of 266 independent breaking traces exhibiting a sharp 1 G_0 peak and a broader peak around 2 G_0 distinctive for Ag. (b) Over 20 minutes long stability measurement in the tunneling regime with a vertical bar indicating a 0.1 Å electrode displacement variation calculated from the vacuum work function of Ag. Published in Ref. P2.*

samples typically survive a few hundred, maybe a few thousand breakings, while notched-wire samples usually last a few ten thousand. Furthermore, due to the low displacement ratio, breaking the nanofabricated samples takes longer which is also a limitation.

For prolonged quantum transport measurements, the long-term stability of the junction is a crucial requirement that can be tested most convincingly in the mechanically most sensitive tunneling regime. Fig. 3.42(a)-(c) presents three over 20 minute long stability measurements measured with a low drive voltage of 10 mV, including the published measurement of Fig. 3.41(b) in panel Fig. 3.42(a). Such measurements were recorded by monitoring the conductance and manually stopping the motor rotation either during the closing (panels (a)-(b)) or the breaking (panel(c)) of the junction. The aim is to obtain the standard deviation (RMS) and peak-to-peak variation electrode separation from the stability measurements, using the formula of the electrode distance variation defined in Eq. (3.23). Due to the exponential dependence, it is evident that the variation of distance is derived from the natural logarithm of the conductances, so it is misleading to rely on the variation of conductance on the linear scale. Fig. 3.42(d) shows the conductance histogram of all three measurements on the natural logarithmic scale with two horizontal bars indicating a displacement variation of 1 Å = 100 pm calculated

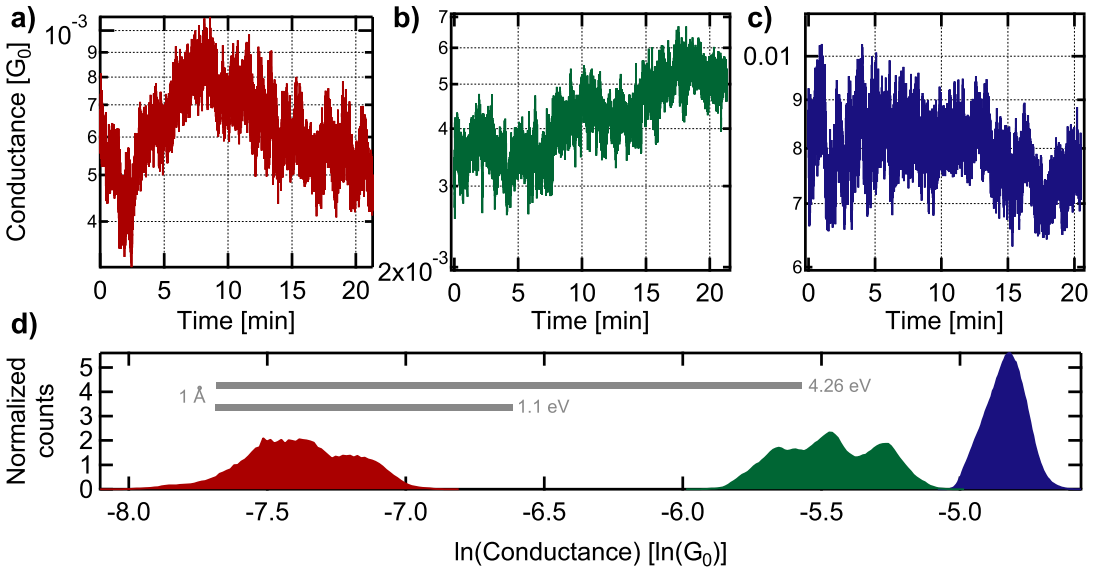

Figure 3.42: *(a-c) Stability measurements obtained at different tunneling conductances. (d) Normalized conductance histograms of the natural logarithm of conductance from the matching colored measurements in panels (a-c). The horizontal bar corresponds to* 1 Å *electrode displacement variation calculated from the vacuum and estimated contaminated work function, assigned values indicated aside.*

with the vacuum 4.26 eV and an estimated contaminated 1.1 eV work function. Table 3.2 summarizes the Δx calculation results derived from the RMS and the peak-to-peak variation of the conductance, again with both work function values. It is to be noted that even though the measurement of panel (c) (blue) exhibits the best stability, i.e., the smallest variation of electrode separation, the sample could not be closed again after this was recorded. Therefore, we decided to publish another more typical and creditable measurement. Furthermore, before judging the mechanical stability described by Δx, one should also consider that the calculation above attributes changes in the conductance exclusively to the mechanical noise of the sample. However, electrical noise and fluctuation in the work function of an ambient environment, including thermal drifting, could also play a significant role. Overall, the results prove the superior stability of the fabricated samples considering the fact that the calculated displacement variation is smaller than the 160 pm radius of an Ag atom [93], making it suitable for atomic-scale applications. Finally, I present the room-temperature pure atomic switchings which serve as a proof-of-principle for high-stability application possibilities of the fabricated sample design. Fig. 3.43 shows the reversible bistable pure atomic switching measured on one of the nanofabricated samples. The switching is observed between 2.34 G_0 and 1.66 G_0, which is speculated to be attributed to a monomer and a double-atom configuration [90], as illustrated in the insets.

Measurement	ϕ [eV]	$\Delta \ln(G_{\text{rms}})$ $[\ln(G_0)]$	Δx_{rms} [pm]	$\Delta \ln(G_{\text{pp}})$ $[\ln(G_0)]$	Δx_{pp} [pm]
Fig. 3.42(a)	4.26	0.19	9.0	1.31	61.8
	1.1		17.7		121.6
Fig. 3.42(b)	4.26	0.17	8.2	1.0	47.9
	1.1		16.2		94.2
Fig. 3.42(c)	4.26	0.07	3.4	0.52	24.7
	1.1		6.6		48.6

Table 3.2: *Δx_{rms} standard variation and Δx_{pp} peak-to-peak variations of electrode displacement based on the stability measurements presented in Fig. 3.42 for both vacuum $\phi = 4.26$ eV and estimated contaminated $\phi = 1.1$ eV work function, calculated by the Eq. (3.23).*

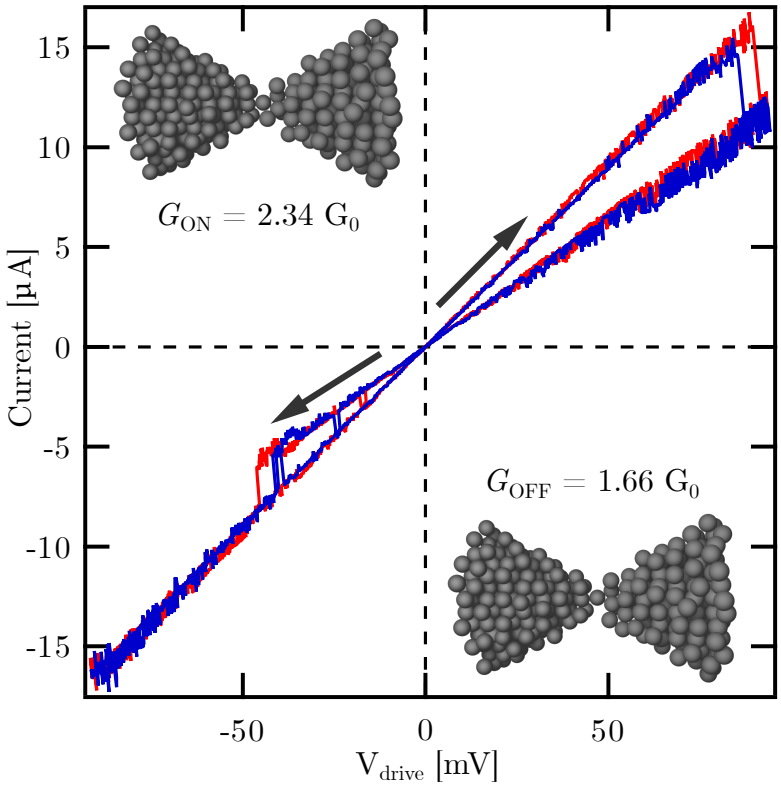

Figure 3.43: *Two reversible room-temperature pure atomic switching curves (red, blue) measured on one of the nanofabricated samples speculated to switch between a monomer and a double-atom configuration displayed in the insets. The arrows indicate the direction of the switching (set transition at negative voltage). Published in Ref. P2.*

3.4.3 Conclusions

The MCBJ technique provides a versatile tool for quantum transport measurements due to its high purity and stability. The nanofabricated MCBJ design offers superior stability and enables complex nanocircuit designs. However, the material of interest in my research with regard to pure atomic switching, Ag, has higher reactivity

that prevents its nanofabrication with the usual lithographic procedures, as the suspension step is executed by oxygen plasma. I demonstrated an alternative sample fabrication method realizing nanofabricated MCBJs of oxygen-sensitive metals. The proposed technique eliminates the reactive ion etching step by utilizing electron beam lithography on an additional sacrificial layer to achieve the suspended constriction. I performed test measurements on such Ag nanofabricated samples, yielding a characteristic conductance histogram for Ag and exhibiting excellent stability. As a proof-of-principle application, I published room-temperature pure atomic switching on Ag for the first time. These results successfully demonstrate the merits of nanofabricated Ag MCBJs as a versatile platform for studying quantum mechanical conductance phenomena.

Chapter 4

$1/f$-type noise characterization of resistive switching devices

Noise spectroscopy measurements are a versatile tool for understanding the physics involved in transport phenomena. While Johnson-Nyquist and shot noise are quite well understood, there are still uncertainties about the origin of $1/f$-type noise in various physical systems [94, 95]. Although the $1/f^{\gamma}$ frequency dependence of the noise spectral density is quite general and almost omnipresent, the broad range of exponents clearly indicates that diverse physical processes may be responsible for the resistance fluctuations. To understand $1/f$-type noise, the transport properties of the investigated physical system must first be considered. In this chapter, I present the overview of $1/f$-type noise research of resistive switching with a special focus on transition-metal-based valence change memories. Next, I summarize the results of Thesis Statement III about the steady-state noise spectroscopy, the voltage-dependent noise measurements describing switching dynamics, and the elaborate subthreshold cycling experiments to investigate noise tuning possibilities. These results are to be published in Ref. P3.

4.1 Noise basics

An essential part of resistive switching research is the electrical characterization of the devices. In my work, I strongly relied on noise spectroscopy to gain information about the investigated systems. In everyday life, noise is regarded as a disturbing effect accompanying any measured signal. However, the words of Rolf Landauer, "The noise is the signal" [96] remind us that noise spectroscopy is a valuable resource of information on the investigated system, which is not accessible via the study of the mean conduction properties. I will start this chapter by giving a short summary of noise basics.

4.1.1 Definition and measurement of noise

Experimentally, the noise of a signal is given by measuring the stochastic deviations from the mean value. For a current noise, an $I(t)$ current signal is decomposed as $I(t) = \langle I(t) \rangle_t + \Delta I(t)$, where the former term is the mean current, while the latter is

the temporal fluctuation around the mean value. The $S_I(f_0)$ noise spectral density is then calculated from the mean squared deviation of $\Delta I(t)$ measured within a narrow, Δf wide frequency band around the f_0 central frequency, $\langle \Delta I(t|f_0, \Delta f))^2 \rangle$. The noise is a broad-band signal containing components at all frequencies, i.e., for a small enough frequency band this mean squared deviation scales with Δf:

$$\langle \Delta I(t|f_0, \Delta f))^2 \rangle = S_I(f_0) \cdot \Delta f, \tag{4.1}$$

where $S_I(f_0)$ is the spectral density of the current noise. The mean squared deviation of the current is obtained as the integral of the noise spectral density:

$$\langle (\Delta I)^2 \rangle = \int_0^\infty S_I(f) \mathrm{d}f. \tag{4.2}$$

In practice, the noise is evaluated by discrete-time Fourier transform, it can be shown, that the spectral density can be calculated from the measured discrete data points as:

$$S_I(f) = \frac{2\Delta t}{N} \left\langle \left| \sum_{n=0}^{N-1} I(n \cdot \Delta t) \exp\left(-i 2\pi f n \Delta t\right) \right|^2 \right\rangle, \tag{4.3}$$

where Δt is the time between subsequent sampling events, and the averaging is performed for different time traces, each containing N data points.

4.1.2 Types of noise

There are multiple sources of electronic noise, which are essential from a technological and research point of view. It is imperative to note that the S_I noise spectral density is additive, which means that the measured noise of a system potentially sums up multiple sources or types of noise from the investigated system and the experimental setup as well.

Johnson–Nyquist (thermal) noise

At finite temperature, the thermal fluctuation of charge carriers generates current fluctuation with the spectral density of

$$S_I = 4 k_\mathrm{B} T G, \tag{4.4}$$

where k_B is the Boltzmann constant, G is the ohmic conductance of the system, and T is the absolute temperature. Thermal noise was first experimentally observed by Johnson [97] and theoretically explained by Nyquist [98], giving it a more commonly used name. The Johnson–Nyquist noise is an equilibrium noise, appears regardless of the applied voltage, and depends solely on the T temperature and the G conductance of the investigated system. Therefore, Johnson–Nyquist noise is present in all systems, serving as the lower resolution limit to any type of electrical measurement. For instance, the input current noise of a current amplifier is basically limited by the thermal noise of its feedback resistor. However, Johnson–Nyquist noise is not necessarily a limitation but serves as the basis for thermometry techniques that can also be used for the high-precision measurement of the Boltzmann constant [99, 100].

Shot noise

The shot noise is generated by the random detection of the quantized electric charges of discrete electrons and, therefore, is a non-equilibrium noise. It can be observed in systems where the emitted electrons are uncorrelated, following a Poissonian emission process. In 1918, Walter Schottky introduced shot noise when he observed stochastical current fluctuations in vacuum tubes [101]. Another system that exhibits the Poissonian process of electron emission is a p-n junction. In both systems, electrons with randomly distributed energies must overcome an energy barrier to traverse. The spectral density of true Poissonian current noise is described with e elementary charge of electrons and $\langle I \rangle$ mean current as follows

$$S_I = 2e \langle I \rangle . \tag{4.5}$$

The correlated nature of electrons in highly transmitting channels suppresses the shot noise in atomic-sized contacts [37, 102]. The set of transmission eigenvalues determines the measured sub-Poissonian shot noise; a tunnel junction with multiple weakly transmitting channels approaches the Poissonian limit while one fully transmitting channel exhibits no shot noise.

1/f-type (flicker) noise

The main focus of the noise analysis in this work is the investigation of $1/f$-type noise, which is named after the typical frequency dependence of the spectral density given as

$$S_I(f) = \beta \cdot (f/f_0)^{-\gamma} , \tag{4.6}$$

where β is the magnitude, f_0 is a reference frequency, which can be chosen as $f_0 = 1$ Hz and the γ exponent is around unity but can vary in the range $\gamma = 0.8-1.45$ for different systems [94]. The broad range of exponents implies that the $1/f$ nature is not universal, additionally, different systems may exhibit distinct physical processes responsible for the $1/f$-type noise. The electronic $1/f$-type noise is usually a conductance (resistance) noise originating from the fluctuation of the conductance (resistance) induced by diverse physical processes.

Conductance (resistance) fluctuations are generated by the variation of the trapped charge in the oxide layer of metal-oxide-semiconductor field effect transistors (MOSFETs) [94, 103] or electron scattering on dynamical defects in metallic systems [104], among other effects. In many cases, this is a steady-state conductance (resistance) noise, which is present without the application of an electronic driving signal (e.g., voltage). It can be described by the $S_G(f)$ or $S_R(f)$ conductance or resistance noise spectral densities, which are defined similarly for the $G(t)$ and $R(t)$ conductance and resistance variations, as $S_I(f)$ for the current noise (see Eq. (4.1)).

First, I discuss the frequency dependence of $S_G(f)$ considering a single fluctuator with a single τ characteristic time. For this process a correlation function of the temporal conductance variation can be defined, $C_G(\Delta t) = \langle \Delta G(t) \cdot \Delta G(t + \Delta t) \rangle_t$, which - due to the single τ characteristic fluctuation time - can be considered as an exponential correlation function, $C_G(\Delta t) = \langle \Delta G^2(t) \rangle_t \cdot \exp(-\Delta t/\tau)$. I note that from here on, the notation $\langle\ \rangle$ will denote the averaging in time domain (instead

of the explicit notation $\langle\ \rangle_t$). It can be shown, that $S_G(f)$ is twice the Fourier transform of the $C_G(\Delta t)$ temporal correlation function (Wiener–Khinchin theorem), from which

$$S_G(f) = \frac{4\left\langle \Delta G^2(t) \right\rangle \cdot \tau}{1 + (2\pi f)^2 \tau^2}, \tag{4.7}$$

follows, i.e., a Lorentzian function describes the conductance noise spectral density, which is constant at $f \ll (2\pi\tau)^{-1}$ and decays with $1/f^2$ at $f \gg (2\pi\tau)^{-1}$. Such spectra are demonstrated by the red lines in Fig. 4.1, each curve corresponding to a different τ. Note, that this type of noise is called $1/f^2$ noise in the high-frequency limit, whereas in the time domain, it is frequently manifested as a random telegraph noise (RTN), i.e., the conductance is jumping back and forth between two characteristic values.

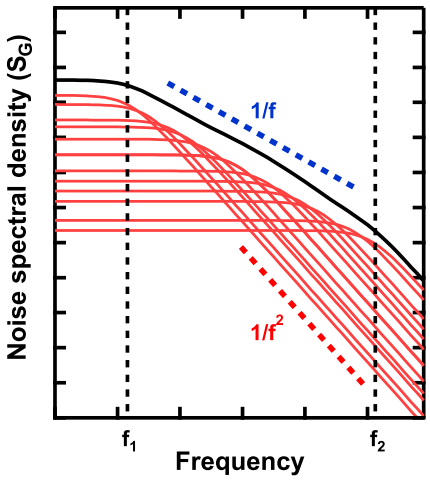

Figure 4.1: *Simulation of $1/f$-type spectrum (black line) formation as a superposition of Lorentzian spectra (red lines) with continuously distributed characteristic time scales in between τ_1 and τ_2. The Lorentzian shape dominates at frequencies under $1/(2\pi\tau_2)$ and above $1/(2\pi\tau_1)$, as illustrated by the black dashed lines. The blue (red) dashed line serves as a guide to the eye illustrating a slope of $\gamma = 1$ (2). The curves are shown on a logarithmic-logarithmic scale. Based on a figure from Ref. 104.*

The superposition of multiple relaxation processes with continuously distributed characteristic time scales between τ_1 and τ_2 yields a significantly shallower frequency dependence than the $1/f^2$ scaling of an individual Lorentzian spectrum. In this particular case the black noise spectrum follows a $1/f^\gamma$ scaling with $\gamma = 1$ (see blue dashed guideline), but the actual slope depends on the distribution of the fluctuation time constants, and therefore different γ values are also realistic.

In a point-contact system, the contribution of individual fluctuators to the noise can vary based on their location: a fluctuator in the active region of the constriction can induce an emerging Lorentzian spectrum superimposed on the $1/f$-type spectrum of a remote ensemble of fluctuators. Such mixed spectra are

observable in the majority of measurements in Ta_2O_5-based memristors. Fig.4.2 demonstrates an example of $1/f^\gamma$ scaling (blue line), and a mixed spectrum (black line). The mixed spectrum can be fitted as the sum of a Lorentzian (red dashed line) and $1/f$-type (blue dashed line) spectrum. The inset illustrates a point-contact device with a single fluctuator at the constriction (red) and an ensemble of remote fluctuators (blue). The possibilities and difficulties in decomposing a mixed spectrum to a Lorentzian and a $1/f$-type curve will be discussed in Section 4.3 in more detail.

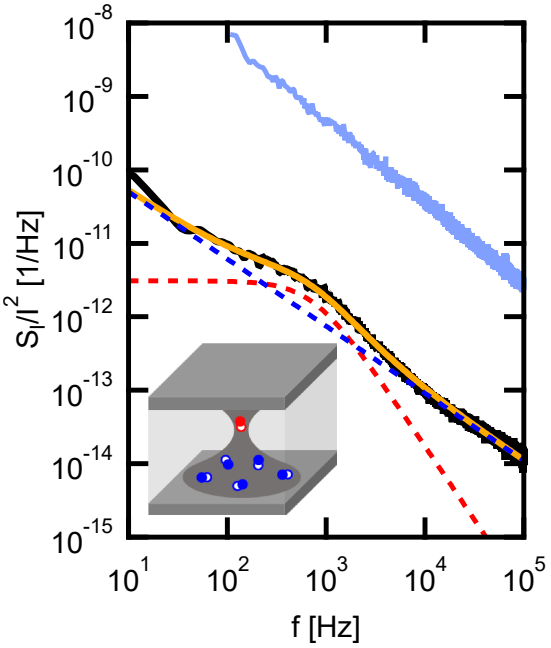

Figure 4.2: *$1/f$-type spectrum (blue) and mixed spectrum (black) observed in a Ta_2O_5-based memristive device. The inset illustrates the constriction in the point-contact system. The mixed spectrum is formed by an emerging Lorentzian spectrum from a single fluctuator near the constriction (red fluctuator in the inset) superimposed on the $1/f$-type spectrum of a remote ensemble of fluctuators (blue fluctuators in the inset). Figure from Ref. 104.*

Next, I discuss the voltage dependence of the noise spectra. If steady-state conductance fluctuations are considered, and no further fluctuations are excited by the applied voltage, the $S_G(f)$ conductance noise spectral density is considered to be voltage-independent. In a measurement, however, usually current noise is measured, for which the $S_I(f) = S_G(f) \cdot V^2$ voltage dependence follows due to the $\left\langle (\Delta I)^2 \right\rangle = \left\langle (\Delta G)^2 \right\rangle \cdot V^2$ relation by Ohm's law. This means, that $S_I(f)$ is not a good measure of the conductance noise, but $S_I(f)/I^2$ already eliminates this obvious voltage dependence.

To quantify the observed noise in a technologically relevant measure, I will frequently use the noise-to-signal ratio, or in other words the $\Delta x/x$ relative noise of the measured quantity x. For current noise, the $\Delta I/I$ relative current fluctuation

is obtained by normalizing the

$$|\Delta I| = \sqrt{\int_{f_1}^{f_2} S_I(f)\mathrm{d}f} \tag{4.8}$$

quantity to the mean current I, where f_1 and f_2 define the frequency band of the analysis, which should be obviously inside the frequency band of the measurement, meaning that f_2 is smaller than the $1/2\Delta t$ Nyquist frequency, whereas f_1 is larger than the $1/(N\Delta t)$ frequency resolution. Note that the ΔI is the measure of current fluctuations, therefore $\Delta I = |\Delta I|$ is considered. According to the above consideration on the voltage dependence of $S_I(f)$, the relative current fluctuation $(\Delta I/I)$ should be also voltage-independent, if two conditions are satisfied: (i) steady-state fluctuations are concerned, i.e., the voltage does not excite further fluctuations, (ii) Ohm's law is valid, i.e., no nonlinear conduction features appear in the range of the noise analysis. This regime is studied by linear noise spectroscopy, and in this case, $\Delta I/I = \Delta G/G$ is also satisfied. A non-voltage-independent $\Delta I/I$ relative noise (in the regime of nonlinear noise spectroscopy investigated in Section 4.4.2) always demonstrates that the latter (i) and (ii) requirements are not satisfied, either the voltage excites fluctuators, or nonlinear conductance features are observed. In case of a nonlinear $I(V)$ curve, the transport nonlinearity is converted to nonlinear noise features, and this conversion heavily relies on the relevant fluctuating parameter in the transport model, i.e., nonlinear noise spectroscopy is efficient in identifying the source of the fluctuation [104, 105]. The latter features will be discussed in Section. 4.4.2, mainly concentrating on the excitation of further fluctuators as the switching threshold voltage is approached.

4.2 Literature review of noise spectroscopy results

A straightforward motivation behind low-frequency noise spectroscopy is understanding noise sources to eliminate them and improve the signal-to-noise ratio. Excellent examples include the research of Balandin *et al.* [106] about tuning the $1/f$-type noise to optimize the performance of GaN/AlGaN field-effect transistors. Later, Balandin presented in Ref. 107 the systematic noise reduction of graphene devices by tuning sample fabrication methods. In a recent work, noise reduction in a memristive system was also published, Saketh Ram *et al.* [108] presented the substantial reduction in the $1/f$-type noise in a HfO_x-based memristor by controlled oxidation of an interface layer.

Instead of optimizing sample fabrication methods, an electrical operation protocol is another approach for noise reduction in memristive systems. For example, noise reduction by repeated switching cycles was demonstrated in Ref. 109 on Y_2O_3-based, and in Ref. 110 on TiOx-based memristors. In another paper, which was introduced earlier in Fig. 2.5, Rao *et al.* [24] reported on the denoising by subthreshold pulse pairs on commercially available $Pt/HfO_2/Al_2O_3/Ti/Ta$ devices, enabling the multilevel programming with a record high resolution of 11 bits, 2048 discrete conductance levels. They used a denoising routine to eliminate conductance

fluctuations if necessary to have no overlap in the neighboring states. Fig. 4.3(a) demonstrates the result of a denoising process, the current signal measured at 0.2 V of an initial (blue) and the denoised (red) state. The denoising was executed by applying at least one positive-negative pulse pair of 350 mV amplitude to the initial state that exhibits high noise. The process reduces the conductance fluctuations by a factor of 7, enabling a high-resolution multilevel programming which is demonstrated in panel (b) by three neighboring levels with a spacing of 0.026 G_0. The authors explained the high noise levels as a result of incomplete conduction

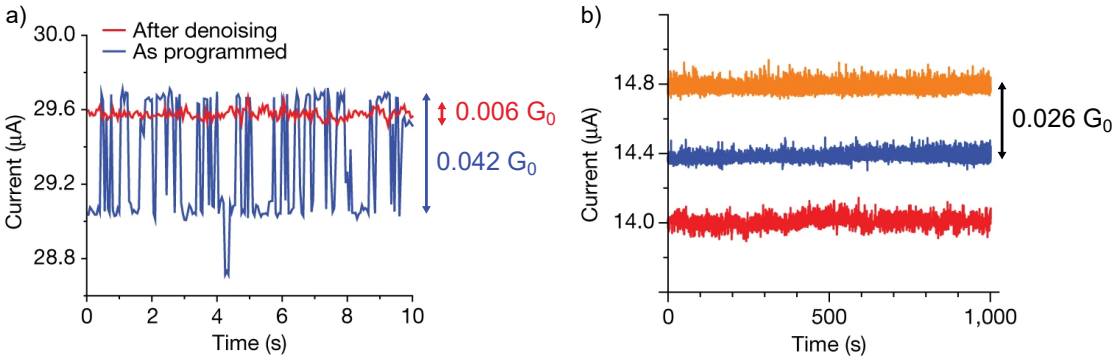

Figure 4.3: *(a) Example of the effectiveness of the denoising process. The initial (blue) current signal exhibits a large variation which is reduced by a factor of 7 (red signal) after applying at least one positive-negative pulse pair of 350 mV amplitude. (b) Current signals of three neighboring states after denoising. All signals measured at 0.2 V. Results from Ref. 24 with conductance fluctuations and spacing values indicated by me.*

channels in the oxide layer, and the denoising involved removing or completing such channels. These mentioned noise reduction procedures mainly affect the lower conducting states of memristors, while the noise in the high conductance regime is mostly unaltered. The decreased noise level is most likely due to eliminating a random telegraph noise (RTN), that is, the elimination of a single dominant fluctuator. Furthermore, none of these papers present the statistical analysis of these protocols. The results of my research will give insights into some of the open questions about noise tuning in Section 4.4.2.

Understanding noise characteristics often enables the tailoring of noise levels; however, in some cases, the objective is not the reduction but the tuning of the noise to an optimal level. Cai *et al.* [111] demonstrated a memristor-based neuromorphic architecture capable of annealing-inspired computing by harnessing the intrinsic hardware noise. Borders *et al.* [112] proposed an integer factorization method and demonstrated the proof-of-concept realization by utilizing the stochastic behavior of magnetic tunnel junctions. Li *et al.* [113] and Wen *et al.* [114] showed how the highly stable RTN can be used as an entropy source of true random number generator circuits, tested with RTN of TiO_2-based and h-BN-based memristors, respectively.

From a pure physics perspective, the analysis of $1/f$-type noise spectra serves as a tool to reveal the underlying charge transport mechanisms in the studied systems,

as well as identifying the physical sources of the fluctuations. It was presented in the introduction that $1/f$-type noise is the superposition of multiple relaxation processes with continuously distributed characteristic time scales (see Fig. 4.1). It was also demonstrated how a single fluctuator near the constriction can induce an emerging Lorentzian spectrum superimposed on the $1/f$-type spectrum of the remote ensemble of fluctuators (see Fig. 4.2.). The usual resistive switching devices are prone to this behavior due to narrow constriction in the active region. In the measurements, a dominant individual fluctuator appears as an RTN, which is the fluctuation between at least two discrete signal levels. Many research groups presented detailed analysis of dominant RTNs in HfO_x-based [115–119] and TaO_x-based [120] memristors. Depending on the contribution of the RTN, one can observe a Lorentzian-like or mixed spectra, which was also reported in the literature, in HfO_x-based [121, 122] and TaO_x-based [123, 124] memristors.

A further highly interesting feature in resistive switching devices is the resistance scaling of noise. Such investigation is highly important as resistance tuning is an intrinsically important feature from the application point of view. There is research on resistance scaling of noise in Cu-containing metal oxide-based [125], NiO-based [126, 127] and HfO_x-based memristors [128, 129]. Some of these resistance scaling results are summarized in Fig. 4.4, showing a considerable variation of noise and an increasing trend with increasing resistance that often saturates in the high resistance regime. The saturation is consistent with the resistance-independent noise induced by the gap fluctuation of an atomic tunnel junction [104, 105, 130]. The slope in the conducting region of these samples reveals information about transport properties [104, 131, 132]. The noise results on pure Au break-junctions by Wu *et al.* [133] plotted in panel (d) reveal an additional feature, the change of slope attributed to the crossover between diffusive and ballistic transport region.

All presented results quantify the measured noise by different parameters. Some results work with the relative noise $\Delta R/R$ or $\Delta I/I$, which are equivalent in case of noise induced by resistance fluctuations. While others show the normalized spectral density S_I/I^2 or S_V/V^2 at a specified frequency. I note that it also common in literature to calculate the Hooge parameter $S_I/I^2 \cdot f$ [94]. Ideally, in a $1/f$-type dependence, all these approaches should describe noise similarly as these quantities are strongly related to each other. In practice, however, the noise spectra can have peculiar frequency dependence if a dominant individual fluctuator results in Lorentzian or mixed spectra. Also, pickup noise can distort given frequencies. In such cases, evaluating the normalized spectral density only at a specified frequency is not ideal. A more general method is to use the integral of the spectral density and, based on Eq. (4.8), obtain the relative noise of a specified frequency range included in the measurement frequency window. As a result, the resulting relative noise is well-defined, where various measurements with different measurement conditions are still comparable as long as the same specified frequency range is used for evaluation. Furthermore, the relative noise only weakly depends on the choice of the frequency range. To express the dependence quantitatively, I consider the two characteristic types of noise spectra and calculate based on the reference integral limits $f_1 = 100$ Hz and $f_2 = 50$ kHz used in this research. (i) The mean squared deviation calculated from the integral of a $1/f$-type spectrum scales with

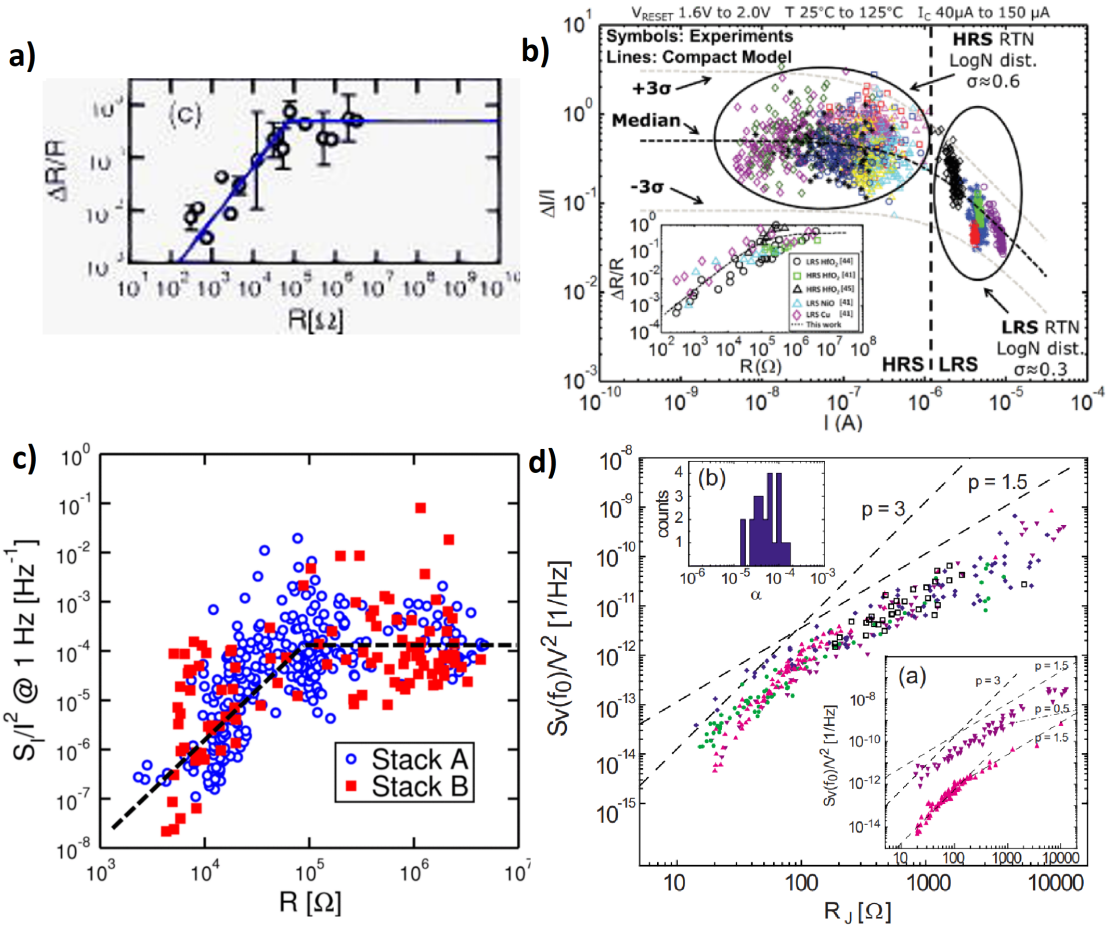

Figure 4.4: *Resistance scaling of the noise on different memristor devices, exhibiting a crossover between different slopes attributed to different transport regimes. (a) W/NiO/Pt memristor from Ref. 127. (b) TiN/Ti/HfO_2/TiN memristor from Ref. 129. (c) Memristor with Cu-containing active electrode and metal oxide switching medium, different colors denote two alternative metal oxide layers. From Ref. 125. (d) Pure Au break-junction resistive switch from Ref. 133.*

$\sim \ln(f_2/f_1)$, therefore a 2 orders of magnitude bandwidth increase (in any direction) would only yield a $\approx 30\%$ increase of $\Delta I/I$. (ii) In the case of a Lorentzian spectrum the mean squared deviation scales with $\sim (\arctan(2\pi\tau \cdot f_2) - \arctan(2\pi\tau \cdot f_1))$. Although the integral strongly depends on the $(2\pi\tau)^{-1}$ cut-off frequency, as long as it is inside the measurement window, the bandwidth extension will only weakly influence the $\Delta I/I$ value. As a specific example, if the corner frequency of the Lorentzian is positioned in the middle of the reference band along the logarithmic axis ($(2\pi\tau)^{-1} = 2.2\,\mathrm{kHz}$) the 2 order of magnitude extension of the reference band towards higher (lower) frequencies would only yield a 1.5% (1.5%) increase of $\Delta I/I$.

The integral of the spectral density for the evaluation method of the relative noise is followed by our research group, yielding for example the extensive study of different memristive materials published in Ref. 132. Fig. 4.5 shows the comparison of Nb_2O_5-based and Ta_2O_5-based VCM-type and Ag_2S-based ECM-type memristors.

Panels (a)-(c) show the resistance scaling of the relative noise (black squares) obtained from the noise spectral density integral, with additional information about the contribution of single fluctuator Lorentzian noise on the right scale (see Fig. 4.2 for a mixed spectrum demonstrating a single dominant Lorentzian). See a more detailed description of all plotted quantities in the caption. The oxide-based memristors exhibit an overall lower noise in comparison to the Ag_2S-based ECM-type device while having a significantly increased contribution of dominant single fluctuators.

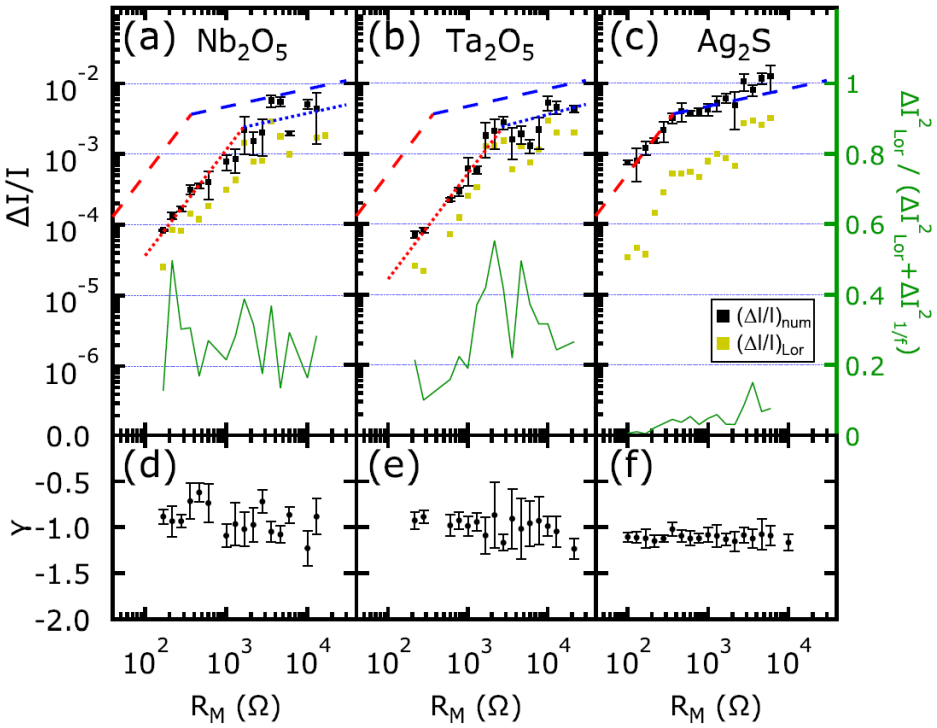

Figure 4.5: *(a-c) Comparison of the resistance scaling and Lorentzian contributions of Nb_2O_5-based and Ta_2O_5-based VCM-type and Ag_2S-based ECM-type memristive devices. The relative noise data is averaged into resistance bins on a logarithmically equidistant scale. The black and yellow squares show the $(\Delta I/I)_{\mathrm{num}}$ relative noise calculated from the numerical integral, and the $(\Delta I/I)_{\mathrm{Lor}}$ contribution of a single nearby fluctuator to the relative noise calculated from the Lorentzian contribution in the analytical fitting, respectively. The green lines present the relative contribution of the Lorentzian to the total noise. Each resistance scaling is fitted by theoretical curves in the diffusive (red dashed line) and the ballistic (blue dashed line) regime. The fitting lines of the Ag_2S system are plotted on each panel for comparison. (d-f) The average γ exponents of the $1/f^{\gamma}$ fitting component. Results from the detailed analysis of Ref. 134.*

These results are significant not only because the noise of these materials has not been studied in such detail yet but also because the point-contact model proposed by Halbritter *et al.* was successfully applied to reveal the diffusive-ballistic crossover

[131, 134]. To address the amplitude of the $1/f$-type noise, $\Delta G/G$ relative noise can be calculated with ΔG change in conductance attributed to electrons scattering on dynamical defects, such as two-level systems. The diffusive (ballistic) regime is distinguished by the junction diameter being larger (smaller) than the mean free path, yielding a G conductance expressed by the Maxwell (Sharvin) formula. Quantitatively, $G_{\text{diff}} = d/\rho$ and $G_{\text{ball}} = G_0(k_{\text{F}}d)^2$ where ρ is the resistivity, d is the junction diameter and k_{F} is the Fermi wavenumber. The ΔG conductance fluctuation resulting from a scattering event is also different in the diffusive and ballistic regime. It can be proven that the former case is reduced to $\Delta G_{\text{diff}} = \Delta G_{\text{ball}} \cdot (l/d)^2$ where l is the mean free path. Based on these considerations, the slope of the conductance dependence of the relative noise shows a $\sim R^{3/2}$ and $\sim R^{1/4}$ dependence in the diffusive and ballistic regime, respectively.

In Fig 4.5(b),(e), the $Ta/Ta_2O_5/PtIr$ sample was measured with scanning tunneling microscopy break-junction technique, which has advantages but is not scaleable for typical memristive applications. For such purposes, it is common to use a crosspoint structure, which will be introduced in Section 4.3.3. The research of Ref. 132 also showed that the resistance scaling of $Nb/Nb_2O_5/PtIr$ scanning tunneling microscopy break-junction (STM-BJ) and $Al/Nb_2O_5/Pt$ crosspoint structure is following the same trends. In this chapter, in Section 4.4.1, I will present measurements on $Ta/Ta_2O_5/Pt$ crosspoint samples, which turn out to follow a distinct trend from what was measured with STM-BJ. Also, I will show additional analysis regarding the contribution of Lorentz and $1/f$-type noise.

Another essential and insightful topic is the bias dependence of the $1/f$-type noise. The bias dependence of $1/f$-type noise in an ohmic sample is expected to be proportional to the square of bias voltage, which is also reported for HfO_x-based memristors [121, 122], NiO-based devices [126] and in the work of our research group for Ag_2S-, Nb_2O_5- and Ta_2O_5-based devices [104, 132, 134]. Once the steady state of the ohmic regime is exceeded, voltage-induced fluctuations will result in the deviation from the V^2 dependence. Even more interesting is the case if voltage-induced fluctuations are observed in the linear transport regime since that enables the study of the nonlinear noise decoupled from any non-ohmic transport behavior. In other words, the nonlinear noise of highly linear characteristics is solely due to voltage-induced fluctuations. For this reason, the material choice of Ta_2O_5 is ideal due to its rather linear $I(V)$ characteristics. At the end of his doctoral research, Botond Sánta measured nonlinear bias dependence of the noise in the still highly linear voltage regime of Ta_2O_5 STM point-contact (STM-PC) devices, an example is shown in Fig. 4.6. Later, the beginning of Section 4.4.2 will elaborate on the voltage-dependent measurement scheme in more detail. The main idea is that a complete memristive switching is executed by applying a non-continuous, staircase voltage signal consisting of discretized voltage plateaus. Panel (a) shows the continuous $I(V)$ characteristics (green) together with a subsequent voltage-dependent noise measurement. The average current values at each voltage plateau are denoted by cross markers, with colors indicating HCS (blue) and LCS (red). The resistance values in panel (b) confirm the high linearity of the HCS and the low-voltage regime of the LCS. Particularly interesting is the evolution of relative noise in panel (c) in the segments before the transitions. The relative noise

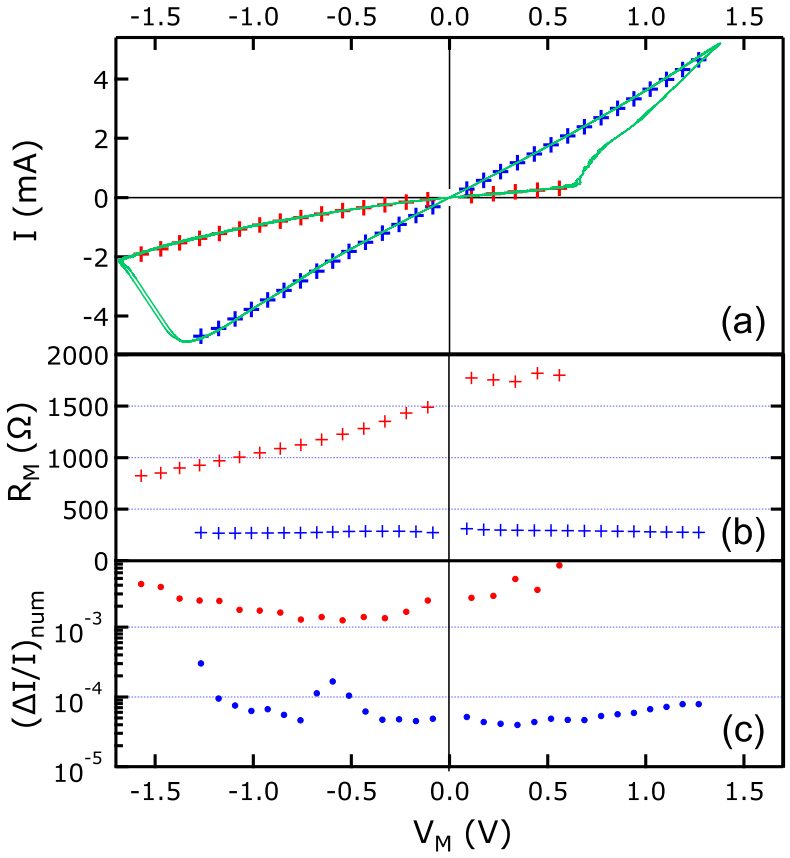

Figure 4.6: *Voltage-dependent noise measurement of a Ta_2O_5-based memristive switching, (a) current-voltage characteristics, (b) resistance-voltage characteristics, (c) relative noise obtained from the numerical integral of the noise spectra. Botond Sánta measured the nonlinear bias dependence of the noise in the still highly linear voltage regime, which is attributed to a precursor anticipating the switching. Results from Ref. 62.*

preceding both, the set transition (positive voltages in the LCS (red)) and the reset transition (negative voltage regime in the HCS (red)) demonstrate a significant, nearly an order of magnitude increase with the voltage while exhibiting a linear transport regime, i.e., stable conductance. This observation could be consistent with a precursor effect predicting the forthcoming resistive switching. However, there were still several questions about how to interpret these results correctly and additional technical limitations to solve. During my research, I conducted a plethora of noise measurements to explain the nonlinear voltage dependence, which also resulted in a deeper understanding of the tunability of noise, which is presented in Section. 4.4.2.

4.3 Experimental techniques

4.3.1 Noise measurement setup

The measurement of extremely low levels of noise poses diverse technical challenges. First, it is crucial to eliminate all instrumental noise sources by utilizing screened connectors and cables, as well as shielding the investigated sample in a Faraday cage, ideally a solid, tightly closed metal box. Even the applied voltage has to be as noise-less as possible, which can be improved by a low-pass filter. It is also essential to avoid any ground loops. The small variation of the measured signal has to be amplified and then measured by a digitizer with high resolution, high sample rate, and, most importantly, an included anti-aliasing filter. Additionally, the measured current noise is only translated properly from conductance noise if the bias voltage on the sample stays steady during measurement. Considering these requirements, the measurement setup is built up as presented in Fig. 4.7. An Agilent 33320A

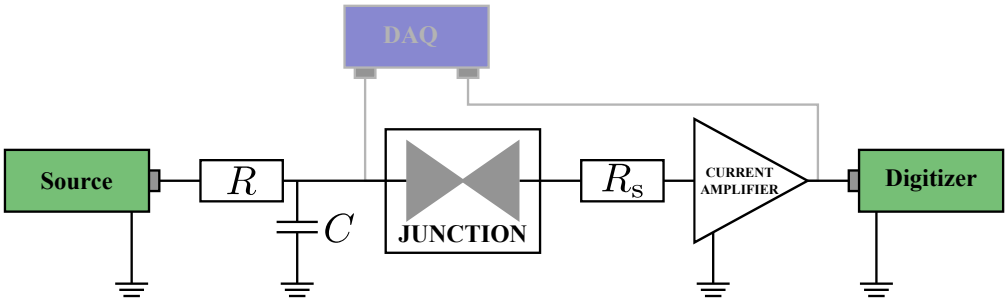

Figure 4.7: *The noise measurement setup and optionally included data acquisition card (DAQ) for electrical characterization measurements. The arbitrary waveform generator outputs the voltage through the RC low-pass filter, the sample, and the instrumental serial resistances. The current on the sample is amplified by the current amplifier and measured with a high-resolution digitizer with an aliasing filter.*

arbitrary waveform generator serves as a voltage source with an RC filter on the output, which is tuned in accordance with the time scale of the actual measurement. Although no extra serial resistance is used due to maximizing the applied bias voltage on small resistance samples, the input impedance of the Femto DLPCA-200 current amplifier, the resistance of the RC filter, and the output impedance of the Agilent have to be considered to obtain the actual bias voltage on the sample. The current amplifier has a gain-dependent bandwidth, which practically limits the measurement bandwidth to 500 kHz. At the end of the line, the National Instruments PXI-5922 digitizer is used for measuring the amplified current signal. This device has a maximal 24-bit resolution and maximal 6 MHz aliasing-free bandwidth.

The noise measurement sequence is controlled by a complex LabVIEW measurement program, which was developed and improved by several contributors over the years, including András Magyarkuti, Zoltán Balogh, Dávid Krisztián, and Botond Sánta. The noise measurement system provides the advanced option to apply an arbitrary voltage signal to the sample. Zoltán Balogh developed an IGOR

Pro program code with a graphical user interface that enables the quick and easy generation of typical waveforms used in the measurements. As the following results will show in detail, the generated waveforms are mostly staircase triangular signals. During my research, I also contributed to the development of these measurement control programs.

The noise spectroscopy of any sample is first prepared by electric characterization measurement to e.g., confirm a stable switching or tune the system to a desired conductance. Technically, this can be performed with the same setup as described above. However, the noise measurement control and evaluation program is not optimized for such endeavors; thus, on most occasions, it is more advantageous to use the same setup already presented in Fig. 3.13 in Section 3.2.1, which was also used for pure atomic switching. In Fig. 4.7, gray outlines indicate the National Instruments USB-6363 data acquisition card (DAQ) optionally included in the system. The conductance of the investigated sample is measured with the LabVIEW measurement program developed by András Magyarkuti [65], which is easy to use, offers real-time monitoring of the conductance and immediate plots of $I(V)$ characteristics. Meanwhile, all these features are not available in the noise program. However, one critical concern is the ground loop introduced by the DAQ loop, which has to be disconnected during noise measurements. This is executed with a relay or manually unplugging the DAQ loop after electrical characterization.

The noise of the measured current signal adds up from not only the physical system under test but also the instrumental noises, described in the following equation:

$$S_I(f) = S_{I,\text{sample}}(f) + S_{V,\text{source}}(f)\cdot G^2 + S_{I,\text{amplifier}}(f) + S_{V,\text{amplifier}}(f)\cdot G^2 + \frac{S_{V,\text{digitizer}}(f)}{R^2_{\text{gain}}}, \tag{4.9}$$

where G is the conductance of the sample. All quantities and their noise properties are described in this paragraph. The resulting level of the instrumental noises often limits the resolvable physically relevant noise of the sample. As it will be evident, the noise of high conductance states in the Ta_2O_5-based memristor is small enough to approach the limit of the instrumental noise. Since $1/f$-type noise is increasing with the applied voltage, a solution can be to increase voltage for the spectral density to emerge above the limit. If changing the applied voltage is not possible, there are some alternative but limited options to reduce the instrumental noise and find a compromise. First, the National Instruments digitizer has a $S_{V,\text{digitizer}}$ voltage noise which is divided by the R_{gain} transimpedance of the amplifier. The Femto current amplifier introduces a constant $S_{V,\text{amplifier}} = 4\ \text{nV}/\sqrt{\text{Hz}}$ voltage noise and a gain-dependent current noise $S_{I,\text{amplifier}}$ [135] to the measurement. The voltage noise is translated into current noise as $S_{V,\text{amplifier}}/R^2$. The current noise generally decreases with increased gain; however, the output of the amplifier and the input of the digitizer are capped, not allowing the unlimited increase of the gain. Additionally, an increasing gain decreases the amplifier's bandwidth, drastically reducing the measurable frequency window for short measurements. Therefore, the compromise between the conductance of the sample, the maximum voltage, and the measurement time will determine the optimal gain setting. Finally, the $S_{V,\text{source}}(f)$ output noise of the Agilent source, which can be extensive, has to be

considered. Low-pass filtering can help to reduce the added noise, Fig. 4.8 shows zero-bias measurements through a 1 kΩ resistor with a set of different capacitors in the filter. The dashed horizontal line shows the expected noise level estimated from the Johnson-Nyquist noise of the 1 kΩ resistor and the added input noises of the current amplifier. The cut-off frequency of the RC filter can be tuned to

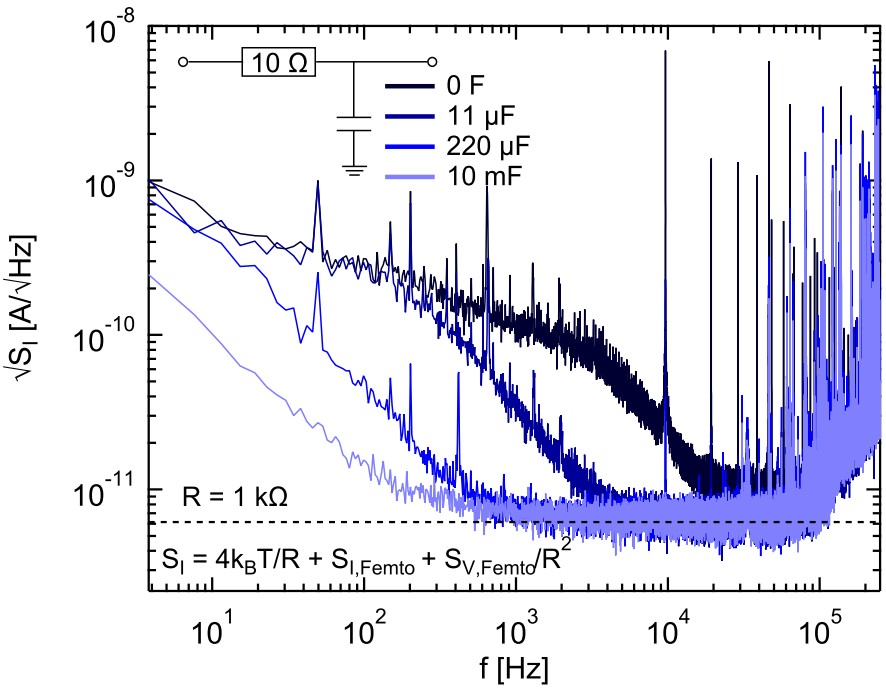

Figure 4.8: *The noisy output of the Agilent 33320A measured on 1 kΩ at zero bias can be reduced by the application of a proper RC low-pass filter to detect the Johnson-Nyquist noise of the 1 kΩ resistor. The dashed line represents the expected noise level estimated from the Johnson-Nyquist noise of the 1 kΩ resistor and the added input noises of the current amplifier.*

low frequencies as long as the measurement time is long enough to wait out the (dis)charge of the capacitor. Therefore, in measurements with a shorter time scale, only smaller capacitors can be used resulting in higher instrumental noise.

4.3.2 Evaluation of noise spectra

In the following, I will give insights into the evaluation of the noise measurements with a particular focus on effects observed in point-contact systems. The physically relevant noise has to be separated from the instrumental and the Johnson-Nyquist noise to investigate only the excess noise caused by $1/f$-type conductance noise.

The extensive and easily adaptable IGOR Pro evaluation program was developed by Zoltán Balogh with contributions from most users. I was strongly involved in the improvement of the program with an emphasis on transparency and generic evaluation procedures. The first step of the evaluation is the discrete-time Fourier transformation of the measured current signal to calculate the noise spectral density,

described by Eq. (4.3). Ideally, the measured current signal can be divided into segments, resulting in multiple Fourier transforms, which are averaged to obtain a clear spectrum. All measurements include a zero-bias noise spectrum, which is subtracted from all biased spectra; thus, only the excess noise is evaluated. Based on Eq. (4.8), ΔI is given by the integral of the spectral density. Without further evaluation, the numerical integral can be used to calculate the noise-to-signal ratio. The frequency band for noise-to-signal ratio evaluation has the limits 100 Hz and 50 kHz to yield comparable results to other works of our group. Alternatively, an analytical fit of the spectra can be executed to eliminate errors from pickup signals present in the numerical integral. In evaluating noise spectra, it is crucial to distinguish between the purely $1/f$-type spectrum of a remote ensemble of fluctuators and the Lorentzian spectrum of a fluctuator in the active region, and be prepared for mixed spectra containing both. It seems that it is reasonable to assume that the noise adds up from a pure $1/f^{\gamma}$ (see Eq. (4.6)) and a Lorentzian (see Eq. (4.7)) spectrum, as demonstrated in Fig. 4.2:

$$S_I(f) = S_{I,1/f}(f) + S_{I,\text{Lorentzian}}(f) = \beta \cdot \frac{1}{f^{\gamma}} + \frac{A \cdot \tau}{1 + (2\pi f)^2 \tau^2}. \tag{4.10}$$

The fitting is executed on the log-log scale, and the resulting analytical sum function can be used to calculate the noise-to-signal ratio. By analyzing the fitting, the analytical integral of the $1/f$-type and Lorentzian contributions can be calculated separately to obtain even more information about the behavior of the fluctuators.

Some examples of typical noise spectra in Ta_2O_5-based memristor are demonstrated in Fig. 4.9. The legends of the spectra show the parameters of the decomposed $1/f$-type and Lorentzian spectrum. Panels (a)-(b) introduce a mixed spectrum together with a segment of the corresponding current signal. When the fluctuator contributes more significantly to the transport, the current signal shows the typical RTN characteristics and a corresponding dominant Lorentzian spectrum, shown in panels (c)-(d). The decomposition of the noise spectrum is problematic since the frequency window determined by the measurement time scale and sample rate does not provide sufficient data points for the $1/f^{\gamma}$ fit. Finally, if the characteristic relaxation time of a dominant fluctuator is outside the measurement frequency window, the spectrum might only show the plateau or the steep $1/f^2$ slope of the Lorentzian function. Panels (e)-(f) is a great example of that, where a $\gamma = 1.94$ slope is misidentified as a $1/f$-type spectrum and an additional dominant fluctuator with a higher frequency cut-off. This example also raises attention to the difficulties of the spectral decomposition. Ideally, all fits are monitored manually, although there are difficult cases and measurements with huge numbers of spectra to oversee. In such cases, evaluating the noise-to-signal ratio from the numerical integral is still more advantageous. Alternatively, the fits can be filtered by an algorithm I implemented which automatically excludes unreasonable γ values, as well as fits with high fitting parameter uncertainty.

4.3.3 Fabrication of $Ta/Ta_2O_5/Pt$ crosspoint samples

The detailed noise spectroscopy measurements and evaluation were performed on $Ta/Ta_2O_5/Pt$ crosspoint devices fabricated by Miklós Csontos at ETH Zürich [136].

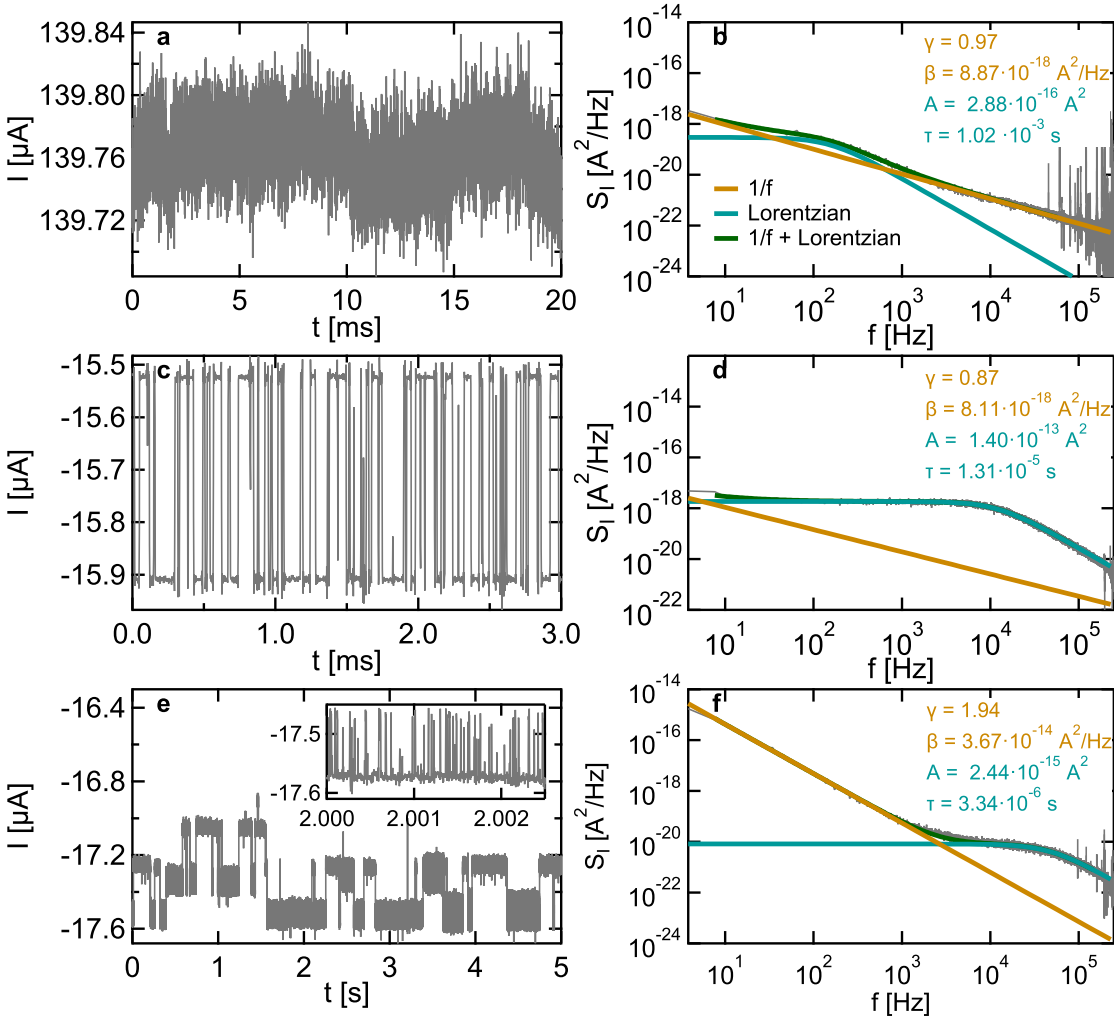

Figure 4.9: *Gallery of mixed spectra and segments of the corresponding current signals measured in $Ta/Ta_2O_5/Pt$ memristor. The spectra are decomposed to a Lorentzian spectrum of a significantly contributing fluctuator (cyan) superimposed on the $1/f$-type noise of a remote ensemble of fluctuators (gold). The final parameters of the fit are presented in the legends with the A Lorentzian magnitude. (a-b) There is no clear sign of individual fluctuator in the current signal, but the spectral density shows a Lorentzian emerging from the $1/f$-type spectrum. (c-d) The current signal shows clear indications of an RTN, and correspondingly, the Lorentzian spectrum dominates in the full frequency range, hindering the confident fitting of the $1/f$-type contribution. (e-f) Periodic fluctuations in the current signal with two different time scales appear in the noise spectral density as two dominant fluctuators. The automatic fit misidentifies the first Lorentzian since the measurement time is insufficient to resolve the low cut-off frequency. However, the fitted $\gamma = 1.94$ unambiguously indicates the cut-off of a Lorentzian curve.*

The sample is nanofabricated on top of a SiO_2 substrate, Ti adhesive layer of 10 nm, and Pt bottom layer of 40 nm thickness is deposited by electron beam evaporation. Subsequently, the 5 nm thick Ta_2O_5 is sputtered by reactive high power magnetron impulse sputtering. Then the 65 nm thick Ta top layer, and an additional Pt capping layer was sputtered on top of the Ta_2O_5 layer. An optical image of the resulting $Ta/Ta_2O_5/Pt$ crosspoint sample is demonstrated in Fig. 4.10. The device consists of multiple crosspoint samples arranged in a matrix structure

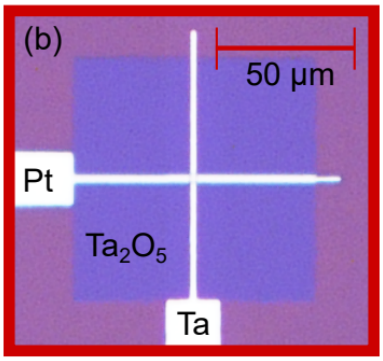

Figure 4.10: *An optical microscope image of $Ta/Ta_2O_5/Pt$ crosspoint sample. Image from Ref. 136.*

on the substrate chip. The contacting of the samples is performed the same way, as described earlier for lithographic planar Ag_2S-sample in Fig. 3.17(b)-(c). The chip is fixed on a printed circuit board, and the individual samples are connected to the copper leads by wedge bonding. The device is mounted in the sample holder, which now serves not as a vacuum chamber but as a Faraday cage. The switch box is equipped with ESD protection, where the sample connections can be switched to the ground with a serial 1 MΩ resistance.

4.4 Noise spectroscopy of Ta_2O_5-based memristors

The following section presents my experimental work on the $1/f$-type noise properties of Ta_2O_5 crosspoint memristive devices. First, in Section 4.4.1 I present my linear noise spectroscopy results. These experiments map the steady-state noise levels of the devices, also demonstrating a strong dependence on the actual conductance of the device. Next, in Section 4.4.1, I go beyond the regime of linear noise spectroscopy and study the noise properties all along the switching curves of the devices. This analysis demonstrates, that even in the fully linear, non-switching part of the $I(V)$ curve a strong noise increase can be observed as the switching threshold voltage is approached. Finally, a subthreshold cycling strategy is also demonstrated, which can be applied to reduce the steady-state noise level.

4.4.1 Steady-state noise characterization of Ta_2O_5-based memristors

The frequency, conductance, and bias dependence of the noise accurately describe the noise characteristics of memristors. Deviations from the frequency scaling of the $1/f^\gamma$ noise trend are frequent in Ta_2O_5-based devices, Fig. 4.9 already demonstrated spectra with significant contributions of a dominant Lorentzian from a single fluctuator. In this Section, I will mainly focus on the conductance dependence of the relative noise in the steady state, which is the regime where no bias dependence is observed in the relative noise, i.e., $\Delta I/I = \text{const.}$ or equivalently $(\Delta I)^2 \sim V^2$ while the conductance is constant (the $I(V)$ characteristics is linear).

The conventional method for mapping the conductance dependence of the $1/f$-type noise is demonstrated in Fig. 4.11, measured on $Ta/Ta_2O_5/Pt$ crosspoint sample, which adheres to earlier works of our research group [104, 132, 134]. Panel (a) demonstrates a representative $I(V)$ curve from a stable, reproducible memristive switching, panels (b)-(c) show the noise spectra and panel (d) plots the evaluated steady-state noise amplitudes in both states. First, the steady-state LCS (OFF state) is measured, corresponding results are presented in red, and then a set transition is executed by an applied half cycle to reach the HCS (ON state) for the noise measurements presented in blue. The S_I mixed spectra in both states of this example exhibit a significant contribution from a single fluctuator to the noise and the clear increase with increasing drive voltage. The black spectra are the base noise measurements at zero bias, and the blue and red dashed lines signify the expected base noise levels calculated from the current and voltage noise of the amplifier and the Johnson-Nyquist noise given by the device resistance and temperature. Only the excess noise is relevant to study the $1/f$-type noise, therefore the corresponding zero-bias base spectrum is subtracted from each voltage-driven noise spectrum. The mean squared deviation of the current is given as the integral of the noise spectral density between the predefined $f_1 = 100$ Hz $f_2 = 50$ kHz frequencies, annotated by the dashed vertical lines in panel (b). Note that the V_{drive} values in the legend are not equal to V_{bias} due to the nonzero serial resistance, but are only slightly different. The bias dependence in panel (d) agrees with the expectation for a steady state as

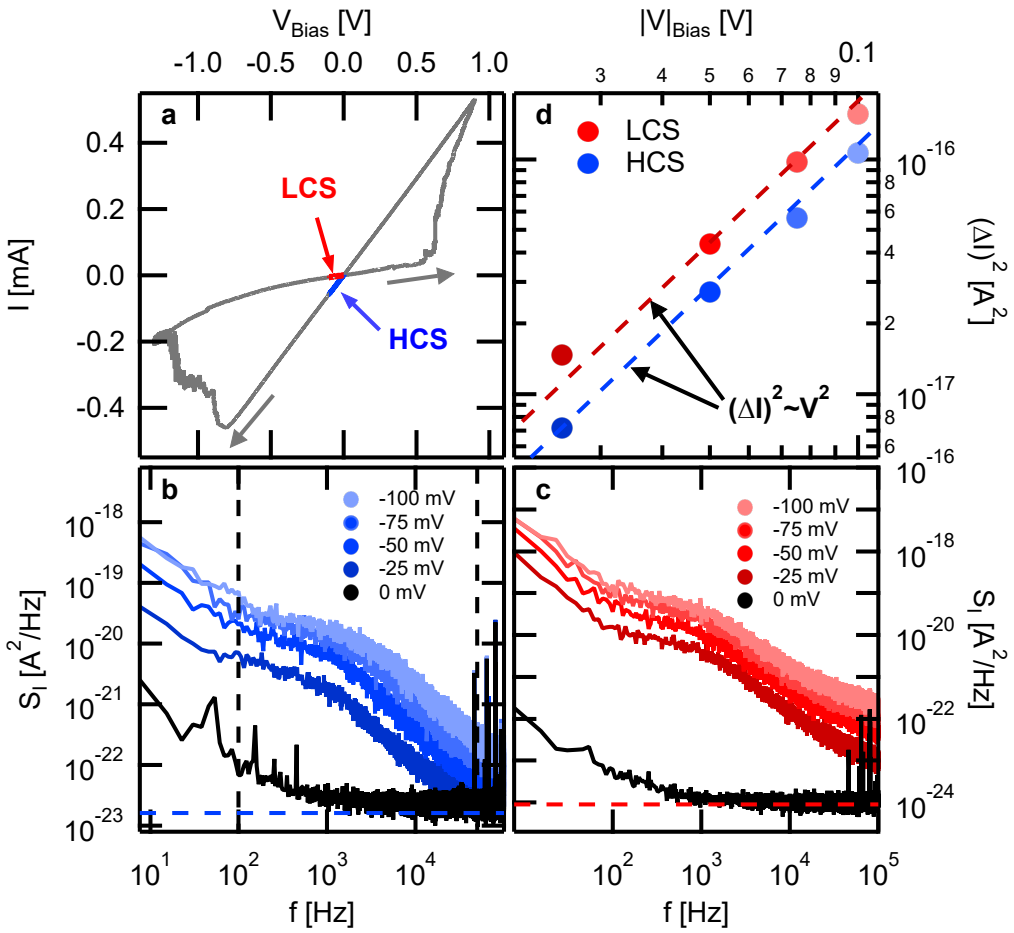

Figure 4.11: *Characterization of steady-state noise in the two states of a memristive switching. (a) Representative switching in a $Ta/Ta_2O_5/Pt$ crosspoint device with HCS of 7.6 G_0 and LCS of 0.65 G_0. Colored sections indicate the low-voltage region used in the steady-state noise measurement. (b-c) Voltage dependence of the noise spectral density obtained at the HCS (blue) and LCS (red) with the corresponding base noise spectra (black). The horizontal dashed lines represent the expected base noise level calculated from instrumental and Johnson-Nyquist noise. The vertical dashed lines indicate the frequency limits used for the integration to obtain the relative noise. (d) The steady-state current noise calculated from the spectra follows the expected V^2-dependence, colored dashed lines serve as a guide to the eye. Results to be submitted in Ref. P3.*

it follows a V^2-dependence.

I conducted the steady-state noise measurements in the low-voltage regime at a maximal of ±100 mV bias voltage (see the colored segments of the $I(V)$ characteristics in Fig. 4.11(a)) while the switching starts around +0.5/-0.8 V (for set/reset) in this example. Such low voltages are beneficial especially to ensure the high stability of the sample. This stability is ideal for noise measurements because it yields a better frequency resolution and enables a higher averaging of the spectra.

In practice, this is crucial for low noise levels of typically higher conductance states with spectra only slightly emerging from the base noise at low bias voltages. After the integral of the noise spectral density is obtained, the relative noise $\Delta I/I$ can readily be calculated. The resulting steady-state noise map, i.e., the conductance-dependent relative noise, in Fig. 4.12(a) is based on 148 investigated junctions from 9 different $Ta/Ta_2O_5/Pt$ crosspoint samples, and are denoted by different markers but all in red tones. For a proper statistical analysis, each junction is represented

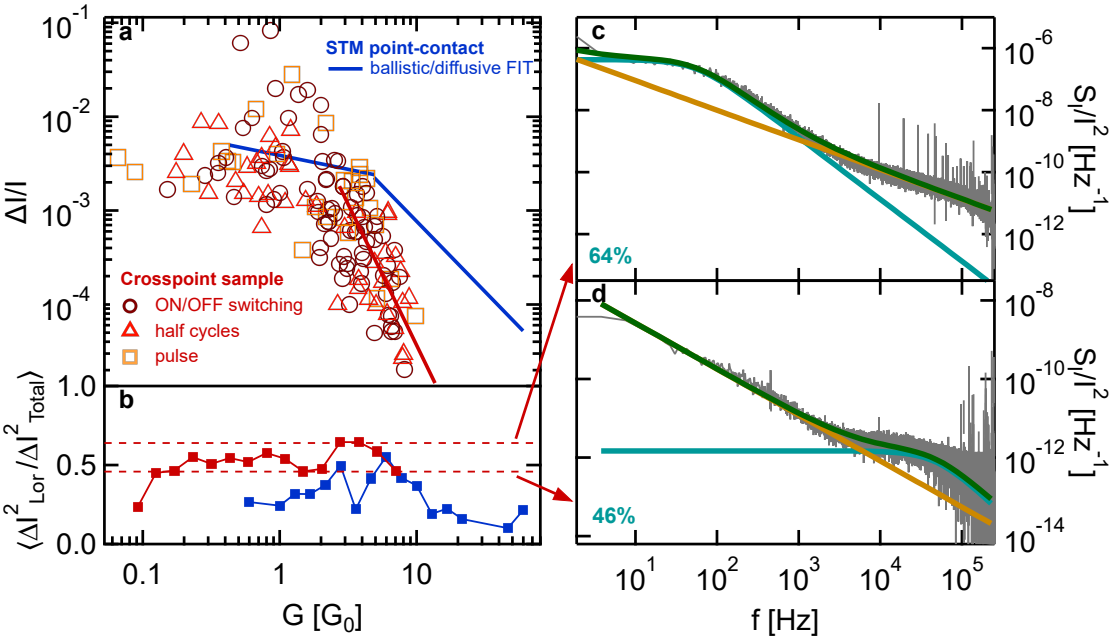

Figure 4.12: *(a) The noise map of 148 independent steady-state measurements in 9 different $Ta/Ta_2O_5/Pt$ crosspoint devices (red tones) compared to the trends observed in $Ta/Ta_2O_5/PtIr$ STM-PC samples (blue line) measured by Botond Sánta [132], see also Fig. 4.5(b). The technique of conductance tuning is indicated by different markers, showing no distinct behavior. (b) The most dominant single fluctuator's average contribution to noise was deduced from the Lorentzian fitting component for the crosspoint (red) and STM-PC (blue) devices. (c-d) Normalized noise spectra in a crosspoint device exhibiting Lorentzian contributions of 64% and 46%, which describe the typical maximal and minimal average contribution presented in panel (b) with the exclusion of the first bin due to the small number of included measurements. Color coding of fitting components: gold for $1/f^{\gamma}$, cyan for Lorentzian, and green for their sum.*

by 1 data point at a drive voltage of 100 mV if available, or 50 mV else. I conducted most of these measurements, a few together with BSc student György Lázár, and 45 data points are results obtained by Botond Sánta. Not only was the above-described method utilized for conductance tuning of the devices, but beyond states of stable, reproducible switching, there were states tuned by half cycles and voltage pulses. These different tuning methods are indicated with distinct markers. Based on these measurements, the conductance dependence of the steady state noise seems to be

universal in the sense that it does not depend on the chosen conductance tuning method or the actual state (OFF or ON). The latter state-independence was also demonstrated previously for various STM point-contact devices [132, 134].

The noise map shows a considerable variation of the relative noise with the device conductance: a rather conductance-independent relative noise up to around 1 G_0 and a steep decrease above. Work in our research group on Ta/Ta_2O_5/PtIr STM-PC samples conducted by Botond Sánta [132] successfully described the conductance-dependent noise by dividing the data into ballistic and diffusive conduction regions, as depicted in the introduction in Fig. 4.5(b). The blue lines in Fig. 4.12(a) correspond to the fits of the ballistic and diffusive transport regime with the crossover at 4.88 G_0 (change from ballistic regime to diffusive with the increasing conductance) reproduced from Ref. 132. Surprisingly, despite consisting of the same Ta_2O_5 switching medium material, these former STM-PC measurements clearly have higher relative noise levels and follow distinct trends in the high conductance regime. -Beyond the obvious differences in the STM-PC and crosspoint geometry, the growth of the Ta_2O_5 layer in the former was performed by anodic oxidation in contrast to the reactive high power magnetron impulse sputtering in case of the crosspoint samples.

Additional comparison is presented in Fig. 4.12(b), analyzing the contribution of a single fluctuator which is calculated as the ratio of the ΔI_{Lor} noise of the Lorentzian fitting component and the $\Delta I_{\mathrm{tot}}^2 = \Delta I_{\mathrm{Lor}}^2 + \Delta I_{1/f}^2$ total noise. During evaluation, the data is grouped into conductance bins spaced equidistantly on the logarithmic scale, and the average values for each bin are calculated. The average contribution of dominant fluctuators in crosspoint samples (51%) is significantly larger than in STM-PC samples (30%) which also implies that the device fabrication technique influences the fluctuator distribution in the samples. For an apparent demonstration of the meaning of the contribution, panels (c) and (d) present examples of noise spectra exhibiting a 64% and 46% Lorentzian contribution. These levels are indicated by the horizontal dashed lines in panel (b) and are chosen because they accurately describe the typical range of contributions in the crosspoint devices by excluding the first bin due to the small number of included measurements.

Next, I give some insight into the possible conductance dependencies of the relative steady-state noise levels. These issues are discussed in the review paper Ref. 104 written by our group, where it is demonstrated that in a barrier-like junction, the conductance is an exponential function of the possible fluctuating parameters (like the width or the height of the barrier), and this exponential dependence yields a mostly conductance-independent relative noise, which is the case for the studied Ta_2O_5 crosspoint devices at $G < 1\,G_0$ conductances. Another limiting case is also discussed in Refs. 104, 132–134, where a diffusive point-contact is considered with fluctuators distributed in the entire volume of the point-contact, yielding $\Delta G/G \sim G^{-1.5}$ conductance dependence of the relative noise (see the blue line in the high conductance regime of Fig. 4.12). A point-contact geometry is illustrated in Fig. 4.13. This type of geometry is a narrowing, which has a characteristic diameter d at the bottleneck, but it does not have a characteristic length, the junction diameter is the only determining dimension. For a diffusive

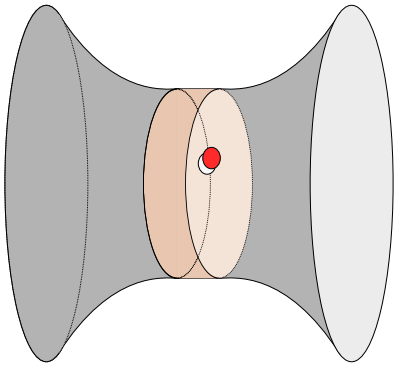

Figure 4.13: *Illustration of the point-contact geometry with a single fluctuator placed around the device bottleneck.*

point-contact, the conductance is approximated by the Maxwell formula [131, 137], $G_{\mathrm{PC}} = \sigma \cdot d$, where σ is the conductivity. In the following, I consider another relevant situation, where also a diffusive point-contact is considered, but the fluctuators are not distributed in the entire point-contact, only a *single* fluctuator is placed around the device bottleneck (see Fig. 4.13). In this case, the R_{PC} resistance of a point-contact is the sum of the resistances of slices, from which the light brown slice at the device bottleneck includes the single fluctuator, i.e., the ΔR_{PC} resistance fluctuation of the entire point-contact is the same as the $\Delta R_{\mathrm{slice}}$ resistance fluctuation of the slice containing the fluctuator. On the other hand, the slice can be considered as the parallel conductances of elementary volumes, from which only the elementary volume including the fluctuator fluctuates, i.e., the $\Delta G_{\mathrm{slice}}$ conductance fluctuation of the slice is the same as the $\Delta G_{\mathrm{fluctuator}}$ conductance fluctuation of the elementary volume including the fluctuator. Using the $\Delta R^2_{\mathrm{slice}} = \Delta G^2_{\mathrm{slice}}/G^4_{\mathrm{slice}}$ conversion between conductance and resistance fluctuations we can conclude in the $\Delta R^2_{\mathrm{PC}}/R^2_{\mathrm{PC}} = \Delta G^2_{\mathrm{PC}}/G^2_{\mathrm{PC}} = \Delta I^2_{\mathrm{PC}}/I^2_{\mathrm{PC}} = \Delta G^2_{\mathrm{fluctuator}} \cdot G^2_{\mathrm{PC}}/G^4_{\mathrm{slice}}$ relation. Note, that $\Delta G_{\mathrm{fluctuator}}$ does not depend on the junction diameter, whereas $G^2_{\mathrm{PC}} \sim d^2$ and $G^2_{\mathrm{slice}} \sim d^4$ relations hold, from which $\Delta G_{\mathrm{PC}}/G_{\mathrm{PC}} \sim d^{-3} \sim G^{-3}_{\mathrm{PC}}$ follows. This cubed dependence sufficiently well describes the steep conductance dependence of the relative noise in the studied Ta_2O_5 crosspoint devices at $G > 1\,G_0$ conductances, as demonstrated by the red guide to the eye line demonstrating a $\Delta I/I \sim G^{-3}$ relation in Fig. 4.12. This indicates, that the noise characteristics of the studied Ta_2O_5 crosspoint devices are dominated by the contribution of a single fluctuator at the bottleneck.

The above considerations imply that the increased contribution of a single fluctuator in the crosspoint devices could account for the distinct conductance dependencies of the relative steady-state noise when compared to the STM-PC devices. How the sample geometry and the oxide layer preparation impact the distribution of the fluctuator, is still an intriguing question. A detailed study on the statistical analysis of different sample designs could help to explain the substantial difference between the two devices, but this was not part of my research.

The noise map presents an excellent information source about the noise tuning range and limits of the characterized sample. To understand its merits, I used the results of Rao *et al.* [24] on HfO_2/Al_2O_3-based memristor as a reference, see the

11-bit multilevel programming in the conductance range of ~ 0.65 and ~ 53.5 G_0 in Fig. 2.5, as well as the denoising process and the 0.026 G_0 spacing between neighboring states in Fig. 4.3. I use the achievements of this study as a comparison basis for my noise measurements, considering $\Delta G_{\mathrm{ref}} = 0.026$ G_0 as a reference resolution. In Fig. 4.14, I compare this reference resolution to my noise data. Note that my current noise measurements were performed in the steady state, where the $\Delta I/I = \Delta G/G$ relation is satisfied. This means that my noise data directly represent the steady-state fluctuation of the conductance normalized to the conductance ($\Delta G/G$), which can be directly compared to the above reference resolution by normalizing the latter to the conductance as well, i.e., plotting the $\Delta G_{\mathrm{ref}}/G$ function, which is a line on the log-log plot (see black line). Compared to this reference conductance resolution the shaded areas illustrate other possible conductance resolutions with a factor of two (1 bit) resolution difference between the different shades. Note, that on the left axis ΔG represents the standard deviation of the conductance, but to achieve the ΔG_{ref} conductance resolution, rather the peak-to-peak noise should be below the resolution limit. Therefore, as a reasonable limit, the relative noise should satisfy $\Delta G < \Delta G_{\mathrm{ref}}/8$, i.e., to have a 3-bit better standard deviation of the noise as the envisioned reference resolution (see the black dashed line).

As a first conclusion of Fig. 4.14 it is to be stated, that at any given conductance the device-to-device variation of the relative steady-state noise level is rather high, reaching an order of magnitude difference between the various measurements. Despite that, even the noisiest devices satisfy the desired ΔG_{ref} conductance resolution at the high and low conductance ends of the investigated conductance regime, i.e., in these regimes all the relative noise values are below the reference black dashed line. In the middle of the conductance range, i.e., in the regime around 1 G_0, this is not satisfied anymore: a significant portion of the measurement points are above the black dashed line, but another significant portion still satisfies the desired resolution limit. This observation prompts the question of whether the noise level requires the choice of a proper device, or alternatively, the noise level of any arbitrary device can be pushed below the reference line by proper electrical treatment of the chosen device. The next section will provide insights into the answer based on the study of non-steady-state noise. Before discussing the results of the nonlinear noise spectroscopy studies, some important notes must be emphasized about Fig. 4.14. First, the above comparisons solely analyzed the relation to the reference resolution from the noise's point of view, i.e., it was not investigated, whether distinct conductance values with ΔG_{ref} conductance spacing can indeed be programmed in the studied devices. Second, the number of resolved bits is determined as $\log_2(G_{\mathrm{max}}/\Delta G_{\mathrm{ref}})$ ratio, where G_{max} is the top end of the programmable conductance range. In my study, the investigated conductances did not reach as high levels as in Ref. 24 (~ 53.5 G_0). This can be immensely improved by extending the upper conductance limit, which is indeed possible on this same sample design, as discussions revealed with Miklós Csontos, who fabricated the samples. During my measurements, such ambitions were not targeted due to the increased risk of device failure at too high conductance values.
An additional remark is that the evaluated ΔG standard deviation values depend

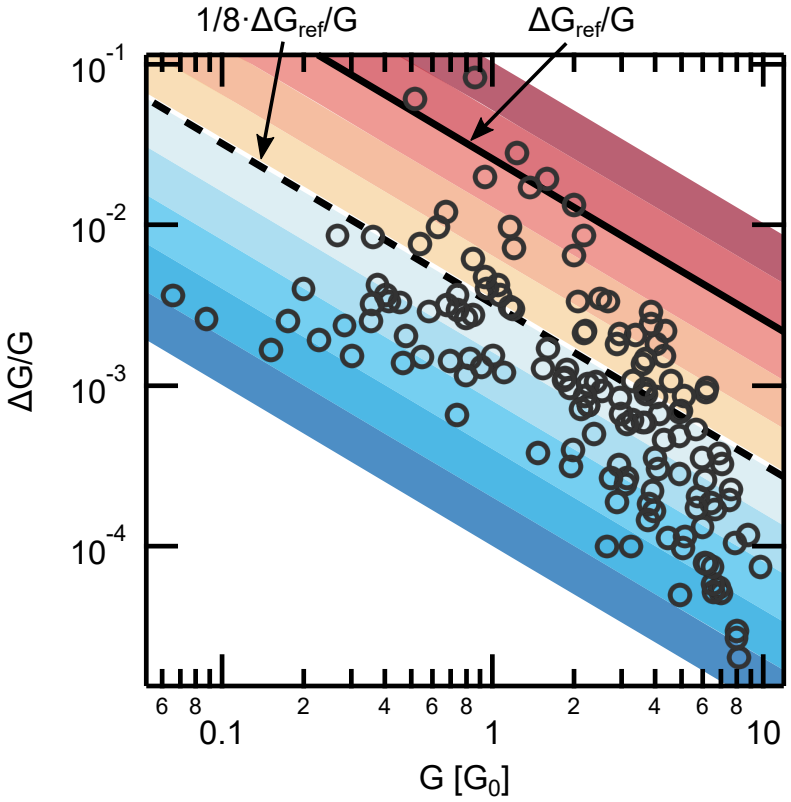

Figure 4.14: *Steady-state noise map with a black line indicating a comparison to the $\Delta G_{\mathrm{ref}} = 0.026\ G_0$ reference resolution. Each cold (warm) colored stripe illustrates an enhancement (deterioration) by an additional 1-bit resolution from the reference line. The dashed line represents $\Delta G_{\mathrm{ref}}/8$ reference resolution, which is compared to the standard deviation of the conductance fluctuations (ΔG on the left axis). All quantities are normalized to the G conductance. Results to be submitted in Ref. P3.*

on the f_1,f_2 frequency limits of the spectral density integral. As discussed in Section 4.2, this is a very weak dependence: orders of magnitude variations in the evaluation bandwidths only yield minor variations in the obtained ΔG values.

4.4.2 Nonlinear noise characteristics of Ta_2O_5-based memristors

Measurement of nonlinear noise

To determine the conductance of a memristive device, one can always find a read-out voltage, where the $I(V)$ curve is linear, and the voltage does not excite further fluctuations. This is the regime of linear noise spectroscopy, where steady-state fluctuations are investigated, as discussed in the previous part of this chapter. These steady-state fluctuations can also be considered as a base level for the read-out noise: no matter how precise instruments are used for the conductance read-out, the conductance resolution cannot be better than the steady-state noise. In this

chapter, I will go beyond steady-state noise measurements, demonstrating that noise benchmarking is possible all the way along the entire switching cycle. This work was initiated by the pioneering studies of Botond Sánta [62], who conducted voltage-dependent noise measurements of full-cycle memristive switchings in Ta_2O_5 STM point-contact devices. These early studies revealed exciting features (see Fig. 4.6) to be analyzed in more detail. I have adapted this measurement technique and optimized the measurement and evaluation protocols to perform voltage-dependent noise measurements on the Ta_2O_5 nanofabricated crosspoint devices which devices were already analyzed in the previous subsection.

First, I used nonlinear noise spectroscopy measurements to investigate memristive switching, focusing on cycle-to-cycle reproducibility. The steps of such measurement are illustrated in Fig. 4.15. The basis for every measurement is a stable and reproducible switching, which is confirmed by multiple current-voltage characteristics with the same LCS and HCS. Next, the noise measurement is designed to match the switching parameters: the device should undergo an equivalent switching with the only difference that the applied voltage signal is discretized to voltage plateaus. Due to the voltage-time dilemma, the continuous and the discretized voltage signals will only result in an equivalent switching if the applied amplitudes and time duration match. Fig. 4.15(a) depicts a continuous $I(V)$ characteristic (gray line) and the average current-voltage pairs at each voltage plateau for the subsequent noise measurements (red plus markers). The excellent agreement between these measurements shows that the discretized and the continuous voltage signal has an equivalent effect regarding memristive switching; therefore, these noise measurements can adequately characterize the switching dynamics. Note, that the small deviations between the results of the continuous $I(V)$ and the discretized noise measurements at the transition regime are normal, even reproducible continuous switching cycles exhibit some degree of cycle-to-cycle variation during the transitions. Additionally, the noise evaluation in the transition regimes must anyway be considered cautiously because the ongoing switching introduces a non-constant conductance at these plateaus.

Although high-speed memristive switching is possible and desirable, noise characterization has limitations in that area. The time duration for each noise measurement plateau determines the frequency resolution and the rank of averaging of the noise spectral density. Furthermore, the voltage plateaus have to be long enough to accommodate the low-pass filtering; the beginning of each plateau displaying the typical (dis)charge characteristics of the RC filter has to be removed, and the filter cut-off frequency will determine this (dis)charge time. See the analysis in Fig. 4.8 on the filtering of the noisy output of the Agilent. This compromises high-resolution noise spectra and reasonable switching times, leading to measurements with lengths in the order of $10 - 100$ s long switching cycles.

The upper inset of Fig. 4.15(a) shows a part of the measured current signal in the HCS, demonstrating a segment with three plateaus measured at subsequent drive voltages. The steps in the current signal exhibit the response to low-pass filtering. In this example, the middle plateau is evaluated, and the red color highlights the evaluated segment, where the transient due to the RC filtering is already negligible. The lower inset shows the corresponding noise spectrum and the black-colored base

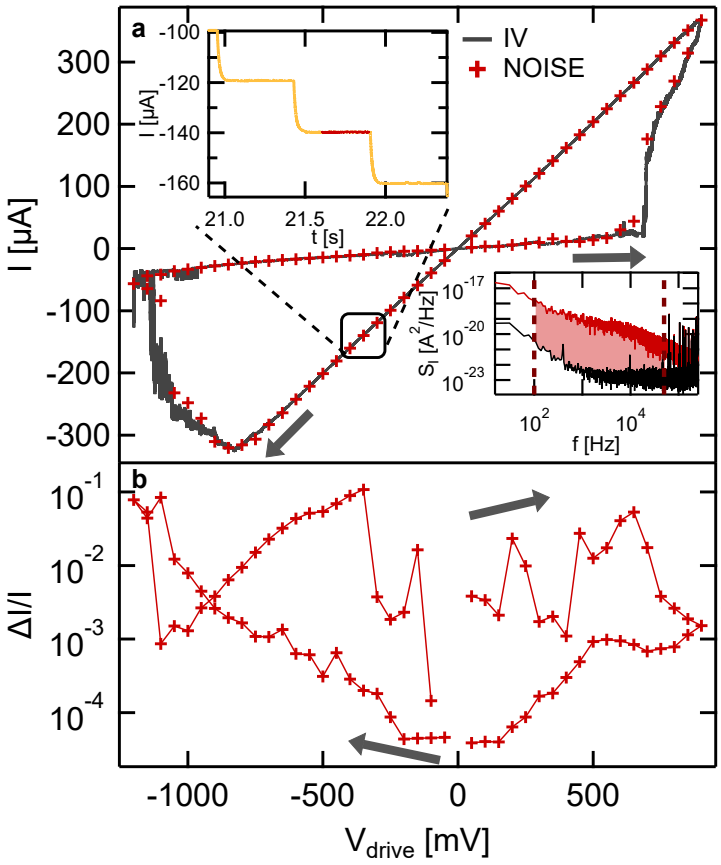

Figure 4.15: *Voltage-dependent noise measurement to investigate memristive switching. (a) Continuous current-voltage characteristics (gray line) and subsequent measurement with a discretized voltage sweep (red plus) yield the equivalent switching characteristics. The upper inset shows part of the measured current signal as a response to the step-wise voltage sweep in the HCS illustrating three plateaus. The lower inset depicts the noise spectral density calculated from the middle plateau highlighted with red color together with the black-colored base noise at zero bias. (b) Relative noise is calculated at all voltage plateaus from the integral of the excess noise between the predefined frequency limits denoted by the vertical dashed lines in the lower inset of (a).*

noise level measured at zero bias of the HCS, and integration limits are illustrated by vertical dashed lines. The relative noise is calculated at all voltage plateaus which is shown in panel (b). In the analysis of these results, I mainly focus on the voltage regimes anticipating the set and reset transitions, which consist of the positive voltage region of the LCS and the negative voltage region of the HCS, respectively. The overall trend follows two observations: (i) constant level low voltage relative noise corresponds to the expectation from the steady-state noise, (ii) there is an increase of relative noise before the switching, which is more convincing in the LCS, where the relative noise increases ~ 1 order of magnitude while the conductance

state is highly linear.

In order to investigate the cycle-to-cycle reproducibility of these observations, the full-cycle voltage-dependent noise measurement is repeated several times. I conducted several cycle-to-cycle reproducibility measurements, all showing similar trends to what is demonstrated here. Fig. 4.16 depicts one of these measurements. The applied discretized triangle drive voltage of the presented nonlinear noise measurements is shown in panel (a), with insets demonstrating the measured current (lower left) and the corresponding noise spectrum (upper right) at the plateau indicated with the blue circle, these are depicted similarly as presented in Fig. 4.15(a). Panels (b)-(c) present the results of 10 subsequent full-cycle noise measurements, the individual (gray) and mean (colored circles) current-voltage pairs in panel (b), and relative noise in panel (c). Due to the considerable cycle-to-cycle variation of relative noise, the average is evaluated on the logarithmic vertical scale, which is representative of the broad distribution of values not uncommonly spreading even over multiple orders of magnitude. It shows that while the $I(V)$ characteristics exhibit high reproducibility with little to no change in the conductance states, the relative noise curves vary greatly. Despite the variations, the averaged relative noise curve does unambiguously show multiple characteristic regimes: (i) steady-state regime at low voltages with voltage-independent relative noise levels, (ii) non-steady-state regime at slightly increased voltages still in the linear conduction regime of the current-voltage characteristics exhibiting a persistent increase of relative noise, and (iii) switching regime where the transition occurs. The color-coding of the corresponding data points for set/reset transitions is (i) red/blue, (ii) dark red/dark blue, and (iii) purple. The relative noise increase in the non-steady-state regimes (dark red and dark blue) is assumed to be attributed to voltage-induced mobilization of ionic motions around the active region, but this is not yet a switching, only a fluctuation with mostly unchanged mean conductance. In this sense the non-steady-state region is considered as a precursor regime: the increasing noise forecasts the proximity of the switching.

To put the noise data into perspective, panel (d) plots the average relative noise data (red, dark red, blue, dark blue and purple curve segments in Fig. 4.16(c)) on top of the steady-state noise map reproduced from Fig. 4.14 (gray circles). Again, the strong, order of magnitude device-to-device variation of the gray steady-state noise data is emphasized. Compared to that, the steady-state regime of the average voltage-dependent noise curve (red and blue circles) exhibits a smaller variation in both relative noise and conductance. The conductance of the LCS corresponds to an oxygen-saturated conducting filament with a transport deviating from metallic conduction and more prone to instabilities, which explains the broader variation in conductance. By definition, the non-steady-state regime is the voltage range, where the conductance is mostly unchanged, but the noise significantly deviates from the steady-state noise. As appropriate, the corresponding dark red and dark blue non-steady-state noise data are positioned above the steady-state noise data in panel (d). Finally, the noise data in the switching region (purple) do not grow above the device-to-device variation of the steady-state noise data, but the purple points are positioned around the largest possible steady-state noise values at the given $G = I/V_{\text{bias}}$ conductance of the actual point on the switching curve.

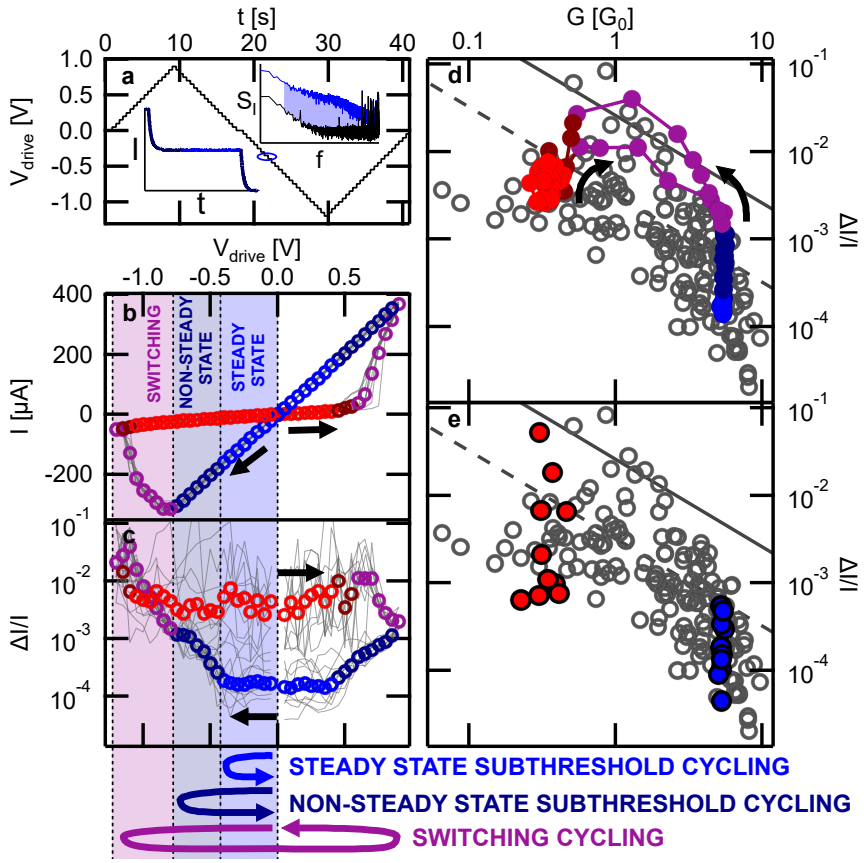

Figure 4.16: *Nonlinear noise measurements and cycle-to-cycle variation. (a) The applied discretized triangle drive voltage is used in the presented nonlinear noise measurements. The lower inset shows the low-pass filtered current signal at one plateau with a light blue color indicating the evaluated section. The upper inset presents the evaluated spectrum (light blue) and the corresponding base noise spectrum (black). The current noise is calculated as the integral of the excess noise between the frequency limits of 100 Hz and 50 kHz. (b-c) 10 subsequent nonlinear noise measurements (gray) exhibit highly reproducible conductance states in the current-voltage characteristics (b) but huge variations in the relative noise (c). The averaged current and relative noise values are plotted with circles color-coded based on the relevant dynamics: steady state (light blue and red), non-steady state (dark blue and dark red), and switching regime (purple). Based on the nonlinear noise measurements, I define cycling measurements illustrated by the arrows below involving the observed distinct regimes (see later in the text). (d) The mean relative noise of the switching cycle plotted on the steady-state noise map reveals the effective distinction of the defined regimes. (e) The steady-state relative noise at each -150 mV (150 mV) for HCSs (LCSs) plotted on the noise map shows commensurate cycle-to-cycle and device-to-device variation. Results to be submitted in Ref. P3.*

Fig. 4.16(d) analyzed the *average* noise characteristics compared to the device-to-device variation. In a device, however, not the cycle-to-cycle average noise, but the actual noise is important. Unfortunately, the individual full-cycle measurements (gray curves in Fig. 4.16(c)) are difficult to follow. For a better comparison, these curves and the corresponding conductance evolution are magnified in Fig. 4.17(a)-(b) to only show the most interesting segment, i.e., the negative voltage branch, where the reset transition happens. Each cycle is color-coded in the same fashion

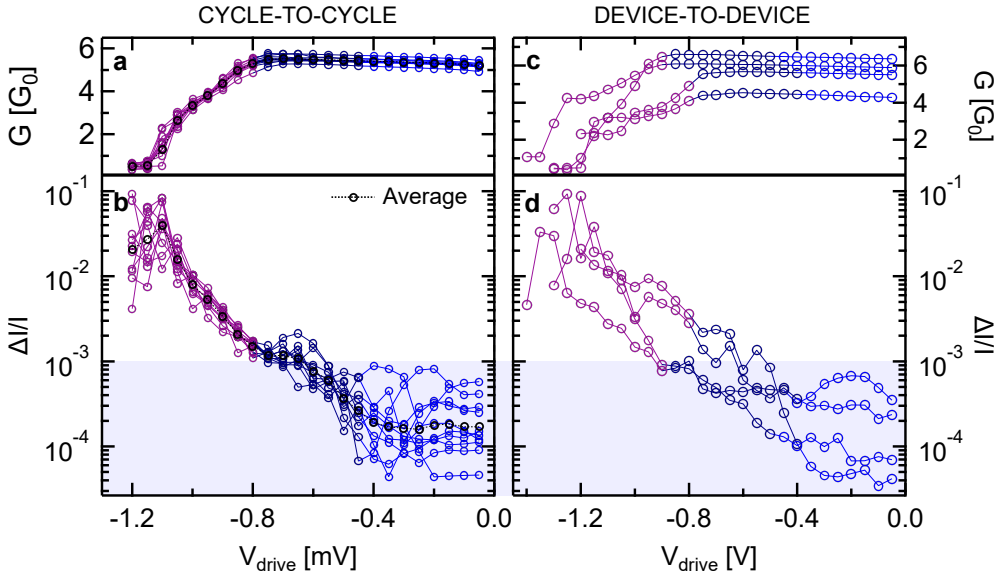

Figure 4.17: *(a-b) Zoom into the conductance (a) and relative noise (b) of the 10 subsequently measured cycles presented in Fig. 4.16(b)-(c), with attention to the HCS at negative polarity where the reset transition happens. The color-coding of the individual curves is consistent with the steady state (blue), non-steady state (dark blue) and switching (purple) distinction, while the average curve is black. (c-d) Same evaluation presented on the individual reset curves measured on 4 different devices, all exhibiting HCSs in the range of* $4.3 - 6.4\ G_0$*. The measurements are colored based on the same distinct color-coding for the relevant regimes.*

as explained in Fig. 4.16, i.e., the blue, dark blue, and purple regions demonstrate the steady-state, non-steady state, and switching conductance regions. Here, the average curve is indicated with black color. As a comparison, panels (c) and (d) demonstrate the reset branches for 4 measurements on 4 different devices (all exhibiting HCSs in the range of $4.3 - 6.4\ G_0$), using the same color coding.

Although in panels (a) and (b) there clearly is a cycle-to-cycle variation of the relative noise, the individual cycles follow a uniform trend consistent with the detailed evaluation above, exhibiting a similar decomposition to (i) a steady-state region (blue), where both the conductance and the relative noise are mostly constant; (ii) a non-steady-state region, where the conductance is constant but the noise increases a lot (dark blue) and (iii) the switching region (purple), where the conductance decreases while the noise further increases. These trends are also

similar on the representative curves taken on different devices with similar HCS conductance in panels (c)-(d). The blue steady-state regions, however, exhibit a remarkable feature. A rather high device-to-device variation of the steady-state noise was observed in Fig. 4.14, which is also obvious from the blue region of Fig. 4.17(d). But most surprisingly, the steady-state noise values of the highly reproducible resistive switching cycles (blue region in panel (b)) exhibit a similarly large variation as the huge device-to-device variation of the steady-state noise. This is also demonstrated by Fig. 4.16(e), where the blue and red points demonstrate the steady-state noise values of the 10 subsequent switching cycles of Fig. 4.16(b)-(c), as compared to the device-to-device variation of the steady-state noise values (gray circles). Again, it is clear, that the cycle-to-cycle variation of the steady-state noise values spans the same wide range as the device-to-device variation.

The previous observations mean, that the seemingly reproducible switching process yields the reconfiguration of the fluctuators along the switching, i.e., a completed switching cycle yields a very similar conductance to the previous cycle, but meanwhile the fluctuations of the active region completely change. This can cause even an order of magnitude decrease of the steady-state noise from one cycle to the other, but a similarly large increase as well, which can be interpreted by switching OFF or ON a highly dominant fluctuator along a resistive switching cycle. This cycle-to-cycle noise variation does not allow a deterministic denoising strategy, but by trial and error, along ~ 10 switching cycles one can find a device state for which the steady-state noise is close to the bottom end of the device-to-device variation's noise, i.e., the noise of the actual state is close to the smallest possible noise value for the given device pool, and accordingly the such-adjusted low-noise state is well applicable as a high-resolution synaptic weight in a neural network.

Note, that the denoising process of Ref. 24 followed a similar, and very successful trial and error strategy, but with considerably less insight into the underlying noise characteristics, i.e., the evolution of noise spectra was not investigated. In their work, they used a subthreshold denoising process, i.e., for denoising, the applied voltages were always smaller than the switching threshold: denoising was executed by positive-negative pulse pairs at 350 mV. This strategy is expected to offer a more precise tuning of the desired device state. Especially, for the demonstrated high-precision applications, it is important to preserve the conductance state with 11 bit resolution along the denoising process, for which the execution of a full switching cycles is less favourable than a more gentle subthreshold denoising.

In the following, I analyze the possibility of subthreshold denoising on the Ta_2O_5 crosspoint devices, following the voltage-cycling strategies illustrated at the bottom of Fig. 4.16. The bottom strategy (switching cycling) just illustrates the above-described scheme, where the steady-state noise of a device can be manipulated throughout repeated switching cycles. Alternatively, one can ramp up and down the applied voltage staying always below the switching threshold, and study, how the steady-state noise is manipulated by such *subthreshold cycling measurements*. By definition of the steady-state, no major variation of the noise properties is expected, if a *steady-state subthreshold cycling* is performed, i.e., if the applied voltage cycle does not exceed the steady-state region. A *non-steady-state subthreshold cycling* may already yield considerable noise variation, which may offer a possibility for

subthreshold denoising. These schemes are discussed in the following subsection by demonstrating a noise benchmarking protocol, which provides a comprehensive insight to the noise properties along the above cycling strategies.

Noise tuning by subthreshold cycling

It was demonstrated, that the non-steady-state region already yields a voltage-induced manipulation of the fluctuators (see the order-of-magnitude noise increase in Fig. 4.16(d)) while the average conductance is kept mostly constant. Inspired by the successful subthreshold denoising process in Ref. 24, I analyzed the variation of the steady-state noise with the following measurement protocol. First, a long read-out noise measurement is executed at $V_{\mathrm{read}} = -100\,\mathrm{mV}$, then the voltage is ramped up in a step-wise fashion to a level, that is still below the switching threshold, then the voltage is ramped down to zero step-wise, and finally, another noise measurement is performed at V_{read} (see the illustration of the staircase and subsequent low-bias signal in Fig. 4.18). The results of such measurements are summarized in Fig. 4.19(a)-(e). The horizontal axis shows the number of the

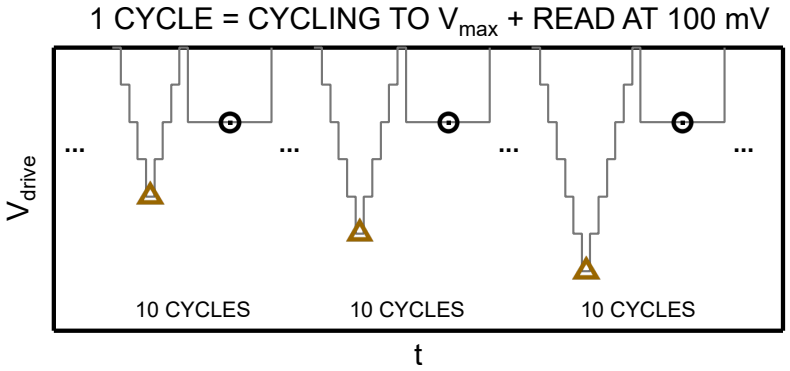

Figure 4.18: *The subthreshold cycling measurement scheme consists of repeated discretized cycling signals with gradually increasing maximal drive amplitude and subsequent low-voltage read-out plateaus. 500 ms long plateaus were found to be ideal for obtaining reasonably good-quality spectra with the ∼ 70 Hz cut-off-frequency RC filter. Each cycling is followed by a 5 s long steady-state measurement at $V_{\mathrm{read}} = -100\,mV$, which yields higher quality spectra due to better frequency resolution and higher averaging. Each cycling to V_{max} is repeated 10 times to observe the cycle-to-cycle variation and V_{max} is then increased by -50 mV towards the negative polarity. To be submitted in Ref. P3.*

executed cycling periods while panel (a) presents the V_{max} voltage reached along the given cycle. First, $V_{\mathrm{max}} = -100\,\mathrm{mV}$ is applied. Each cycling amplitude is repeated 10 times to observe the cycle-to-cycle variation at a given voltage and then V_{max} is increased by -50 mV towards the negative polarity. The choice of negative voltages is motivated by Fig. 4.16, where the subthreshold non-steady-state noise increase is the most pronounced at negative polarity. This schematic is repeated for 120 cycles in total reaching $V_{\mathrm{max}} = -650\,\mathrm{mV}$. This value relies on my experience

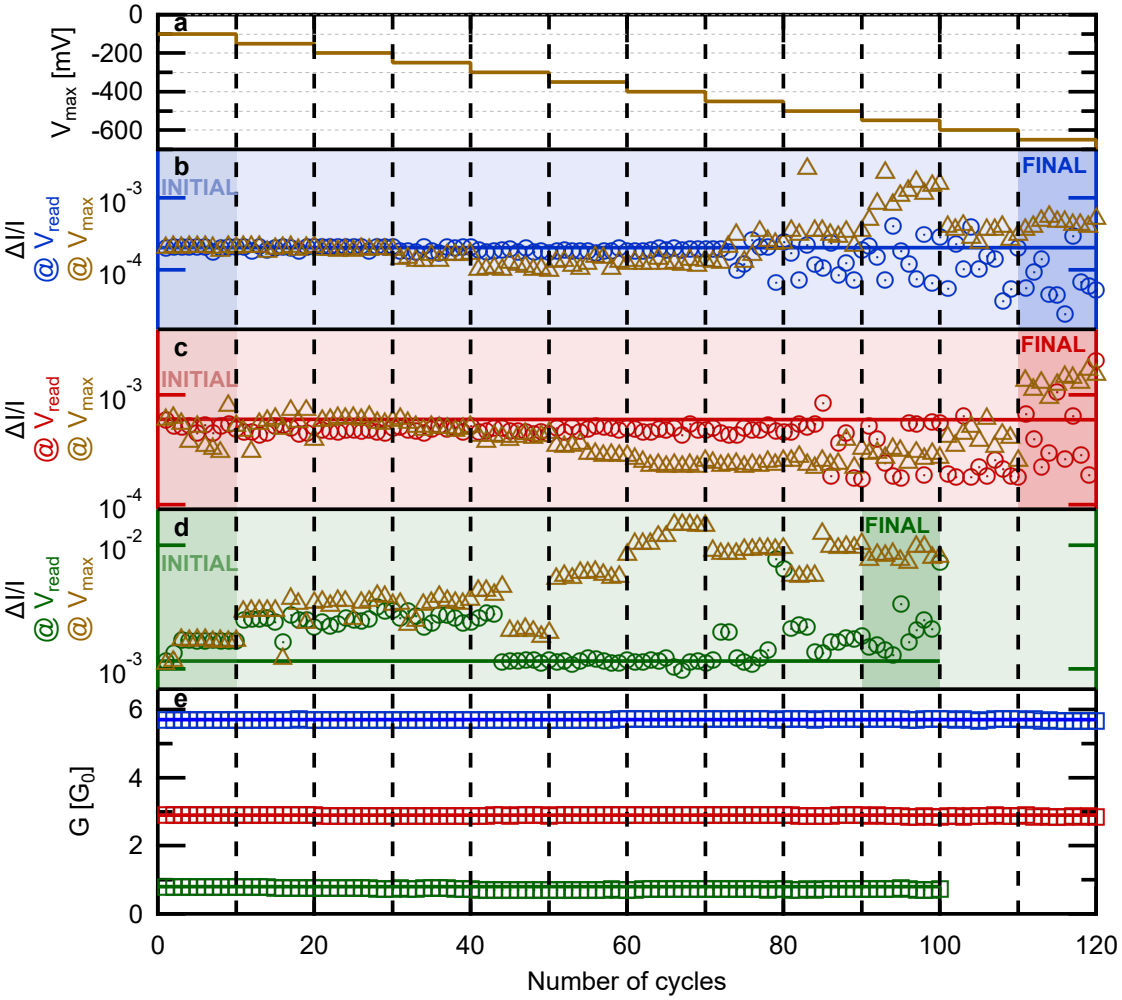

Figure 4.19: *Subthreshold cycling measurements focusing on the negative voltage regime preceding the reset transition. (a-e) Summary of the subthreshold cycling measurements, divided into segments with identical maximal amplitude of the applied cycling signal (a). The relative noise of the maximal amplitude plateau (gold triangle) and of the read-out plateau (colored dot-centered circles) after each cycling is analyzed for three different junctions in panels (b-d) with corresponding stable conductance (colored squares) in panel (e). Results to be submitted in Ref. P3.*

on a large amount of junctions, representing a voltage level, where the switching threshold is not yet reached, i.e., the steady-state conductance is unchanged, but the steady-state regime is well exceeded. Eventually, only the part exhibiting stable conductance is included in the analysis. Practically, this means that cyclings leading to a $> 10\%$ change in the conductance are excluded which was the case for the measurement of panel (d), where the cyclings with maximal amplitudes above $V_{\max} = -550\,\mathrm{mV}$ resulted in the increasing change of the conductance. It is to be noted, that a measurement program implementing the real-time monitoring of the conductance and the relative noise would allow an adaptive stopping of the voltage

sweep right before the onset of the switching process, but such a development was not in the scope of my work.

Such cycling periods are presented on three different junctions (panels (b)-(d)), well representing the entire conductance region of the usual measurements. The experiments yield two useful quantities for further evaluation. (i) The steady-state relative noise level after a certain cycling period is evaluated along the V_{read} read-out plateau (read-out noise demonstrated by colored circles with dots in the middle in panels (b)-(d)); (ii) the relative noise is also evaluated at each voltage plateau of the cycling, and the highest voltage (V_{max}) is used in this analysis, as demonstrated by the gold triangles on panels (b)-(d). As a reference, the conductance is also evaluated after each cycle at V_{read} as demonstrated by the colored squares in panel (e) using the same colors for the various junctions as in the noise data in panels (b)-(d). The initial steady-state relative noise and conductance values are indicated by solid horizontal colored lines to emphasize any relative change.

First of all, it is to be stated, that the conductance (panel (e)) is extremely stable along all these subthreshold voltage cycles. The noise measured at V_{max} (triangles) is not necessarily monotonic, but a general increasing trend is identified in accordance with the non-steady-state noise region in Fig. 4.16. This is attributed to the tendency, that a non-steady-state voltage is likely to excite further fluctuators compared to the steady state, but sometimes it is also possible that the applied voltage pushes a certain fluctuator to a state, where it stops fluctuating, or alternatively, it modifies its fluctuation frequency, which also alters the integrated current fluctuation. Later, Fig. 4.22 will present a detailed example of such voltage-induced tuning of a dominant fluctuator that can lead to an initial decrease of noise at V_{max} before the increase takes place.

The read-out noise (colored circles) is mostly constant until $V_{\mathrm{max}} = -450$ mV or $V_{\mathrm{max}} = -500$ mV voltage amplitudes, which is apparent in panels (b) and (c), respectively corresponding to junctions with 5.7 G_0 and 2.9 G_0 conductances. At even higher V_{max}, the read-out noise values do not show a general increasing tendency, but rather a stochastic variation between the subsequent subthreshold cycles is observed, such that the actual noise values can even be significantly smaller than the initial read-out noise. The results in panel (d) are obtained at a lower conductance of 0.8 G_0 (green), where the device is less stable than at the above higher conductances. Around the quantum conductance unit, the smallest rearrangements in the conductive filament strongly influence the overall conductance and the steady-state read-out noise, which is evidently the case here. Such instabilities hinder the evident identification of the steady-state and non-steady-state regimes. Nonetheless, the results do suggest an onset of the non-steady state at -400/-450 mV with a considerably increased maximal amplitude noise relative to the initial values and, more apparently, an increased cycle-to-cycle variation of the read-out noise.

The results of panels (b)-(d) can also be summarized in comparison to my reference figure on the device-to-device steady-state noise variation (gray circles in Fig. 4.20). In the same figure, the light blue, light red, and light green horizontal lines enclose the regions, where the read-out noise values scatter for the initial 10 cycles in panels (b)-(d), i.e., for the measurements with $V_{\mathrm{max}} = -100\,\mathrm{mV}$. These

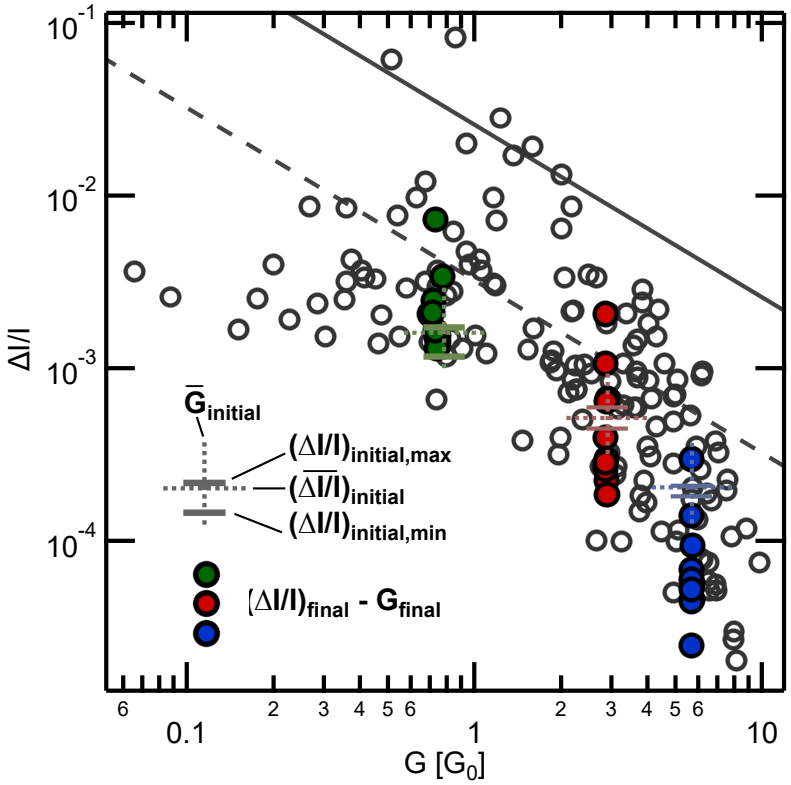

Figure 4.20: *Initial levels and final read-out noise values of the presented subthreshold cycling measurements of Fig. 4.19 panels (b), (c) and (d) compared to the steady-state noise map (gray circles), with the respective colors, blue, red and green. The lightly colored horizontal solid lines indicate the minimum and maximum of read-out relative noise values in the initial 10 cycles with the* $V_{\max} = -100\,mV$*. The horizontal and vertical dashed lines show the average read-out noise and average read-out conductance, respectively. The read-out noise of the final 10 cycles (*$V_{\max} = -650$ *mV,* -650 *mV,* -550 *mV in Fig. 4.19 panels (b), (c), (d)) are presented with individual blue, red and green circles. Results to be submitted in Ref. P3.*

noise values span a significantly narrower noise interval than the device-to-device variation represented by the gray circles. This means that the low voltage cycling keeps the device's noise mostly stable. As a sharp contrast, the blue, red, and green circles in panel (g) exhibit the read-out noise values during the final 10 cycles in panels (b)-(d), where the $V_{\max}$ voltage amplitudes reach the maximal values in the non-steady-state regime. These noise values span a similar noise interval as the device-to-device variation at the same conductance.

Next, I present a selection of subthreshold cycling measurements to investigate the reproducibility beyond the results discussed in Fig. 4.19. I conducted a total of 41 subthreshold cycling measurements on 2 devices, and Fig. 4.21 presents 6 representative ones at various conductances indicated by different colors. Each dataset in panel (a) includes the 10 individual relative noise values of the $|V_{\text{read}}| =$ 100 mV read-out after every cycling at each $V_{\max}$ maximal amplitude, which are

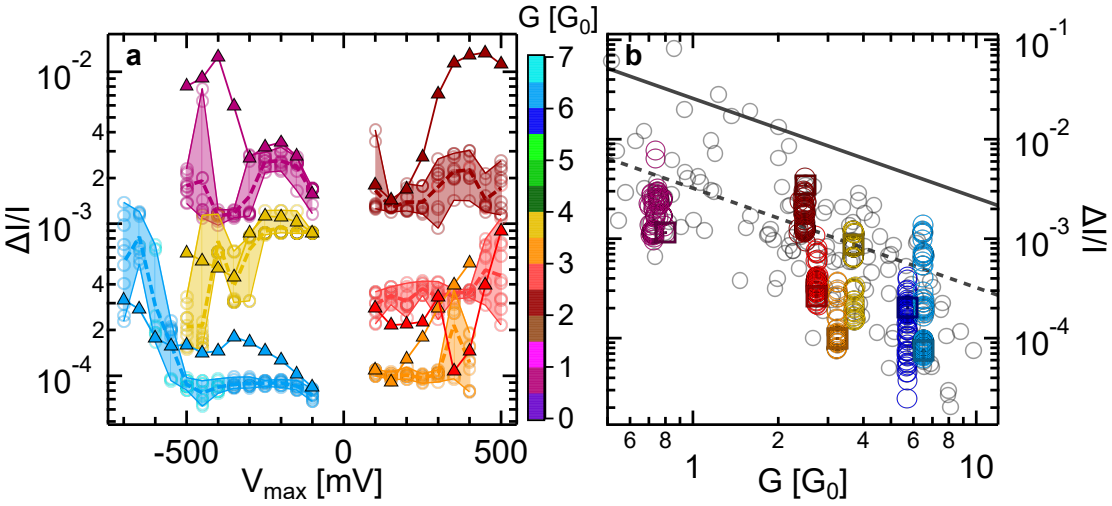

Figure 4.21: *The summary of 6 representative subthreshold cycling measurements colored based on their conductance. (a) Relative noise evolution at the maximal amplitude plateau (triangles) and the read-out plateaus (circles) as a function of the applied maximal cycling amplitude. A shaded area connects the minimal to the maximal relative noise values, and the mean value is plotted with a dashed line. (b) All steady-state read-out relative noise data points from panel (a) are plotted on the steady-state noise map to compare the cycle-to-cycle variation. Darker toned squares indicate the first read-out value.*

plotted with individual circles. The shaded area highlights the range of the 10 read-out noise values at each V_{max} amplitude, as it ranges from the minimal to the maximal relative noise. The dashed lines indicate the mean of these read-out relative noise values. Finally, the triangles indicate the mean relative noise of the maximal amplitude plateaus (average relative noise of 10 V_{max} plateaus). The measurements are analyzed up to the maximal cycling amplitude, where the conductance is still linear and stable, similar to the analysis of Fig. 4.19(b)-(d). The higher conductances ($\gtrsim$ 3 G_0) show the expected narrow distribution of steady-state noise at lower voltage and an evident increase of variation as soon as the non-steady state is reached. In comparison, lower conductances might exhibit a higher initial variation, similarly to the 0.9 G_0 dataset of Fig. 4.19(d). Meanwhile, the evolution of the maximal amplitude noise follows similar trends at all conductances: at intermediate maximal amplitudes, each measurement shows a unique voltage dependence, which is then clearly overshadowed by a sharp increase at the highest V_{max} amplitudes. These effects were already observed in the previous measurements, and the former phenomenon of the unique voltage dependence will be elaborated on in the next figure (Fig. 4.22). Note that the datasets cycled to positive voltages typically reach lower voltages before nonlinearities and switching effects are triggered. This can also shorten the non-steady-state regime.

The steady-state read-out noise results are compared to the device-to-device variation given by the steady-state noise map on Fig. 4.21(b). The measurements plotted include all the same datasets from panel (a) with attention to the read-out

noise (colored circles) measured after each cycling for all V_{max} maximal amplitudes on top of the steady-state noise values (gray circles) of the noise map. The initial noise state, the first read-out value, is indicated by a darker-toned square. This comparison verifies that the conductance variation during the cycling measurements is negligible. Additionally, it demonstrates that the noise map provides the frames of available relative noise range, and the initial noise state sets the probable direction to walk the map, e.g., a significant noise reduction is only possible from a high-noise initial state, see dark red, yellow and dark blue measurements. Note that for some measurements, the subthreshold cycling meant the implementation of noise reduction below the ΔG_{ref} conductance resolution (gray dashed line), see dark red and yellow data. This analysis again confirms that the noise map is indeed a versatile tool to benchmark multilevel programming applications in revealing the limits of noise tuning.

The previous figures provided detailed information about the voltage dependence of the relative noise, which, however, did not include the full information content of the executed noise measurements. In Fig. 4.22, I go beyond the investigation of the integrated relative noise values ($\Delta I/I$). Instead, I pick an example of three subsequent subthreshold cycling periods, on which I demonstrate the evolution of the full frequency-dependent noise spectra as the voltage is varied. Panels (a), (b), and (c) demonstrate the evolution of the noise as the voltage is ramped up and down (colored circles), and (a1)-(a5),(b1)-(b5), and (c1)-(c5) depict noise spectra at selected V_{drive} amplitudes indicated on the right side. Similarly as introduced earlier in Fig. 4.18, first, a noise measurement is performed at a voltage plateau with $V = 100\,\mathrm{mV}$, then the voltage is increased in $50\,\mathrm{mV}$ steps up to a maximal value of $V = 450\,\mathrm{mV}$. Afterwards, a similar step-wise ramp is performed in the downward direction, and finally, this procedure is repeated. The relative noise values in panels (a)-(c) and the related noise spectra below are colored in darker (lighter) tones corresponding to the upward (downward) sweep. Each noise spectrum is fitted by the sum of a 1/f-like spectrum (ensemble of more remote fluctuators) and a single Lorentzian (a single dominant fluctuator positioned close to the device bottleneck), as it was already discussed in Figs. 4.2 and 4.9. The decomposed fitted spectra are also integrated, and the $\Delta I/I$ values are evaluated separately for the 1/f-type part ($(\Delta I/I)_{1/f}$) and the Lorentzian part ($(\Delta I/I)_{\mathrm{Lor}}$). In panels (a)-(c), the decomposition is illustrated by the empty circle corresponding to $(\Delta I/I)_{\mathrm{Lor}}$, and the total relative noise $(\Delta I/I)_{\mathrm{total}} = \sqrt{(\Delta I/I)^2_{\mathrm{Lor}} + (\Delta I/I)^2_{1/f}}$.

The relative noise in the upward ramp of the first sweep (panel (a)) exhibits an unconventional, non-monotonic voltage dependence at intermediate voltages and an obvious increase at the highest voltages. Initially, the steady-state noise has a significant contribution from a single fluctuator whose amplitude is decreased and relaxation time is detuned by the applied voltage, see the Lorentzian spectra shifting to a higher cut-off frequency (vertical dashed lines) and eventually out of the integration window (panels (a1)-(a5)). The non-monotonic voltage dependence is nicely reproduced in the downward ramp, i.e., the noise spectra reproduce at the same drive voltages and the corresponding decomposition to 1/f-like and Lorentzian spectra yield nearly identical proportions. However, this reproducible behavior is not observed in the next sweep (orange colors). Although the upward

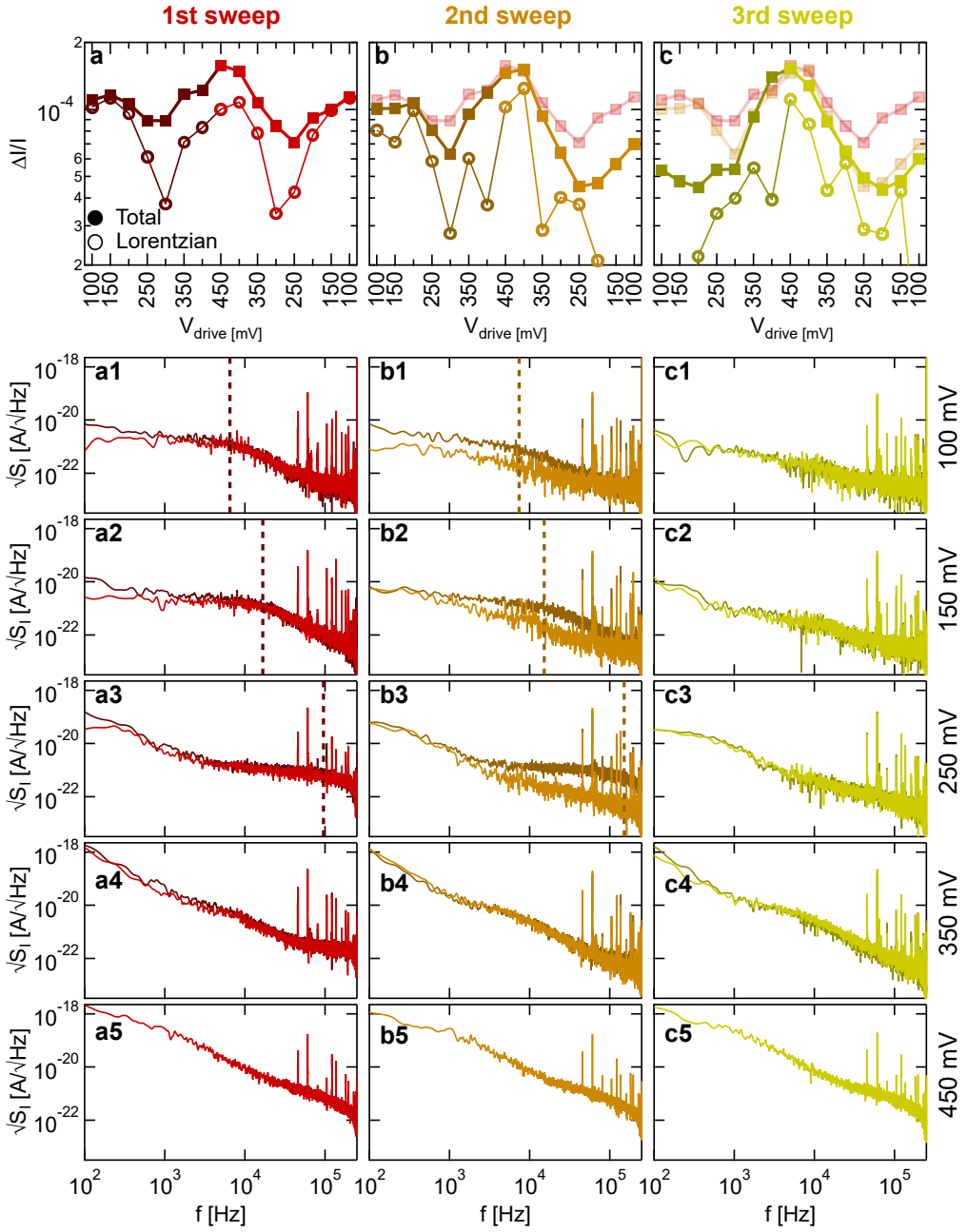

Figure 4.22: *Extended analysis of three subsequent non-steady-state cyclings (red, orange, yellow) leading to noise reduction. (a-c) Voltage dependence of the total relative noise* $(\Delta I/I)_{\mathrm{total}} = \sqrt{(\Delta I/I)^2_{\mathrm{Lor}} + (\Delta I/I)^2_{1/f}}$ *(squares) and the contribution of the Lorentzian component* $(\Delta I/I)_{\mathrm{Lor}}$ *(circles) during the upward (dark tones) and the downward (light tones) ramp. Faint colored squares show the voltage evolution in the previous sweeps. (a1-c5) Noise spectra at selected drive voltages (label on the right) are plotted underneath the corresponding sweep with the same color coding for the downward/upward direction.*

ramp exhibits a similar voltage dependence to the first sweep (see the faint red curve in the background of panel (b)), i.e., the non-monotonic voltage dependence and Lorentzian spectra shifting to higher cut-off frequencies, the downward ramp exhibits a fundamentally changed voltage dependence, and the strong suppression of the Lorentzian noise $(\Delta I/I)_{\mathrm{Lor}}$. Consequently, the final noise at 100 mV is significantly smaller than the initial noise at the same voltage. The differences are further highlighted by the individual spectra in panels (b1)-(b2), which reveals the disappearance of the Lorentzian spectrum, thus the noise spectrum is dominated by the 1/f-like spectrum from the ensemble of remote fluctuators. This behavior is indicative of non-steady-state cycling, where the applied voltages are capable of causing an irreversible change in the steady-state noise with unchanged steady-state conductance (not shown here). Note that a single non-steady-state cycling does not necessarily induce a change, but multiple cyclings might be needed. After the voltage-induced detuning of the single fluctuator, the emerging state is usually stable for subsequent cycling with the same $V_{\mathrm{max}} = 450$ mV maximal amplitudes. The third sweep in panel (c) (yellow colors) demonstrates the rather conventional nearly monotonic voltage dependence of the relative noise, and the noise spectra observed in the upward and downward sweeps (panels (c1)-(c5)) reproduce.

These results suggest that dominant fluctuators play a crucial role during noise tuning and are partly responsible for the huge cycle-to-cycle variation. Furthermore, these results somewhat refine the voltage regions, we observed in Fig. 4.19. The results can serve as an explanation for panel (c) where the voltage dependence of the V_{max} maximal amplitude noise (triangles) exhibits a decrease at intermediate voltages preceding the characteristic noise increase typical for the non-steady state. The analysis of the voltage-dependent noise with decomposition to Lorentzian and $1/f$-type spectra in Fig. 4.22 demonstrates that such non-monotonic voltage dependence is attributed to the voltage-induced detuning of an individual fluctuator.

4.4.3 Conclusions

During my research, I started investigating Ta_2O_5-based crosspoint devices motivated by intriguing noise results observed on Ta_2O_5-based STM point-contacts in our research group which was not yet explored fully. The material choice is specifically advantageous due to the stable operation and linear current-voltage characteristics ideal for voltage-dependent noise studies. First, I performed an extensive noise study of the conductance-dependent steady-state noise, yielding a wide-range noise map. The map shows huge device-to-device variation and distinct scaling at conductance lower or higher than $1 - 2\ G_0$, corresponding to a shift in the conduction mechanism. I found substantially different conductance scaling compared to the earlier measurements on Ta_2O_5-based STM point-contacts which I explained with the role of the increased contribution of a single fluctuator. I showed the use of the noise map as a robust benchmark of the investigated system for the noise-limited resolution of multilevel programming, which I demonstrated with comparison reference given by the work of Rao *et al.* [24].

In addition to the huge device-to-device variation, I studied the cycle-to-cycle evolution of noise using voltage-dependent measurements, enabling the investigation

of noise during the whole memristive switching. My measurements revealed a considerable cycle-to-cycle variation in the steady-state noise observed during highly reproducible switching, which was in the order of the device-to-device variation discovered in the noise map. Furthermore, I observed a precursor effect in the non-steady state before the transitions with the order-of-magnitude increase in the noise at mostly unchanged conductance.

Based on the conclusions of the cycle-to-cycle measurements, I proposed a subthreshold denoising process consisting of steady-state and non-steady-state cyclings. I studied the influence of increasing amplitude subthreshold cyclings on noise. I performed a large number of experiments in order to describe the noise tuning possibilities. On the one hand, the results reproduced the steep noise increase in the non-steady state (precursor effect). On the other hand, they revealed an increasing steady-state cycle-to-cycle variation appearing parallel to the onset of the precursor effect. I also demonstrated the assumed microscopic effect of the significant steady-state noise reduction observed during a non-steady-state cycling, i.e., the voltage-induced detuning of a single dominant fluctuator.

Chapter 5

Thesis Statements

I **I performed the extended statistical analysis of pure Ag atomic switches, obtained consistent theoretical results based on a proposed vibrational pumping model, and demonstrated the fundamental differences compared to an AgI-based electrochemical-metallization-type system [P1].** I performed measurements investigating pure Ag atomic switches at cryogenic temperature in a notched-wire mechanically controllable break-junction setup to ensure high purity in the metallic wire, enabling the investigation of the inherent properties of pure atomic switching. I used measurements on electrochemical metallization cells for a detailed comparison of switching characteristics, particularly to explore the cycle-to-cycle stochasticity and the weaker sweep rate dependence of pure atomic switching. I demonstrated that the simple theoretical approach relying on the voltage-induced pumping of a single vibrational mode provides a consistent model of the experimental observations, i.e., quantitatively describes the stochastic cycle-to-cycle variation and the weak frequency dependence of the switching threshold voltage.

II **I optimized a non-oxidizing fabrication method for nanofabricated break-junctions and subsequently, performed successful characterization measurements on Ag samples [P2].** I implemented and optimized a preparation method for realizing nanofabricated mechanically controllable break-junctions of oxygen-sensitive metallic electrodes. I fabricated several Ag samples, which metal has not been reported as nanofabricated break-junction in literature before. I performed thorough testing and characterization measurements under vacuum conditions at room temperature. The repeated breaking of the break-junction demonstrate clear plateaus with 1 G_0 conductance characteristic for the single-atom Ag junction. The samples exhibit excellent stability observed in the mechanically most sensitive tunneling regime. Finally, I showed a proof-of-principle application, I observed pure atomic switching at room temperature.

III **I explored the steady-state noise map of Ta_2O_5 crosspoint devices and investigated the full-cycle switching dynamics which revealed huge device-to-device and cycle-to-cycle variations in the steady-state noise and a precursor effect in the non-steady state, then based on these findings, I proposed a subthreshold denoising strategy [P3].**
I characterized the steady-state noise of Ta_2O_5-based crosspoint samples in a wide conductance range which features a huge device-to-device variation. Furthermore, the noise map exhibits differences to earlier Ta_2O_5-based scanning tunneling microscopy point-contact measurements which I attribute to the enhanced role of single dominant fluctuators in the crosspoint system. I demonstrated the relevant connection between the obtained steady-state noise map and the resolution limit for multilevel programming applications. Next, I thoroughly investigated the switching dynamics by full-cycle noise measurements, revealing a large cycle-to-cycle steady-state noise variation and a precursor effect in the non-steady state anticipating the transition. To exploit the relative noise variations in the non-steady-state, I proposed a subthreshold cycling strategy for denoising and demonstrated its potential in targeted noise tuning applications.

Acronyms

AI	Artificial Intelligence
DAQ	Data Acquisition Card
ECM	Electrochemical Metallization
ESD	Electrostatic Discharge
HCS	High Conducting State
LCS	Low Conducting State
MCBJ	Mechanically Controllable break-junction
RTN	Random Telegraph Noise
STM-BJ	Scanning Tunneling Microscopy Break-junction
STM-PC	Scanning Tunneling Microscopy Point Contact
VCM	Valence Change Memory

Acknowledgements

I want to acknowledge all the help and motivation I received from my colleagues, friends, and family. This thesis would not have been possible without the valued contributions from all of them.

First of all, I am especially grateful to my supervisor, András Halbritter, who inspired me to start my Ph.D. research and provided me with his high level of knowledge and patient guidance along the way.

The participation in noise measurements and the mentoring I received from Zoltán Balogh helped me through some of the more difficult times, and I truly appreciated our - sometimes lengthy - discussions.

I suppose Botond Sánta had the hardest part in supporting me through this research. He mentored me in the first years of my Ph.D., shared his valuable technical knowledge with me about memristors and noise measurements, and meanwhile, was the most loving, patient, and encouraging husband I could have. I am eternally grateful for all the love, motivation, and knowledge I received from him. I could not have run this marathon without you cheering along the way.

I very much appreciated the opportunity to work with Miklós Csontos at Empa and ETH Zürich during the development of a non-oxidizing fabrication method for nanofabricated break-junctions.

I am thankful to Máté Vigh for his insights and the plenty of helpful discussions about the vibrational pumping model.

I am thankful to László Pósa who worked with me on the electron beam lithography of the nanofabricated Ag samples.

I learned a lot from working with students, I am especially grateful to György Lázár and his evaluation codes that helped me dig through the immense amount of noise data necessary for my analysis.

I am grateful to my fellow students, who made my day-to-day life at the university more enjoyable. Gréta Mezei was always available for a good discussion about mental health and any important problems I faced, and I am also thankful for all the delicious pastry. I look back on our lunches with Gréta Mezei, Dániel Molnár, and Sebastian Schmid in a nostalgic mood and miss all our nice "Kaffeepausche" discussions about work, life, and of course, tomatoes and salty coffee.

I am thankful to Tímea Török for encouraging me as the deadline approached, and her assistance in printing and submitting this thesis.

I am particularly grateful to László Forró and Bence Márkus for giving me the space and resources to finish this thesis in the comfort of the Stavropoulos Center at the University of Notre Dame.

Last but not least, I cannot thank my family and friends enough, they have always stood by me and supported me unconditionally throughout my life. I especially thank my parents and my sister, Veronika, for providing me with an encouraging and loving home and helping me to become a physicist. My beloved nephew, Hunor, thank you for the smiles.

Publications related to the Thesis Statements

[P1] A. Nyáry, Z. Balogh, M. Vigh, B. Sánta, L. Pósa, and A. Halbritter, "Voltage-time dilemma and stochastic threshold-voltage variation in pure-silver atomic switches", Physical Review Applied **21**, 014027 (2024).

[P2] A. Nyáry, A. Gubicza, J. Overbeck, L. Pósa, P. Makk, M. Calame, A. Halbritter, and M. Csontos, "A non-oxidizing fabrication method for lithographic break junctions of sensitive metals", Nanoscale Advances **2**, 3829–3833 (2020).

[P3] A. Nyáry, Z. Balogh, B. Sánta, G. Lázár, N. J. Olalla, J. Leuthold, and M. Csontos, "Benchmarking stochasticity behind reproducibility: denoising strategies in Ta2O5 memristors", To be submitted (2024).

Other publications

[O1] A. Magyarkuti, K. P. Lauritzen, Z. Balogh, A. Nyáry, G. Mészáros, P. Makk, G. C. Solomon, and A. Halbritter, "Temporal correlations and structural memory effects in break junction measurements", The Journal of Chemical Physics **146**, 092319 (2017).

Bibliography

[1] D. Silver, A. Huang, C. J. Maddison, A. Guez, L. Sifre, G. van den Driessche, J. Schrittwieser, I. Antonoglou, V. Panneershelvam, M. Lanctot, S. Dieleman, D. Grewe, J. Nham, N. Kalchbrenner, I. Sutskever, T. Lillicrap, M. Leach, K. Kavukcuoglu, T. Graepel, and D. Hassabis, "Mastering the game of Go with deep neural networks and tree search", Nature **529**, 484–489 (2016).

[2] D. B. Strukov, G. S. Snider, D. R. Stewart, and R. S. Williams, "The missing memristor found", Nature **453**, 80–83 (2008).

[3] L. Chua, "Memristor-The missing circuit element", IEEE Transactions on Circuit Theory **18**, 507–519 (1971).

[4] F. Zahoor, T. Z. Azni Zulkifli, and F. A. Khanday, "Resistive Random Access Memory (RRAM): an Overview of Materials, Switching Mechanism, Performance, Multilevel Cell (mlc) Storage, Modeling, and Applications", Nanoscale Research Letters **15**, 90 (2020).

[5] *International Roadmap for Devices and Systems (IRDS) 2022 Edition*, `https://irds.ieee.org/editions/2022`.

[6] R. Waser, R. Dittmann, C. Staikov, and K. Szot, "Redox-based resistive switching memories nanoionic mechanisms, prospects, and challenges", Advanced Materials **21**, 2632–2663 (2009).

[7] J. J. Yang, D. B. Strukov, and D. R. Stewart, "Memristive devices for computing", Nature Nanotechnology **8**, 13–24 (2013).

[8] B. Mohammad, M. A. Jaoude, V. Kumar, D. M. Al Homouz, H. A. Nahla, M. Al-Qutayri, and N. Christoforou, "State of the art of metal oxide memristor devices", Nanotechnology Reviews **5**, 311–329 (2016).

[9] M. Le Gallo and A. Sebastian, "An overview of phase-change memory device physics", Journal of Physics D: Applied Physics **53**, 213002 (2020).

[10] S. Lequeux, J. Sampaio, V. Cros, K. Yakushiji, A. Fukushima, R. Matsumoto, H. Kubota, S. Yuasa, and J. Grollier, "A magnetic synapse: multilevel spin-torque memristor with perpendicular anisotropy", Scientific Reports **6**, 31510 (2016).

[11] S. Jan van der Molen and P. Liljeroth, "Charge transport through molecular switches", Journal of Physics: Condensed Matter **22**, 133001 (2010).

[12] H. Jeong and L. Shi, "Memristor devices for neural networks", Journal of Physics D: Applied Physics **52**, 023003 (2019).

[13] I. Valov, R. Waser, J. R. Jameson, and M. N. Kozicki, "Electrochemical metallization memories—fundamentals, applications, prospects", Nanotechnology **22**, 254003 (2011).

[14] S. Munjal and N. Khare, "Valence Change Bipolar Resistive Switching Accompanied With Magnetization Switching in CoFe2O4 Thin Film", Scientific Reports **7**, 12427 (2017).

[15] A. Geresdi, A. Halbritter, A. Gyenis, P. Makk, and G. Mihály, "From stochastic single atomic switch to nanoscale resistive memory device", Nanoscale **3**, 1504 (2011).

[16] B. Sánta, D. Molnár, P. Haiber, A. Gubicza, E. Szilágyi, Z. Zolnai, A. Halbritter, and M. Csontos, "Nanosecond resistive switching in Ag/AgI/PtIr nanojunctions", Beilstein Journal of Nanotechnology **11**, 92–100 (2020).

[17] A. C. Torrezan, J. P. Strachan, G. Medeiros-Ribeiro, and R. S. Williams, "Sub-nanosecond switching of a tantalum oxide memristor", Nanotechnology **22**, 485203 (2011).

[18] M. von Witzleben, T. Hennen, A. Kindsmüller, S. Menzel, R. Waser, and U. Böttger, "Study of the SET switching event of VCM-based memories on a picosecond timescale", Journal of Applied Physics **127**, 204501 (2020).

[19] M. von Witzleben, S. Wiefels, A. Kindsmüller, P. Stasner, F. Berg, F. Cüppers, S. Hoffmann-Eifert, R. Waser, S. Menzel, and U. Böttger, "Intrinsic RESET Speed Limit of Valence Change Memories", ACS Applied Electronic Materials **3**, 5563–5572 (2021).

[20] M. Csontos, Y. Horst, N. J. Olalla, U. Koch, I. Shorubalko, A. Halbritter, and J. Leuthold, "Picosecond Time-Scale Resistive Switching Monitored in Real-Time", Advanced Electronic Materials **9**, 2201104 (2023).

[21] D. Sanjay Khone, S. Bera, and A. Singh Rana, "Investigations of endurance and retention in tantalum oxide based memristor", Materials Today: Proceedings, `10.1016/j.matpr.2023.03.238` (2023).

[22] Y. Xiao, B. Jiang, Z. Zhang, S. Ke, Y. Jin, X. Wen, and C. Ye, "A review of memristor: material and structure design, device performance, applications and prospects", Science and Technology of Advanced Materials **24**, 2162323 (2023).

[23] B. Chen, H. Yang, B. Song, D. Meng, X. Yan, Y. Li, Y. Wang, P. Hu, T.-H. Ou, M. Barnell, Q. Wu, H. Wang, and W. Wu, "A memristor-based hybrid analog-digital computing platform for mobile robotics", Science Robotics **5**, eabb6938 (2020).

[24] M. Rao, H. Tang, J. Wu, W. Song, M. Zhang, W. Yin, Y. Zhuo, F. Kiani, B. Chen, X. Jiang, H. Liu, H.-Y. Chen, R. Midya, F. Ye, H. Jiang, Z. Wang, M. Wu, M. Hu, H. Wang, Q. Xia, N. Ge, J. Li, and J. J. Yang, "Thousands of conductance levels in memristors integrated on CMOS", Nature **615**, 823–829 (2023).

[25] K. Sun, J. Chen, and X. Yan, "The Future of Memristors: Materials Engineering and Neural Networks", Advanced Functional Materials **31**, 2006773 (2021).

[26] C. Li, D. Belkin, Y. Li, P. Yan, M. Hu, N. Ge, H. Jiang, E. Montgomery, P. Lin, Z. Wang, W. Song, J. P. Strachan, M. Barnell, Q. Wu, R. S. Williams, J. J. Yang, and Q. Xia, "Efficient and self-adaptive in-situ learning in multilayer memristor neural networks", Nature Communications **9**, 2385 (2018).

[27] P. Yao, H. Wu, B. Gao, J. Tang, Q. Zhang, W. Zhang, J. J. Yang, and H. Qian, "Fully hardware-implemented memristor convolutional neural network", Nature **577**, 641–646 (2020).

[28] H. Abbas, Y. Abbas, G. Hassan, A. S. Sokolov, Y.-R. Jeon, B. Ku, C. J. Kang, and C. Choi, "The coexistence of threshold and memory switching characteristics of ALD HfO 2 memristor synaptic arrays for energy-efficient neuromorphic computing", Nanoscale **12**, 14120–14134 (2020).

[29] J. Moreland and J. W. Ekin, "Electron tunneling experiments using Nb-Sn "break" junctions", Journal of Applied Physics **58**, 3888–3895 (1985).

[30] C. J. Muller, J. M. van Ruitenbeek, and L. J. de Jongh, "Experimental observation of the transition from weak link to tunnel junction", Physica C: Superconductivity and its applications **191**, 485–504 (1992).

[31] C. Zhou, C. J. Muller, M. R. Deshpande, J. W. Sleight, and M. A. Reed, "Microfabrication of a mechanically controllable break junction in silicon", Applied Physics Letters **67**, 1160 (1995).

[32] J. M. Van Ruitenbeek, A. Alvarez, I. Piñeyro, C. Grahmann, P. Joyez, M. H. Devoret, D. Esteve, and C. Urbina, "Adjustable nanofabricated atomic size contacts", Review of Scientific Instruments **67**, 108–111 (1996).

[33] J. C. Cuevas and E. Scheer, *Molecular Electronics*, Vol. 1, World Scientific Series in Nanoscience and Nanotechnology (World Scientific, 2010).

[34] Z. Balogh, "Atomi kontaktusok kölcsönnhatása szén-monoxid molekulákkal", PhD Thesis (Budapest University of Technology and Economics, 2017).

[35] R. Landauer, "Spatial variation of currents and fields due to localized scatterers in metallic conduction (and comment)", Journal of Mathematical Physics **37**, 5259–5268 (1996).

[36] N Agraït, "Quantum properties of atomic-sized conductors", Physics Reports **377**, 81–279 (2003).

[37] H. E. van den Brom and J. M. Van Ruitenbeek, "Quantum suppression of shot noise in atom-size metallic contacts", Physical Review Letters **82**, 1526–1529 (1999).

[38] M. Dreher, F. Pauly, J. Heurich, J. C. Cuevas, E. Scheer, and P. Nielaba, "Structure and conductance histogram of atomic-sized au contacts", Physical Review B **72**, 075435 (2005).

[39] V. Rodrigues, J. Bettini, A. R. Rocha, L. G. C. Rego, and D. Ugarte, "Quantum conductance in silver nanowires: Correlation between atomic structure and transport properties", Physical Review B **65**, 153402 (2002).

[40] A. I. Yanson and J. M. van Ruitenbeek, "Do histograms constitute a proof for conductance quantization?", Physical Review Letters **79**, 2157–2157 (1997).

[41] E. Scheer, N. Agraït, J. C. Cuevas, A. L. Yeyati, B. Ludoph, A. Martín-Rodero, G. R. Bollinger, J. M. van Ruitenbeek, and C. Urbina, "The signature of chemical valence in the electrical conduction through a single-atom contact", Nature **394**, 154–157 (1998).

[42] J. C. Cuevas, A. L. Yeyati, and A. Martín-Rodero, "Microscopic origin of conducting channels in metallic atomic-size contacts", Physical Review Letters **80**, 1066–1069 (1998).

[43] B. Ludoph, N. van der Post, E. N. Bratus', E. V. Bezuglyi, V. S. Shumeiko, G. Wendin, and J. M. van Ruitenbeek, "Multiple andreev reflection in single-atom niobium junctions", Physical Review B **61**, 8561–8569 (2000).

[44] F. Q. Xie, L. Nittler, C. Obermair, and T. Schimmel, "Gate-controlled atomic quantum switch", Physical Review Letters **93**, 1–4 (2004).

[45] K. Terabe, T. Hasegawa, T. Nakayama, and M. Aono, "Quantized conductance atomic switch", Nature **433**, 47–50 (2005).

[46] J. J. Wagenaar, M. Morales-Masis, and J. M. Van Ruitenbeek, "Observing quantized conductance steps in silver sulfide: Two parallel resistive switching mechanisms", Journal of Applied Physics **111**, 014302 (2012).

[47] C. A. Martin, R. H. Smit, H. S. Van Der Zant, and J. M. Van Ruitenbeek, "A nanoelectromechanical single-atom switch", Nano Letters **9**, 2940–2945 (2009).

[48] K. Yoshida and K. Hirakawa, "Stochastic resonance in bistable atomic switches", Nanotechnology **28**, 125205 (2017).

[49] C. Schirm, "Einfluss hoher Ströme auf atomare Kontakte", PhD Thesis (University of Konstanz, 2010).

[50] C. Schirm, M. Matt, F. Pauly, J. C. Cuevas, P. Nielaba, and E. Scheer, "A current-driven single-atom memory", Nature Nanotechnology **8**, 645–648 (2013).

[51] Q. Wang, R. Liu, D. Xiang, M. Sun, Z. Zhao, L. Sun, T. Mei, P. Wu, H. Liu, X. Guo, Z.-L. Li, and T. Lee, "Single-Atom Switches and Single-Atom Gaps Using Stretched Metal Nanowires", ACS Nano **10**, 9695–9702 (2016).

[52] D. Weber, "Current-Induced Switching in Superconducting Break Junctions", PhD Thesis (University of Konstanz, 2018).

[53] P. Haiber, "Stromgetriebenes Schalten in atomaren Brücken aus Kupfer Inhaltsverzeichnis", Master's Thesis (University of Konstanz, 2020).

[54] E. Scheer, P. Joyez, D. Esteve, C. Urbina, and M. H. Devoret, "Conduction channel transmissions of atomic-size aluminum contacts", Physical Review Letters **78**, 3535–3538 (1997).

[55] M. Brandbyge, K. Stokbro, J. Taylor, J.-L. Mozos, and P. Ordejón, "Origin of current-induced forces in an atomic gold wire: a first-principles study", Physical Review B **67**, 193104 (2003).

[56] G. Rubio, N. Agraït, and S. Vieira, "Atomic-sized metallic contacts: mechanical properties and electronic transport", Physical Review Letters **76**, 2302 (1996).

[57] G. Rubio-Bollinger, S. R. Bahn, N. Agraït, K. W. Jacobsen, and S. Vieira, "Mechanical properties and formation mechanisms of a wire of single gold atoms", Physical Review Letters **87**, 026101 (2001).

[58] H. Masuda and T. Kizuka, "Structure, electrical, and mechanical properties of silver nanocontacts", Japanese Journal of Applied Physics **49**, 0452021–0452025 (2010).

[59] S. V. Aradhya, M. Frei, A. Halbritter, and L. Venkataraman, "Correlating structure, conductance, and mechanics of silver atomic-scale contacts", ACS Nano **7**, 3706–3712 (2013).

[60] M. Ring, D. Weber, P. Haiber, F. Pauly, P. Nielaba, and E. Scheer, "Voltage-Induced Rearrangements in Atomic-Size Contacts", Nano Letters **20**, 5773–5778 (2020).

[61] N. Papior, S. Leitherer, and M. Brandbyge, "Simple approach to current-induced bond weakening in ballistic conductors", Physical Review B **106**, 155401 (2022).

[62] B. Sánta, "Rezisztív kapcsoló memóriák dinamikai vizsgálata", PhD Thesis (Budapest University of Technology and Economics, 2021).

[63] A. Gubicza, D. Z. Manrique, L. Pósa, C. J. Lambert, G. Mihály, M. Csontos, and A. Halbritter, "Asymmetry-induced resistive switching in Ag-Ag2S-Ag memristors enabling a simplified atomic-scale memory design", Scientific Reports **6**, 30775 (2016).

[64] L. Pósa, "Resistive switching in ultrasmall nanogap devices", PhD Thesis (Budapest University of Technology and Economics, 2019).

[65] A. Magyarkuti, "Analysis of Break Junction Measurements with Single Organic Molecules using Advanced Statistical Methods", PhD Thesis (Budapest University of Technology and Economics, 2020).

[66] P Senthil Kumar and C. Sunandana, "γ-AgI films by iodization at ambient temperature", Thin Solid Films **323**, 110–114 (1998).

[67] C. Nef, L. Pósa, P. Makk, W. Fu, A. Halbritter, C. Schönenberger, and M. Calame, "High-yield fabrication of nm-size gaps in monolayer CVD graphene", Nanoscale **6**, 7249–7254 (2014).

[68] A. Gubicza, M. Csontos, A. Halbritter, and G. Mihály, "Non-exponential resistive switching in Ag2S memristors: a key to nanometer-scale non-volatile memory devices", Nanoscale **7**, 4394–4399 (2015).

[69] S. Tappertzhofen, I. Valov, and R. Waser, "Quantum conductance and switching kinetics of AgI-based microcrossbar cells", Nanotechnology **23**, 145703 (2012).

[70] J. van den Hurk, V. Havel, E. Linn, R. Waser, and I. Valov, "Ag/GeSx/Pt-based complementary resistive switches for hybrid CMOS/Nanoelectronic logic and memory architectures", Scientific Reports **3**, 2856 (2013).

[71] W. Chen, S. Tappertzhofen, H. J. Barnaby, and M. N. Kozicki, "SiO2 based conductive bridging random access memory", Journal of Electroceramics **39**, 109–131 (2017).

[72] M. Paulsson, T. Frederiksen, and M. Brandbyge, "Modeling inelastic phonon scattering in atomic- and molecular-wire junctions", Physical Review B **72**, 201101 (2005).

[73] T. N. Todorov, "Local heating in ballistic atomic-scale contacts", Philosophical Magazine B **77**, 965–973 (1998).

[74] D. Djukić, "Simple molecules as benchmark systems for molecular electronics", PhD thesis (Leiden University, 2006).

[75] H. R. Schober, P. H. Dederichs, K.-H. Hellwege, and J. L. Olsen, "Phonon dispersion, frequency spectra, and related properties of metallic elements", in *Phonon states of alloys. electron states, and fermi surfaces of strained elements* (Springer, 1983).

[76] N. Agraït, C. Untiedt, G. Rubio-Bollinger, and S. Vieira, "Onset of Energy Dissipation in Ballistic Atomic Wires", Physical Review Letters **88**, 216803 (2002).

[77] D. Djukic, K. S. Thygesen, C. Untiedt, R. H. M. Smit, K. W. Jacobsen, and J. M. van Ruitenbeek, "Stretching dependence of the vibration modes of a single-molecule Pt-H2-Pt bridge", Physical Review B **71**, 161402 (2005).

[78] J. G. Kemeny and J. L. Snell, *Finite Markov Chains* (Springer-Verlag, 1976).

[79] T. N. Todorov, D. Dundas, A. T. Paxton, and A. P. Horsfield, "Nonconservative current-induced forces: A physical interpretation", Beilstein Journal of Nanotechnology **2**, 727–733 (2011).

[80] R. Cron, M. F. Goffman, D. Esteve, and C. Urbina, "Multiple-Charge-Quanta Shot Noise in Superconducting Atomic Contacts", Physical Review Letters **86**, 4104–4107 (2001).

[81] F. Strigl, C. Espy, M. Bückle, E. Scheer, and T. Pietsch, "Emerging magnetic order in platinum atomic contacts and chains", Nature Communications **6**, 6172 (2015).

[82] J. J. Parks, A. R. Champagne, G. R. Hutchison, S. Flores-Torres, H. D. Abruña, and D. C. Ralph, "Tuning the Kondo Effect with a Mechanically Controllable Break Junction", Physical Review Letters **99**, 026601 (2007).

[83] S. Wagner, F. Kisslinger, S. Ballmann, F. Schramm, R. Chandrasekar, T. Bodenstein, O. Fuhr, D. Secker, K. Fink, M. Ruben, and H. B. Weber, "Switching of a coupled spin pair in a single-molecule junction", Nature Nanotechnology **8**, 575–579 (2013).

[84] D. Rakhmilevitch, S. Sarkar, O. Bitton, L. Kronik, and O. Tal, "Enhanced Magnetoresistance in Molecular Junctions by Geometrical Optimization of Spin-Selective Orbital Hybridization", Nano Letters **16**, 1741–1745 (2016).

[85] R. Frisenda, V. A. E. C. Janssen, F. C. Grozema, H. S. J. van der Zant, and N. Renaud, "Mechanically controlled quantum interference in individual π-stacked dimers", Nature Chemistry **8**, 1099–1104 (2016).

[86] Z. Balogh, D. Visontai, P. Makk, K. Gillemot, L. Oroszlány, L. Pósa, C. Lambert, and A. Halbritter, "Precursor configurations and post-rupture evolution of Ag-CO-Ag single-molecule junctions", Nanoscale **6**, 14784–14791 (2014).

[87] W. H. Thijssen, D. Marjenburgh, R. H. Bremmer, and J. M. Van Ruitenbeek, "Oxygen-enhanced atomic chain formation", Physical Review Letters **96**, 026806 (2006).

[88] C. Untiedt, A. I. Yanson, R. Grande, G. Rubio-Bollinger, N. Agraït, S. Vieira, and J. van Ruitenbeek, "Calibration of the length of a chain of single gold atoms", Physical Review B **66**, 085418 (2002).

[89] A. I. Yanson, G. R. Bollinger, H. E. van den Brom, N. Agraït, and J. M. van Ruitenbeek, "Formation and manipulation of a metallic wire of single gold atoms", Nature **395**, 783–785 (1998).

[90] P. Makk, D. Visontai, L. Oroszlány, D. Z. Manrique, S. Csonka, J. Cserti, C. Lambert, and A. Halbritter, "Advanced Simulation of Conductance Histograms Validated through Channel-Sensitive Experiments on Indium Nanojunctions", Physical Review Letters **107**, 276801 (2011).

[91] C. Kergueris, J.-P. Bourgoin, S. Palacin, D. Esteve, C. Urbina, M. Magoga, and C. Joachim, "Electron transport through a metal-molecule-metal junction", Physical Review B **59**, 12505–12513 (1999).

[92] S. A. Vrouwe, E. Van Der Giessen, S. J. Van Der Molen, D. Dulic, M. L. Trouwborst, and B. J. Van Wees, "Mechanics of lithographically defined break junctions", Physical Review B - Condensed Matter and Materials Physics **71**, 2–9 (2005).

[93] J. C. Slater, "Atomic Radii in Crystals", The Journal of Chemical Physics **41**, 3199–3204 (1964).

[94] S. Kogan, *Electronic Noise and Fluctuations in Solids* (Cambridge University Press, 1996).

[95] A. Raychaudhuri, "Measurement of 1/f noise and its application in materials science", Current Opinion in Solid State and Materials Science **6**, 67–85 (2002).

[96] R. Landauer, "The noise is the signal", Nature **392**, 658–659 (1998).

[97] J. B. Johnson, "Thermal Agitation of Electricity in Conductors", Physical Review **32**, 97–109 (1928).

[98] H. Nyquist, "Thermal Agitation of Electric Charge in Conductors", Physical Review **32**, 110–113 (1928).

[99] N. E. Flowers-Jacobs, A Pollarolo, K. J. Coakley, A. E. Fox, H Rogalla, W. L. Tew, and S. P. Benz, "A Boltzmann constant determination based on Johnson noise thermometry", Metrologia **54**, 730–737 (2017).

[100] J. F. Qu, S. P. Benz, H Rogalla, W. L. Tew, D. R. White, and K. L. Zhou, "Johnson noise thermometry", Measurement Science and Technology **30**, 112001 (2019).

[101] W. Schottky, "Über spontane Stromschwankungen in verschiedenen Elektrizitätsleitern", Annalen der Physik **362**, 541–567 (1918).

[102] C. Beenakker and C. Schönenberger, "Quantum Shot Noise", Physics Today **56**, 37–42 (2003).

[103] A. McWhorter, "1/f Noise and Germanium Surface Properties", in *Semiconductor surface physics*, edited by R. Kingston (University of Pennsylvania Press, 1957).

[104] Z. Balogh, G. Mezei, L. Pósa, B. Sánta, A. Magyarkuti, and A. Halbritter, "1/f noise spectroscopy and noise tailoring of nanoelectronic devices", Nano Futures **5**, 042002 (2021).

[105] L. Pósa, Z. Balogh, D. Krisztián, P. Balázs, B. Sánta, R. Furrer, M. Csontos, and A. Halbritter, "Noise diagnostics of graphene interconnects for atomic-scale electronics", npj 2D Materials and Applications **5**, 57 (2021).

[106] A. Balandin, S. Morozov, S. Cai, R. Li, K. Wang, G. Wijeratne, and C. Viswanathan, "Low flicker-noise GaN/AlGaN heterostructure field-effect transistors for microwave communications", IEEE Transactions on Microwave Theory and Techniques **47**, 1413–1417 (1999).

[107] A. A. Balandin, "Low-frequency 1/f noise in graphene devices", Nature Nanotechnology **8**, 549–555 (2013).

[108] M. Saketh Ram, J. Svensson, and L.-E. Wernersson, "Effects of Interface Oxidation on Noise Properties and Performance in III–V Vertical Nanowire Memristors", ACS Applied Materials & Interfaces **15**, 19085–19091 (2023).

[109] E. Piros, M. Lonsky, S. Petzold, A. Zintler, S. Sharath, T. Vogel, N. Kaiser, R. Eilhardt, L. Molina-Luna, C. Wenger, J. Müller, and L. Alff, "Role of Oxygen Defects in Conductive-Filament Formation in Y2O3-Based Analog RRAM Devices as", Physical Review Applied **14**, 034029 (2020).

[110] J.-K. Lee, J. Pyo, and S. Kim, "Low-Frequency Noise-Based Mechanism Analysis of Endurance Degradation in Al/αTiOx/Al Resistive Random Access Memory Devices", Materials **16**, 2317 (2023).

[111] F. Cai, S. Kumar, T. Van Vaerenbergh, X. Sheng, R. Liu, C. Li, Z. Liu, M. Foltin, S. Yu, Q. Xia, J. J. Yang, R. Beausoleil, W. D. Lu, and J. P. Strachan, "Power-efficient combinatorial optimization using intrinsic noise in memristor Hopfield neural networks", Nature Electronics **3**, 409–418 (2020).

[112] W. A. Borders, A. Z. Pervaiz, S. Fukami, K. Y. Camsari, H. Ohno, and S. Datta, "Integer factorization using stochastic magnetic tunnel junctions", Nature **573**, 390–393 (2019).

[113] X. Li, T. Zanotti, T. Wang, K. Zhu, F. M. Puglisi, and M. Lanza, "Random Telegraph Noise in Metal-Oxide Memristors for True Random Number Generators: A Materials Study", Advanced Functional Materials **31**, 2102172 (2021).

[114] C. Wen, X. Li, T. Zanotti, F. M. Puglisi, Y. Shi, F. Saiz, A. Antidormi, S. Roche, W. Zheng, X. Liang, J. Hu, S. Duhm, J. B. Roldan, T. Wu, V. Chen, E. Pop, B. Garrido, K. Zhu, F. Hui, and M. Lanza, "Advanced Data Encryption using 2D Materials", Advanced Materials **33**, 2100185 (2021).

[115] M. Maestro, J. Diaz, A. Crespo-Yepes, M. Gonzalez, J. Martin-Martinez, R. Rodriguez, M. Nafria, F. Campabadal, and X. Aymerich, "New high resolution Random Telegraph Noise (RTN) characterization method for resistive RAM", Solid-State Electronics **115**, 140–145 (2016).

[116] M. Gonzalez, J. Martin-Martinez, R. Rodriguez, M. Acero, M. Nafria, F. Campabadal, and X. Aymerich, "Dedicated random telegraph noise characterization of Ni/HfO2-based RRAM devices", Microelectronic Engineering **147**, 59–62 (2015).

[117] M. B. Gonzalez, J. Martin-Martinez, M. Maestro, M. C. Acero, M. Nafria, and F. Campabadal, "Investigation of Filamentary Current Fluctuations Features in the High-Resistance State of Ni/HfO 2 -Based RRAM", IEEE Transactions on Electron Devices **63**, 3116–3122 (2016).

[118] F. M. Puglisi, L. Larcher, A. Padovani, and P. Pavan, "Operations, Charge Transport, and Random Telegraph Noise in HfOx Resistive Random Access Memory: a Multi-scale Modeling Study", MRS Advances **1**, 327–338 (2016).

[119] Y. Li, K.-S. Yin, M.-Y. Zhang, L. Cheng, K. Lu, S.-B. Long, Y. Zhou, Z. Wang, K.-H. Xue, M. Liu, and X.-S. Miao, "Correlation analysis between the current fluctuation characteristics and the conductive filament morphology of HfO2-based memristor", Applied Physics Letters **111**, 213505 (2017).

[120] S. Choi, Y. Yang, and W. Lu, "Random telegraph noise and resistance switching analysis of oxide based resistive memory", Nanoscale **6**, 400–404 (2014).

[121] V. Maccaronio, F. Crupi, L. Procel, L. Goux, E. Simoen, L. Trojman, and E. Miranda, "DC and low-frequency noise behavior of the conductive filament in bipolar HfO2-based resistive random access memory", Microelectronic Engineering **107**, 1–5 (2013).

[122] S. Yu, R. Jeyasingh, Y. Wu, and H.-S. P. Wong, "Characterization of low-frequency noise in the resistive switching of transition metal oxide HfO2", Physical Review B **85**, 045324 (2012).

[123] Y. Pan, Y. Cai, Y. Liu, Y. Fang, M. Yu, S. Tan, and R. Huang, "Microscopic origin of read current noise in TaOx-based resistive switching memory by ultra-low temperature measurement", Applied Physics Letters **108**, 153504 (2016).

[124] W. Yi, S. E. Savel'ev, G. Medeiros-Ribeiro, F. Miao, M.-X. Zhang, J. J. Yang, A. M. Bratkovsky, and R. S. Williams, "Quantized conductance coincides with state instability and excess noise in tantalum oxide memristors", Nature Communications **7**, 11142 (2016).

[125] S. Ambrogio, S. Balatti, V. McCaffrey, D. C. Wang, and D. Ielmini, "Noise-Induced Resistance Broadening in Resistive Switching Memory—Part I: Intrinsic Cell Behavior", IEEE Transactions on Electron Devices **62**, 3805–3811 (2015).

[126] S. B. Lee, S. Park, J. S. Lee, S. C. Chae, S. H. Chang, M. H. Jung, Y. Jo, B. Kahng, B. S. Kang, M.-J. Lee, and T. W. Noh, "Large 1/f noise of unipolar resistance switching and its percolating nature", Applied Physics Letters **95**, 122112 (2009).

[127] D. Ielmini, F. Nardi, and C. Cagli, "Resistance-dependent amplitude of random telegraph-signal noise in resistive switching memories", Applied Physics Letters **96**, 053503 (2010).

[128] Z. Fang, H. Y. Yu, W. J. Fan, G. Ghibaudo, J. Buckley, B. DeSalvo, X. Li, X. P. Wang, G. Q. Lo, and D. L. Kwong, "Current Conduction Model for Oxide-Based Resistive Random Access Memory Verified by Low-Frequency Noise Analysis", IEEE Transactions on Electron Devices **60**, 1272–1275 (2013).

[129] F. M. Puglisi, N. Zagni, L. Larcher, and P. Pavan, "Random Telegraph Noise in Resistive Random Access Memories: Compact Modeling and Advanced Circuit Design", IEEE Transactions on Electron Devices **65**, 2964–2972 (2018).

[130] O. Adak, E. Rosenthal, J. Meisner, E. F. Andrade, A. N. Pasupathy, C. Nuckolls, M. S. Hybertsen, and L. Venkataraman, "Flicker Noise as a Probe of Electronic Interaction at Metal–Single Molecule Interfaces", Nano Letters **15**, 4143–4149 (2015).

[131] A. Halbritter, L. Borda, and A. Zawadowski, "Slow two-level systems in point contacts", Advances in Physics **53**, 939–1010 (2004).

[132] B. Sánta, Z. Balogh, L. Pósa, D. Krisztián, T. N. Török, D. Molnár, C. Sinkó, R. Hauert, M. Csontos, and A. Halbritter, "Noise Tailoring in Memristive Filaments", ACS Applied Materials and Interfaces **13**, 7453–7460 (2021).

[133] Z. Wu, S. Wu, S. Oberholzer, M. Steinacher, M. Calame, and C. Schönenberger, "Scaling of 1/f noise in tunable break junctions", Physical Review B **78**, 235421 (2008).

[134] B. Sánta, Z. Balogh, A. Gubicza, L. Pósa, D. Krisztián, G. Mihály, M. Csontos, and A. Halbritter, "Universal 1/ f type current noise of Ag filaments in redox-based memristive nanojunctions", Nanoscale **11**, 4719–4725 (2019).

[135] *Femto DLPCA-200 Manual*, `https://www.femto.de/images/pdf-dokumente/de-dlpca-200.pdf`.

[136] D. Molnár, T. N. Török, R. Kövecs, L. Pósa, P. Balázs, G. Molnár, N. J. Olalla, J. Leuthold, J. Volk, M. Csontos, and A. Halbritter, "Autonomous neural information processing by a dynamical memristor circuit", (2023).

[137] J. C. Maxwell, *A treatise on electricity and magnetism* (Clarendon Press, Oxford, 1904).